UNIVERSITY OF Southampton

University of Southampton Research Repository
ePrints Soton

Copyright © and Moral Rights for this thesis are retained by the author and/or other copyright owners. A copy can be downloaded for personal non-commercial research or study, without prior permission or charge. This thesis cannot be reproduced or quoted extensively from without first obtaining permission in writing from the copyright holder/s. The content must not be changed in any way or sold commercially in any format or medium without the formal permission of the copyright holders.

When referring to this work, full bibliographic details including the author, title, awarding institution and date of the thesis must be given e.g.

AUTHOR (year of submission) "Full thesis title", University of Southampton, name of the University School or Department, PhD Thesis, pagination

http://eprints.soton.ac.uk

UNIVERSITY OF SOUTHAMPTON

FACULTY OF ENGINEERING, SCIENCE AND MATHEMATICS
SCHOOL OF ELECTRONICS AND COMPUTER SCIENCE

Spintronic and Plasmonic Applications of Electrodeposition on Semiconductors

by

Xiaoli Li

A thesis submitted in partial fulfilment of the requirements for the award of Doctor of Philosophy at the University of Southampton

Feb 2009

SUPERVISOR:
Cornelis H. "Kees" de Groot

© Xiaoli Li 2009

Dedicated to my family

UNIVERSITY OF SOUTHAMPTON

ABSTRACT

Faculty of Engineering, Science and Mathematics
School of Electronics and Computer Science

A thesis submitted in partial fulfilment of the
requirements for the award of Doctor of Philosophy

Spintronic and Plasmonic Applications of Electrodeposition on Semiconductors

by Xiaoli LI

In this thesis, metal electrodeposition on semiconductor substrates is investigated. We show that electrodeposition of metals on n-type Si and Ge is an excellent method to create Schottky barriers and that this method has a number of unique advantages over other (physical) deposition methods. These advantages can be used to improve the prospects of applications in the area of Spintronics and Plasmonics.

Firstly, the excellent current-voltage and capacitance-voltage characteristics of electrodeposited Schottky barriers indicate that they have an ideality factor close to unity and that the reverse bias leakage is orders of magnitude smaller than in evaporated Schottky barriers. These characteristics can be used to make highly doped Schottky barriers in which all reverse bias current is due to tunnelling. For magnetic metals, these Schottky barriers hence allow spin-conserved conduction which is a necessary step towards semiconductor spin valves and spin transistors.

Secondly, electrodeposition is not a line-of-sight-technique and can hence be used to grow three dimensional structures when an appropriate pattern is created. Self assembly of latex spheres is shown to change both qualitative and quantitatively upon using a lithographically defined pattern. By using electrodeposition of gold around this latex sphere pattern nano-void array photonic crystals are created. We show that plasmonic modes are detectable in these arrays opening up the path to on-chip optical communication.

Declaration of Authorship

I, **Xiaoli LI**, declare that the thesis entitled:

Spintronic and Plasmonic Applications of Electrodeposition on Semiconductors

and the work presented in it are my own. I confirm that:

- this work was done wholly or mainly while in candidature for a research degree at this University;
- where any part of this thesis has previously been submitted for a degree or any other qualification at this University or any other institution, this has been clearly stated;
- where I have consulted the published work of others, this is always clearly attributed;
- where I have quoted from the work of others, the source is always given. With the exception of such quotations, this thesis is entirely my own work;
- I have acknowledged all main sources of help;
- where the thesis is based on work done by myself jointly with others, I have made clear exactly what was done by others and what I have contributed myself;
- parts of this work have been published in research journals. A list of publications is provided with this manuscript.

Signed:

Date:

Acknowledgement

Many people have supported me during my graduate research in diverse ways, without whom the completion of this thesis would be impossible. Only a few words here could not adequately express my appreciation.

Firstly, I would like to express my deepest gratitude to my supervisor Dr. Kees de Groot for his excellent guidance, nonstop encouragement and support. He guided me how to start research since my master degree. During these five years, he was very patient to guide me to dig my advantages and overcome my weaknesses. He managed to keep me highly motivated even after disheartening events such as the destructive ECS fire in Oct., 2005. Besides the excellent individual research opporunities, he taught me how to collaborate with other researchers.

I would like to thank the School of Electronics and Computer Science of the University of Southampton for the full financial support throughout my Ph.D. studies.

I owe a big thanks to all the staffs and students of Nano reseach group for the excellent working atmosphere, the support and the social activities. Special thanks the colleagues, Dr. Michail Kiziroglou, Dr. David Gonzalez, Muhammad Husain, Dr. Alexander Zhukov, Dr. Clelia Milhano and Robin Cole, and the advisors Prof. Peter de Groot, Prof. Philip Bartlett and Prof. Jeremy Baumberg for all their help and contribution to the publications related to this Ph.D. work. Also, thanks Prof. Michael Kraft for his positive assessments through this Ph.D.

I would like to thank Mr. Charles Ford and Mrs. Sheila Ford for their patient and precise proofreading of this thesis.

Finally, huge thanks to my beloved parents and special thanks to Lingkun, for their unreserved support, encouragement, patience and understanding during my 'grown-up'.

List of Publications

Articles

related to Chapter 3:

Thermionic field emission at electrodeposited Ni-Si Schottky barriers

M. E. Kiziroglou, **X. Li**, A. A. Zhukov, P. A. J. de Groot and C. H. de Groot. Solid-State Electronics 52, 1032-1038, 2008.

Analysis of thermionic emission from electrodeposited Ni-Si Schottky barriers.

M. E. Kiziroglou, A. A. Zhukov, **X. Li**, D. C. Gonzalez, P. A. J. de Groot, P. N. Bartlett and C. H. de Groot. Solid State Communications 140, 508-513, 2006.

Electrodeposition of Ni-Si Schottky barriers

M. E. Kiziroglou, A. A. Zhukov, M. Abdelsalam, **X. Li**, P. A. J. de Groot, P. N. Bartlett, and C. H. de Groot. IEEE Transactions on Magnetics, 41, no. 10, 2639-2641, 2005.

related to Chapter 4:

Inhomogeneous Ni/Ge Schottky barriers due to variation in Fermi-level pinning

X. V. Li, M. K. Husain, and C.H. de Groot. Microelectronic Engineering (In Press), 2009.

High Quality Schottky Contacts for Limiting Leakage Currents in Ge Based Schottky Barrier MOSFETs

M. K. Husain, **X. V. Li**, and C.H. de Groot. IEEE Transactions on Electron Devices, 56, 499-504, 2009.

High-quality NiGe/Ge diodes for Schottky barrier MOSFETs

M. K. Husain, **X. V. Li**, and C.H. de Groot. Materials Science in Semiconductor Processing (In Press), 2009.

Observation of negative differential conductance in a reverse-biased Ni/Ge Schottky diode

M. K. Husain, **X. V. Li**, and C.H. de Groot. Submitted to IEEE Electron Device Letters.

A Vertical Transport Geometry for Electrical Spin Injection and Extraction in Si

M.K. Husain, **X. V. Li**, and C.H. de Groot. Submitted to IEEE Transactions on Magnetics.

related to Chapter 5:

Orientation and symmetry control of inverse sphere magnetic nano arrays by guided self-assembly.

M. E. Kiziroglou, A. A. Zhukov, **X. Li**, D. C. Gonzalez, P. A. J. de Groot, P. N. Bartlett and C. H. de Groot. Journal of Applied Physics, 100, 113720-113725, 2006.

Long range ordering in self-assembled Ni arrays on patterned Si.

D. C. Gonzalez, M. E. Kiziroglou, **X. Li**, A. A. Zhukov, H. Fangohr, P. A. J. de Groot, and C. H. de Groot. Journal of Magnetism and Magnetic Materials, 316, e78-e81, 2007.

Shape induced anisotropy in anti-dot arrays from self-assembled templates.

A. A. Zhukov, M. E. Kiziroglou, A. V. Goncharov, R. Boardman, M. A. Ghanem, M.Abdelsalam, V. Novosad, G. Karapetrov, **X. Li**, H. Fangohr, C. H. de Groot, P. N. Bartlett, P. A. J. de Groot. IEEE Transactions on Magnetics, 71, no. 10, 3598-3600, 2005.

related to Chapter 6:

Plasmonic modes in Au Nanoscale Void Arrays by Guided Self-assembly

X. V. Li, R. M. Cole, C. Milhano, P. N. Bartlett, J. J. Baumberg, and C.H. de Groot. Accepted by Nanotechnology.

Fabrication of Anti-Nanoparticle Gold Strip Arrays by Guided Self-assembly for Plasmonics

X. V. Li, C. Milhano, R. M. Cole, P. N. Bartlett, J. J. Baumberg, and C.H. de Groot. Materials Research Society Symposium Proceedings, 1077E, 1077-L04-01, 2008.

Conference Presentations

Transport Mechanisms at Ferromagnet-Silicon Schottky Barrier Contact for Spin Injection

X. Li, M. E. Kiziroglou, M. K. Husain, A. A. Zhukov, P. A. J. de Groot, and C. H. de Groot. WUN-SPIN, York, UK, 2007.

Magnetic Domain Structures in self-assembled Ni anti-dot stripes on Si

X. Li, D. C. Gonzalez, M. E. Kiziroglou, A. A. Zhukov, H. Fangohr, P. A. J. de Groot, P. N. Bartlett, and C. H. de Groot. III Joint European Magnetic Symposia (JEMS), San Sebastian, Spain, 2006.

Magnetic Domain Structures in self-assembled Ni anti-dot stripes on Si

X. Li, D. C. Gonzalez, M. E. Kiziroglou, A. A. Zhukov, H. Fangohr, P. A. J. de Groot, P. N. Bartlett, and C. H. de Groot. Condensed Matter and Materials Physics (CMMP), Exeter, UK, 2006.

Nano Inverse Sphere Ni arrays by Guided Self-assembly

X. Li, D. C. Gonzalez, M. E. Kiziroglou, A. A. Zhukov, P. A. J. de Groot, P. N. Bartlett, and C. H. de Groot. The 10_{th} Joint MMM/Intermag, Baltimore, USA, 2007.

Fabrication of Anti-Nanoparticle Gold Strip Arrays by Guided Self-assembly for Plasmonics

X. V. Li, C. Milhano, R. M. Cole, P. N. Bartlett, J. J. Baumber, and C.H. de Groot. Materials Research Society (MRS) Spring Meeting, San Francisco, USA, 2008.

Contents

Chapter 1

Introduction

1.1 Electrodeposition on Semiconductors

Electrodeposition, also called electroplating or electrochemical deposition is a process of coating an electrically conductive item with a thin layer of metal using electrical current. Modern electrodeposition was invented by Italian chemist Luigi V. Brugnatelli in 1805 [1]. He used the voltaic pile to facilitate the first electrodeposition. By 1839, scientists in Britain and Russia had independently devised metal deposition processes similar to Brugnatelli's for the copper electroplating of printing press plates. Soon after, John Wright of Birmingham, England discovered that potassium cyanide was a suitable electrolyte for gold and silver electroplating. Wright's associates, George Elkington and Henry Elkington were awarded the first patents for electroplating in 1840. These two then founded the electroplating industry in Birmingham, England from where it spread around the world [1].

Although electrodeposition is a very simple, fast, cost effective and mature industrial deposit method, researchers in semiconductor fabrication field are usually not very familiar with this method because the method requires a conductive substrate. The primary problems of metal electrodeposition on a Si surface are nucleation, adhesion and limitation of the current distribution associated with high resistivity of the Si layer. As it turns out Si with even relatively low doping is sufficiently conductive to allow electrodeposition. Other smaller problems are also not insurmountable. Review papers of Oskam[2] and Ji [3] detail the literature available on electrodeposition of

metal films directly on semiconductor substrate.

We show in this thesis, that metal electrodeposition on Si and Ge is certainly possible if a few precautions are taken and that the resulting Schottky barriers have properties superior to those of evaporated or sputtered barriers. Firstly, and in particular the reverse bias leakage is significantly lower, which might make these barriers suitable for spin injection and detection devices. Secondly, since it is not a line of sight technique, complicated 3D structures can be grown which can be used to create plasmonic waveguides

1.2 Spintronics

Traditionally, an electrical current is regarded as a flow of electrons which carry charge. Besides its charge, an electron also carries a spin. With the dawn of the new millennium, a novel technology called spintronics (magneto-electronics or spin-based electronics) has emerged which exploits the quantum propensity of electrons to spin as well as making use of their charge state. The spin can be used to differentiate electrical carriers into two different types according to whether their spin projection onto a given quantization axis is $\pm\frac{1}{2}$. The two states of spin are characterized as 'up' and 'down'. Spins can be manipulated faster and at lower energy cost than charge. Hence the new generation of devices which combine standard microelectronics with spin-dependent effects could have faster switching times, higher integration densities and lower power consumption than the conventional devices. Furthermore, because of its quantum nature, electron spin may exist not only in the "up" or "down" state but also in infinitely many intermediate states depending on the energy of the system. This quality holds the potential for what is, in effect, highly parallel computation. Thus it could make a quantum computer, which is capable of performing certain types of calculations, much faster.

In this active and promising research field of Spintronics, several approaches are explored in parallel. One approach is employed in magnetic (random access) memory (MRAM), where an array of magnetic memory elements is placed on top of a semiconductor wafer containing transistors and other circuitry required to drive memory. This can still be considered to be "metal spintronics" as the integration with Si is

only on a passive level. The second approach is using a magnetic semiconductor to put magnetic properties into semiconductor materials. This is the most intimate form of integration and often called "Semiconductor Spintronics". The third approach is "Hybrid Spintronics" in which ferromagnetic metals and semiconductors are combined within the active (transistor or diode) part of the circuit. The spin-valve transistor (SVT) demonstrated by Monsma et al. [4] in 1995 is a typical example of a hybrid device in which spin dependence of the transport occurs in the ferromagnets and the semiconductors are used to create potential barriers to operate the device. In the development of spin-valve transistor, spin injection and detection, the transfer of spin information into a semiconductor device through spin-polarized current, becomes the biggest challenge. The biggest obstruction is the so called conductivity mismatch problem. Schottky contacts are proposed to solve this problem. However, the Schottky contacts fabricated by physical methods on Si did not attain the requirements for spin injection. Here, we investigate if the Schottky contacts fabricated by electrodeposition have higher potential for spin injection.

1.3 Plasmonics

Optical data transfer allows high bandwidth but requires bulky tubes with reflective interiors while electronic data transfer only requires tiny wires but operates at low frequencies. When light hits the metallic surface under precise circumstance, electron density waves, called plasmons, are produced. Because these density waves are generated at optical frequencies, they can theoretically encode a lot of information, even more than is possible for conventional electronics. Therefore, a new technology called plasmonics has emerged, which squeezes electromagnetic waves into minuscule metal wires by using light to create plasmons. This technology included the advantages of both optical and electronic data transfer. Hence, plasmonics allows the transmission of data at optical frequencies along the surface of a tiny metal wire. Plasmonic circuits are promising to build fast interconnects in computer chips that can move large amounts of data across a chip.

The main limitation of plasmonics today is that plasmons survive for a distance which is too short to serve as a basis for computer chips. To improve the sending

distance, the key is to use a material with a low refractive index, ideally negative, such that the incoming electromagnetic energy is reflected parallel to the surface of the material and transmitted along its length as far as possible. There exists no natural material with a negative refractive index, but nanostructured materials can try to fill this gap. Using guided self-assembly, inverse sub-micro sphere (nanovoid) metal arrays on Si is a promising structures to explore the creation of new plasmon modes. To realize these nanostructures, it is necessary to combine conventional semiconductor fabrication, the chemical process of self-assembly and electrodeposition. The resulting structure is a proto-type photonic crystal waveguide suitable to study plasmon modes in constrained geometries.

1.4 Objectives and Outline

This thesis is organized as follows: In Chapter 2, the fundamentals of electrodeposition are introduced. It is explained how to develop a new electrodeposition process for various metals, depending on the applications, such as a sharp interfacial layer, or a bright surface. Chapter 3 introduces the concepts of the Schottky barriers, and presents the analysis of the current-voltage (I-V) and capacitance-voltage (C-V) analysis of the experimental barriers in terms of ideality factor, and barrier height. Chapter 4 introduces the ideas of Spintronics, with a description of magnetoresistance, spin injection, and spin transistors, followed by an experimental section on creating magnetic alignment in electro-deposited barriers. This chapter contains two sections on the initial steps to fabricate lateral and vertical spin valves and transistors. Chapter 5 introduces the background of self-assembly, followed by an experimental section on creating self-assembled latex sphere templates in flat bottom trenches, and transferring them to the Ni nanovoid arrays on Si by electrodeposition. The anisotropic magnetoresistance of Ni nanovoid arrays is presented at the end of this chapter. Chapter 6 introduces the ideas of Plasmonics, with some basic theory of surface plasmon polaritons. It is followed by an experimental section on creating the Au nanovoid strip arrays into v-shape Si trenches. The optical measurements of Au nanovoid arrays are carried out and analyzed. Finally, in Chapter 7, the summary is drawn.

Chapter 2

Metal Electrodeposition on Semiconductors

2.1 Introduction

In electrodeposition, the sample to be coated is the cathode which is placed into a container containing a solution of one or more metal salts. The metal salt 'MA' dissociates in water to positively charged metal cations M^{n+} and negatively charged salt anions A^{n-} as illustrated in fig. 2.1. The sample, the solution and the anode form together the electrical circuit over which a potential difference can be applied. The cathode electrode, which is to be plated, is negatively charged, and it attracts the positively charged M^{n+} cations. Meanwhile the negatively charged A^{n-} anions are attracted to the positively charged anode electrode. An electron current in the external circuitry completes the loop and reduces the M^{n+} cations to the metallic form M. At the anode, electrons are removed from the metal M, oxidizing it to M^{n+} cations and hence replenishing the supply. Thus, the anode dissolves as ions into the solution, enabling the concentratation of the metal salt MA to remain constant.

As the flow through the metal electrodes is necessarily an electron flow, it requires that if we want to use a semiconductor as electrode that it is doped n-type, such that electrons are the majority carrier. We see later in chapter 3, that if the cathode is n-type Si and the metal a 3d metal or noble metal, a Schottky barrier between the metal and the Si will form. This Schottky barrier is essentially a diode which

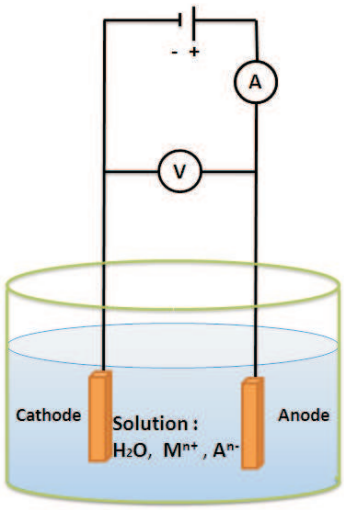

Figure 2.1: Schematics of an electrolytic cell for plating metal "M" from a solution of the metal salt "MA".

only allows conduction in one direction. The forward bias of the barrier is with an electron flow from the semiconductor to the metal deposit such that the electrons can continue to reduce the metal salt-ions and that the electro-deposition process can continue unlimited.

In this chapter, electrodeposition is explained in detail. The fundamental theory and elements of the electrodeposition experiments, such as reference electrode and electrodeposition solutions are explained. Four metal-semiconductor electrodeposition processes are developed and the optimum deposition conditions are described. Two systems with ferromagnetic metal on Si, Ni-Si and Co-Si, have been described before in literature. The other two processes, high reflectivity metal Au on Si, and Ni on Ge, are completely novel.

2.2 Principle of Electrodeposition

In this section, the essential principles of electrodeposition based on several fundamental electrochemical books are presented [5, 6, 7, 8]. For our purposes, the most important aspects of electrodeposition are electrode potential, kinetics and growth mechanism, film thickness, and cyclic voltammetry.

2.2.1 Electrode Potential

As described in fig. 2.1, when a metal M is immersed in an aqueous solution containing these same metal ions M^{n+}, there will be an exchange of the metal ions M^{n+} between the metal and the solution. Some M^{n+} enter the solution from the crystal lattice while some enter the crystal lattice from solution. If no external circuit is connected, the speed of these two reaction may not be the same initially. After a certain period of time, a dynamic equilibrium between the metal M and its ions in the solution will spontaneously result, expressed by

$$M^{n+} + ne \Leftrightarrow M \tag{2.1}$$

where e is electron, n is the number of electrons involved in the reaction. Reaction from the right to the left liberates electrons and is called oxidation. Reaction from the left to the right consumes electrons and is called reduction.

Though the interphase region is neutral at equilibrium, the charging of the interphase still causes a potential difference $\Delta\phi(M,S)$ across the interphase between the potential of the metal ϕ_M and that of the solution ϕ_S, expressed by

$$\Delta\phi(M,S) = \phi_M - \phi_S \tag{2.2}$$

Since only the metal is considered as a terminal, the potential difference cannot be measured directly. Hence, in order to obtain the value of the potential difference, another interphase (the reference electrode) is introduced to connect with the solution and thus form an electrochemical cell.

When the two electrodes of a cell are connected by an external circuit, the cell reaction will only happen naturally if the free energy change ΔG is negative. The free energy change can be expressed as a function of concentration of the products and the reactants:

$$\Delta G = \Delta G^0 + RT \ln Q \tag{2.3}$$

where R is the gas constant, T is the absolute temperature, and Q is the reaction quotient, the ratio of concentrations of product and reactant. When concentrations of the reactant and product are equal,

$$Q = \frac{M^{n+}}{M} = 1 \tag{2.4}$$

the standard free-energy change ΔG^0 is equal to ΔG. Since the thermal voltage is expressed as

$$V_T = kT/q \tag{2.5}$$

the free energy change can further be expressed as a function of cell voltage ε:

$$\Delta G = -n\varepsilon qR/k = -n\varepsilon RT/V_T \tag{2.6}$$

where n is the number of electrons involved in the reaction, ε is the cell voltage. Introducing Eq. 2.6 into Eq. 2.3, the general Nernst equation giving the concentration dependence of the equilibrium cell voltage is obtained

$$\varepsilon = \varepsilon^0 - \frac{V_T}{n} \ln Q \tag{2.7}$$

In a general case of a metal/metal-ion electrode, such as Eq. 2.1, there are two reactants, M^{n+} and e, and one product M. Since the concentrations of metal (M) and electrons (e) in the metal lattice both equal 1 by convention, Eq. 2.7 is simplified to

$$E = E^0 - \frac{V_T}{n} \ln[M^{n+}] \tag{2.8}$$

where E^0 is the relative standard electrode potential of the M/M^{n+} electrode. Since the value of V_T is 0.0257 V at 298 K(25°C, room temperature), the M/M^{+n} electrode potential is

$$E = E^0 - \frac{0.0592}{n} \log[M^{n+}] \tag{2.9}$$

It should be noted that the effect of considering the activity coefficient in this calculation is not substantial unless the concentration of solution is 0.001 molar per litre or lower. Then the activity can be replaced by the concentration.

The relative standard electrode potential of a certain metal can be obtained by forming a cell consisting of the electrode under investigation and the normal hydrogen electrode (NHE). This is the hydrogen electrode when the pressure of hydrogen is 1 atm and the activity of hydrogen cation is 1. By convention, its potential is zero.

2.2.2 Thickness control

In all of our work, specific thin metal films are able to electrodeposit because the thickness of film is controlled in realtime straightforwardly by the total current. The

total charge transferred in the process can be calculated by

$$Q = \int I dt = n \cdot q \cdot a \tag{2.10}$$

where n is the number of electrons taking part in depositing, q is the electrical charge per electron and a is the number of atoms deposited. This atom number a is related to the film thickness deposited t. As we know, the mass of the deposit is

$$m = m_w \cdot \frac{a}{N_a} = \rho \cdot A \cdot t \tag{2.11}$$

where m_w is the atomic weight of species M, N_a is Avogadro's number, A is the contact area and ρ is the density of metal. So the relation between thickness and charge is now established by combining equations 2.10 to 2.11

$$t = \frac{m_w Q}{nA\rho q N_a} \tag{2.12}$$

However, during Ni and Co electrodeposition, part of charge contributes to hydrogen evolution. Therefore, an estimate of the current efficiency needs be carried out. The details of the estimate are stated in Ref.[9].

A key equation in the applied electrochemistry, which is about overpotential and potential drop term IR, is

$$V = E_e^C - E_e^A - |\eta_C| - |\eta_A| - IR \tag{2.13}$$

where V is the total cell voltage, E_e^C and E_e^A are the equilibrium potential of the cathode and anode respectively, η_C and η_A are the overpotential of the cathode and anode respectively and IR is the potential drop, where R is the resistance of the electrolyte solution between the electrodes. Because overpotential and potential drop in all cells represent energy inefficiencies, they must be minimized.

The potential drop term, IR, also explains the reason why the three electrode system is more advanced than the two electrode cell and replaces the latter in laboratory application nowadays. In a two electrode cell, the plot of I-V would not provide enough information about the electron transfer processes in the cell since both the overpotential and the IR term vary with the current. Whereas, in a three electrode system, a third electrode, called the reference electrode, is designed so that its I-V response is characteristic of the processes at only one of the electrodes. The reference

electrode is positioned as closed as possible to the working electrode surface. Using a potentiostat, the potential of the working electrode is controlled versus the reference electrode. Also it should be noticed that the electrolyte contacting area of the working electrode should be much smaller than that of the counter electrode in order to avoid the substantial polarization of the latter so that the response of the cell is only from the working electrode.

2.2.3 Kinetics and Growth mechanism

Since the rate of electrolysis will depend on the kinetics of the two electrode reactions, a new concept overpotential is introduced. In a non-equilibrium electrochemical cell, the difference η between the potential of an electrode E(I) as a result of current flowing and the equilibrium potential of this same electrode (E_e, potential in the absence of current) is defined as overpotential.

$$\eta = E(I) - E_e \tag{2.14}$$

The overpotential η is regarded as the power source to support the overall electrode reaction, which is normally composed of 4 main partial reactions: electron transfer, mass transfer (mainly diffusion), chemical reaction and crystallization. Electron-transfer reaction occurs between the electrode and an electron carrier, which involves the transfer process of the electron carrier across the double layer. This type of reaction is the only partial reaction directly influenced by the electrode potential. Mass-transfer reaction means that the substances consumed, or formed, during the electrode reaction need to be transported from the bulk solution to the electrode surface and from the electrode surface to the bulk solution. The rate of the mass transport depends only on the bulk concentration of the electroactive species and the mass transport regime.

The relationship between the current density J and the overpotential, Butler-Volmer equation is described by:

$$J = J_0[exp(\frac{(1-\alpha)n\eta}{V_T}) - exp(\frac{-\alpha n\eta}{V_T})] \tag{2.15}$$

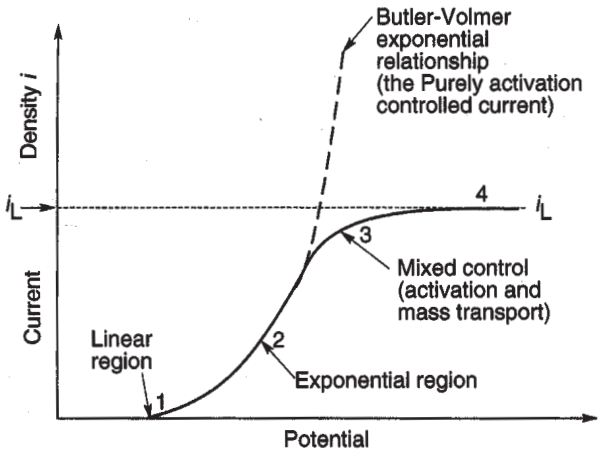

Figure 2.2: Four regions in the general current-overpotential relationship[8].

where i_0 is the exchange current density (i_0=i when η=0)and α is the transfer coefficient.

A number of approximations can be made to this formula. When the absolute value of overpotential is smaller than 0.10 V, the current density varies linearly with the overpotential:

$$J = J_0 \frac{n\eta}{V_T} \tag{2.16}$$

When the absolute value of overpotential is greater than 0.10 V, the cathodic current density is majority if the η is negative. The Bulter-Volmer equation can be simplified as

$$J = -J_0 e^{-\alpha n\eta/V_T} \tag{2.17}$$

for large cathodic current density. Taking the logarithm of Eqs. 2.17, the Tafel equation is obtained:

$$\eta = a + b\log|i| = b\log|i_0| + \log|i| \tag{2.18}$$

Since in our work, metal deposition is a cathodic process, the theoretical value of the constant b for the cathodic process is

$$b_c = \frac{2.303V_T}{\alpha n} \tag{2.19}$$

The current-potential relation defined by Eqs. 2.17 also has a limit where the rate of

deposition reaction is limited by the mass transfer. Fig. 2.2 shows a general current density-overpotential. The maximum current density is given by Eqs. 2.20

$$i_L = \frac{nV_T D}{\delta RT} c_b \tag{2.20}$$

where D is the diffusion coefficient of the depositing species M^n+, δ is the diffusion layer thickness and c_b is the bulk concentration of M^n+ in the solution.There are two basic mechanisms for formation of a coherent deposit [6, 10]: layer growth and three-dimensional (3D) crystallites growth (also called nucleation-coalescence growth). In the layer growth mechanism, a crystal deposit enlarges by a spreading of discrete layers, one by one across the surface. When the surface is covered by a grown layer, the next layer begins to form by the same way.

In the 3D crystallites growth mechanism, the structural components are 3D crystallites, so that a coherent deposit is built up as a result of coalescence of these crystallites. There are four stages to make up of the growth sequence of electrodeposition via nucleation coalescence:(i) formation of isolated nuclei and their growth to 3D crystallites, (ii) coalescence of 3D crystallites, (iii) formation of linked network and (iv) formation of a continuous deposit.

The development of growth forms on overpotentials stems from the potential dependence of the nucleation and growth processes. Competition between nucleation and growth processes is strongly influenced by the potential of the cathode [6, 5].

2.2.4 Cyclic Voltammetry

There are two different types of transient techniques to probe the electrodeposition behaviours. In the first type, an instantaneous perturbation of the electrode potential or current is applied and the system is monitored as it relaxes towards its new steady state. The method is called chronoamperometry or chronopotentiometry dependent on whether potential or current is perturbed respectively. In the second type, a periodically varying perturbation of current or potential is applied to the system, and its response is measured as a function of the frequency of the perturbation. The method is called cyclic or a.c. voltammetry dependent on whether the potential source is DC or AC.

Since cyclic voltammetry can obtain all kinetic parameters by recording the rate of

mass transport varying with time, this method is the most common technique when studying a system for the first time. The cell current is recorded as a function of the applied potential. The potential is continuously changed as a linear function of time at a scan rate (ν, the rate of change of potential with time). Once the potential scan range is decided, the potential scan starts at any initial potential which is in the potential range and scans in one direction until reaching the critical potential at the end of range, then the scan direction is reversed for a new scan. The potential waveform is usually of the form of an isosceles triangle. This has the advantage that the product of the electron transfer reaction that occurred in the forward scan can be probed again in the reverse scan. Hence, it is a powerful tool for the determination of formal redox potentials, detection of chemical reactions that precede or follow the electrochemical reaction and evaluation of electron transfer kinetics.

In experiments, qualitative experiments will be carried out firstly in order to get an integral feel for the system before proceeding to semi-quantitative and finally quantitative experiments from which kinetic parameters may be calculated. In a classic qualitative study, the scan will be set up over a wide range of scan rates and potential scan range. Usually there will be several peaks, and by observing how these appear and disappear as the potential limits and sweep rate are varied, and also by noting the differences between the first and subsequent cycles, it is possible to determine how the processes represented by the peaks are related. At the same time, from the scan rate dependence of the peak amplitudes the role of absorption, diffusion and coupled homogeneous chemical reactions may be identified. The difference between the first and subsequent cyclic voltammograms frequently provides useful mechanistic information. It should be emphasized that kinetic parameters can only be accurately obtained from an analysis of the first scan.

Illustrated in Fig. 2.3(a), a redox reaction is described. Initially, only the oxidized form of the species (M^{n+}) is assumed to be present. Thus, a negative potential scan is chosen for the first half cycle during which a cathodic current is observed. Because the solution is quiescent, the product generated during the forward scan is available at the surface of the electrode for the reverse scan resulting in an anodic current.

At the start of the experiment(point 1), there is no net conversion of M^{n+} into M, the reduced form since the cell potential is lower than the redox potential. As

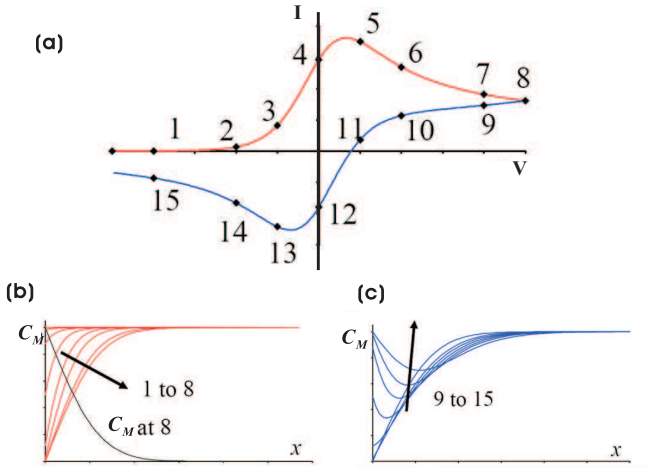

Figure 2.3: (a) Schematic of Cyclic voltammogram for a reversible process, $M^{n+} + ne \rightleftharpoons M$. X-axis is current(I) and Y-axis is voltage(E). Initially only M^{n+} present in solution. (b) The concentration profiles of M (C_M) at numbered points in the first reduction stage. Y-axis is the distance to the working electrode (x). (c) The concentration profiles of M at numbered points in the first oxidation stage. Modified from [11]

the redox potential is approached, there is a net cathodic current which increases exponentially with potential. As M^{n+} is converted into M, concentration gradients are set up for both M^{n+} and M, and diffusion occurs down these concentration gradients. At the cathodic peak (point 5), the redox potential is sufficiently negative that any M^{n+} that reaches the electrode surface is instantaneously reduced to M. Therefore, the current now depends upon the rate of mass transfer to the electrode surface. Upon reversal of the scan (point 8), the current continues to decay until the potential nears the redox potential. At this point, a net oxidation of M to M^{n+} occurs which causes an anodic current which eventually produces a peak shaped response (point 13). Fig. 2.3(b,c) show the concentration profiles of reductive species (M) at numbered points to help understand this reversible process.

If the electron transfer rate at all potentials is significantly greater than the rate of mass transport so that the redox system remains in Nernstian equilibrium throughout the potential scan, the electrochemical reaction is reversible. But this is just an ideal case. In practice, the rate of electron transfer is insufficient compared with mass transfer, or chemical reactions are coupled to the redox process, or adsorption of either reactants or products occurs, and this equilibrium is broken.

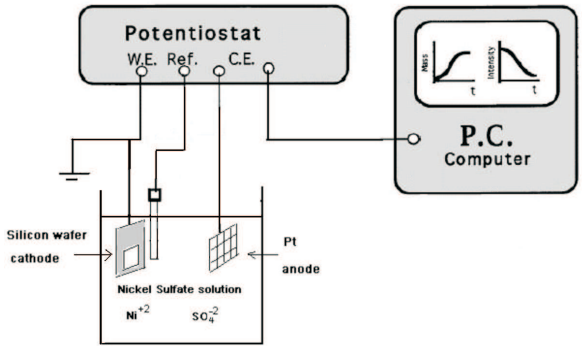

Figure 2.4: Scheme of experimental set up for Ni electrodeposition on Si, the electrochemical control and the monitoring by a PC computer.

2.3 Experimental Details

2.3.1 Experimental Setup

The setup of the electrodeposition experiment is illustrated in Fig. 2.4. This is a three-electrode electrodeposition system with potentiostat. The potentiostat (Autolab PGSTAT12) controls the equilibrium electrode potentials using a saturated calomel reference electrode (SCE)(Ref401, Radiometer Analytical model). A large area platinum gauze as the anode connects to the positive pole of the potentiostat, which functions as a counter electrode, and the silicon wafer as the cathode connects to the negative pole of the potentiostat, which functions as a work electrode. In addition, a personal computer (PC) is connected the potentiostat to monitor the electrodeposition process with potentiostatic current-time transient curve. All of the electrodes are rinsed in the electrobath.

There are many types of reference electrodes to measure equilibrium electrode potentials, such as calomel electrodes(including normal calomel electrodes(NCE), saturated calomel electrodes(SCE), sodium saturated calomel electrodes(SSCE)), silver-silver chloride electrodes, mercury-mercurous hydrogen electrodes and nonaqueous electrodes. As mentioned before, the relative electrode potentials are determined by measuring cell voltage. So the different reference electrodes are corresponding to different relative electrode potentials. A saturated calomel electrode (SCE) is selected for this experiment. The construction is shown in Fig. 2.5.

The saturated calomel electrode consists of mercury, calomel, KCl solution from

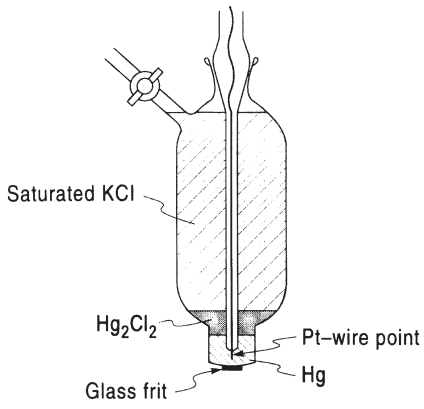

Figure 2.5: Saturated calomel electrode (SCE) for measuring electrode potential[6].

bottom to top:

$$Hg|Hg_2Cl_2|Cl^-$$

The electrode potential [6] is

$$E = E^0 - \frac{RT}{2qN_a}\ln[Cl^-] \tag{2.21}$$

where R is the gas constant, T is the absolute temperature, and Cl^- is the concentration of Cl anion with unit of mol/L.For the concentration of KCl of SCE is at saturation (about 3.5 M), the standard potential (E^0) of the SCE at 25° is 0.242 V versus NHE. SCE has a large temperature coefficient [6]:

$$E[V] = 0.242 - 7.6 \times 10^{-4}(T - 298) \tag{2.22}$$

2.3.2 Electrodeposition solutions

The components of electrodeposition solutions are varied dependent on the metal components for deposit, the adhesion properties between the metal and substrate and the functional applications of the deposited structures. Besides the essential deposited metallic ions, acid/alkali ions and other chemical additives play modulatory functions.

- **Nickel and Cobalt Solutions**

The electrodeposition baths for nickel and cobalt were prepared by ourselves. The nickel bath contains 0.1 mol/dm^{-3} nickel sulfate ($NiSO_4{\cdot}6H_2O$), 0.1 mol/dm^{-3} boric

acid, 5 m mol/dm^{-3} sodium dodecly sulfate (SDS) and sulfuric acid (Analar grade > 98%, to adjust pH value between 3.0 - 3.5). Nickel sulfate ($NiSO_4 \cdot 6H_2O$) contributes the nickel ions for electrodeposition. The advantages of this nickel salt relative to the other nickel salts are remarkable. It is the cheapest salt of nickel. Its anion is so stable that it is not reduced at the cathode or oxidized at the anode or volatilized. In addition, it is easy to dissolve. The main function of boric acid is to control the pH value in the cathode film, and as a weak buffer in the solution, it also improves the smoothness of the deposit surface[8]. SDS serves as an additive to improve the wettability of the electrolyte to the silicon surface so that the adhesion between metal and semiconductor is enhanced. The cobalt bath contains 0.1 mol/dm^{-3} cobalt sulfate ($CoSO_4 \cdot 7H_2O$), 0.1 mol/dm^{-3} boric acid, and sulfuric acid (Analar grade > 98%, to adjust pH value between 3.0 - 3.5). It should be noticed that the additive SDS is not required in the cobalt bath due to the good intrinsic wettability of cobalt sulfate.

- **Gold Solutions**

Because of the good stability of the gold(I) cyanide complex $[Au(CN)_2]^-$, gold cyanide baths are the most common solution for gold electrodeposition. According to the pH value, there are three kinds of cyanide baths: alkaline cyanide baths, acid cyanide baths and neutral cyanide baths. Because the gold film obtained from alkaline cyanide baths presents very bright and smooth appearance, the standard alkaline cyanide baths are selected as the gold solution in our work, which were purchased from Cravemount Ltd directly. The cathodic reaction of this type of solution is

$$4[Au(CN)_2]^- + 4e^- \rightarrow 4Au + 8CN^- \tag{2.23}$$

Since the anode is nonsoluble platinum, oxygen gas and hydrogen ions are the dominant products at the anode, as shown in Eq. 2.24:

$$2H_2O \rightarrow 4H^+ + O^2 + 4e^- \tag{2.24}$$

The cathodic current efficiency for the deposition of the gold from alkaline baths can be as high as 90% to 100% with adequate gold content in the bath and sufficient stir.

2.4 Optimization of Electrodeposition

2.4.1 Pretreatment

There are two kinds of pretreatments required for good electrodeposition on a semiconductor. Surface pretreatment, either chemical or mechanical, is very important to the quality of electrodeposition. Its effect directly influences the adhesion of the metal layer coating to the cathode surface, which is of particular importance on semiconductor substrates. Surface cleaning is designed to remove contaminants and films from the substrate. Contamination can cause poor adhesion and even prevent deposition. The surface contamination can be intrinsic (such as oxide layer) or extrinsic (comprised of organic debris and mineral dust from the environment or preceding processes). Usually this cleaning process includes the employing of solvents, alkaline cleaners, acid cleaners, abrasive materials or water [12].

Nucleation pretreatment is very necessary for metals electrodeposited on a semiconductor due to the weak conductivity of the semiconductor. There are several pretreatment methods to overcome the low nuclei density problem. Kwon *et al.* [13] used a chemical pretreatment, Pd activation as a nucleus formation method to make Ru electroplating possible on TiN substrate. Gabrielli *et al.* [14] used a electrochemical pretreatment. They polarized the electrode at very negative potential (-2.5 V/SCE) during 5 min to get a vigorous hydrogen evolution, to reduce oxide or organic impurities. Afterwards, the electrode was rinsed in dilute acetic acid to dissolve traces of calcium carbonate. In this work, we applied a pulse of further negative potential on the semiconductor cathode electrode to produce a high density nuclei layer instantaneously.

- **Pretreatments for Electrodeposited Ni-Si/Co-Si Schottky Barriers**

Specific pretreatments are required for nickel or cobalt electrodeposition on silicon surfaces. Our pretreatment operations have two basic steps:

- Surface cleaning or preparation. In this step, two-step Radio Corporation of America (RCA) clean and Buffered Hydrogen Fluoride (BHF) clean are applied. RCA clean is to remove intrinsic contamination while BHF clean is not only to remove the oxide layer but also to leave the silicon surface H-terminated so

that the surface becomes hydrophobic. In the BHF clean, the silicon sample was rinsed in buffered hydrogen fluoride solution (20:1) for 30 seconds.

- Surface electrochemical pretreatment to improve the nucleation. In this experiment, a electrochemical pretreatment applied -1.5 $\sim$ -1.9 V/SCE negative potential during 0.2 second to 0.4 second to improve the nucleation magnitude to get good quality electrodeposition.

- **Pretreatments for Electrodeposited Au on Si**

Due to the weak bondstrength between gold and Si which causes gold film to peel-off after it was electrodeposited on silicon surface, some specific pretreatments should be carried out. The typical method is the growth of a thin chrome or titanium film, with several nanometers thickness, by evaporation or sputtering. However, this method is not suitable for our design because the chrome or titanium film would not only cover the silicon surface but also the silicon dioxide surface. Alternatively, it is possible to deposit this kind of bonding layer through electrodeposition. However, it involves even more complicated work to deposit a smooth chrome or titanium film with controllable thickness on silicon. The method for growth of a bonding layer that we used finally, was prepared by a simple chemical reaction[15, 16, 17]. Firstly, the pattern silicon substrate was dipped into a 20:1 BHF for 6 seconds to etch the ultrathin layer of native oxide. After quickly washing by DI water, the second dipping step was to place the sample into 5 mol/L potassium hydroxide (KOH) for 30 seconds to leave OH-terminal on the silicon surface. The sample was washed by DI water to remove KOH, then washed by ethanol (EtOH) to remove DI water. Finally, the sample was immersed into a solution of 10% APTMS (3-aminopropyltrimethoxysilane)in high-performance liquid chromatography(HPLC) grade EtOH during 8-9 hours. After this treatment, the sample would be ready for self-assembly after rinsing instantly into HPLC grade EtOH for 40 seconds then drying under Argon.

2.4.2 Au Film on Si

In the initial stage, cyclic voltammetry is applied to study a new system. At the beginning, a sample holder was used to extend the dimensions of the silicon wafer sample in order to load it into the electrolytic cell easily. But the small cathodic current in this case, shown in Fig. 2.6, indicated that the conductivity between sample and holder was not good. So, in the following experiments, the silicon wafer samples were connected directly to the work electrode.

Solely based on a voltammogram (shown in Fig. 2.7 solid line) with the the scan range from 0 to -1.3V, it is hard to judge whether the current is caused by gold deposition or Hydrogen evolution. Therefore, a large range potential scan (shown in Fig. 2.7 dashed) is carried out. Three mechanisms occurred: The nucleation started at -0.5 V/SCE; Between -0.5 to -1.9V/SCE, the cathodic current was dominated by gold deposition; After -1.9V/SCE, the cathodic current suddenly increased which indicated the hydrogen evolution began. It should be noticed that in the common potential scan range from 0 to -1.3V/SCE, the currents of these two scans are not identical. This is mainly caused by the difference of deposition areas between these two sample.

Initially, according to the cyclic voltammogram, -1V/SCE was selected as the deposition potential, which can promisingly control the speed of electrodeposition. However, as the solid line in Fig. 2.8 shows, the current keeps increasing during the deposition, which indicates that the deposition process is accompanied with further nucleation. It does not result in a uniform film. A pulse pretreatment usually yields finer grain deposits because of the high pulse current density and resulting high nucleation rate. The potentiostatic current-time transient curve without pulse pretreatment, shown in Fig. 2.8 solid, which strongly reduced current relative to the with pulse pretreatment case, indicates that during a 0.5 second pulse -1.2V/SCE, nuclei spread on the silicon surface uniformly then under the low deposition potential -0.7V/SCE, the gold film grows nearly without nucleation. It results in a uniform film. Fig. 2.9 proves this opinion.

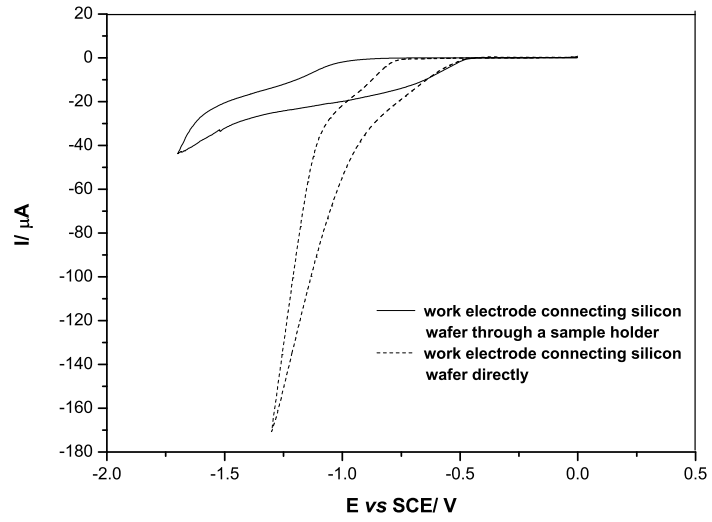

Figure 2.6: Comparison of two cyclic voltammograms for Au. Potential scan rates were both 0.02 V/s. The cathodic current in the with sample holder case was much smaller than the current without holder case though the former scan range was more negative.

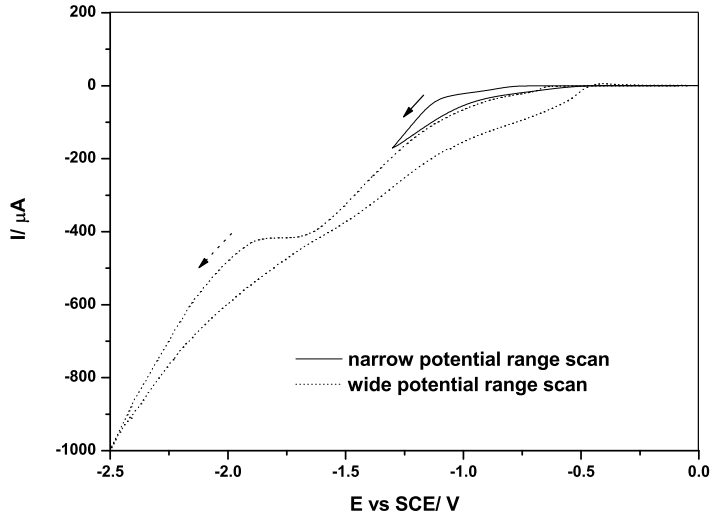

Figure 2.7: Comparison of two cyclic voltammograms for Au with different scan ranges. Potential scan rates were both 0.02 V/s and the scans both start from 0V/SCE. The wide scan range was from 0 to -2.5V/SCE while the narrow scan range was from 0 to -1.3V/SCE. The dispersion of currents in the potential range from 0 to -1.3V/SCE is mainly due to the difference of deposit areas between these two samples.

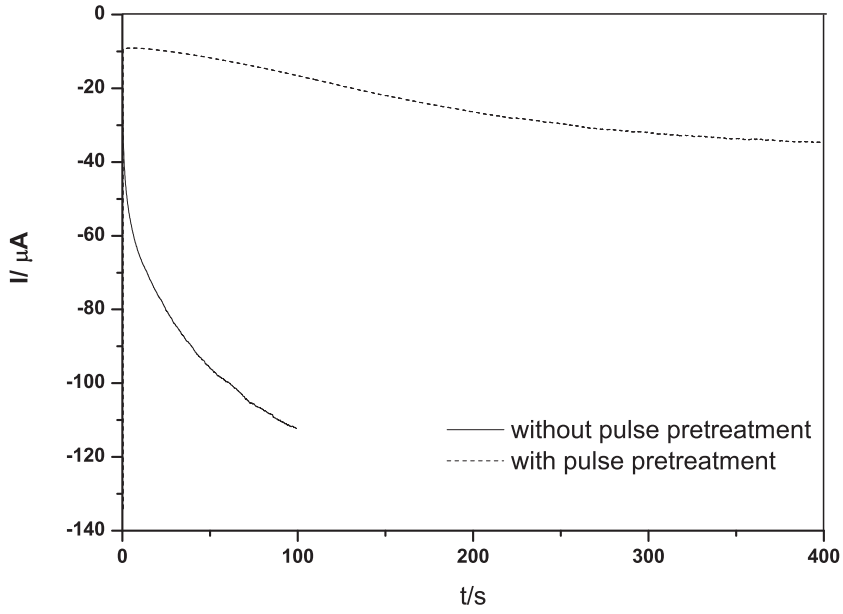

Figure 2.8: Comparison of two potentiostatic current-time transients curves of Au electrodeposition on Si with and without pulse pretreatment. In the one-step potential case, potential for electrodeposition was selected as -1V/SCE. Gold atoms deposited accompanied with nucleation. In the pulse pretreatment case, a pulse of -1.2V/SCE during 0.5 second was given before applied a -0.7V/SCE potential.

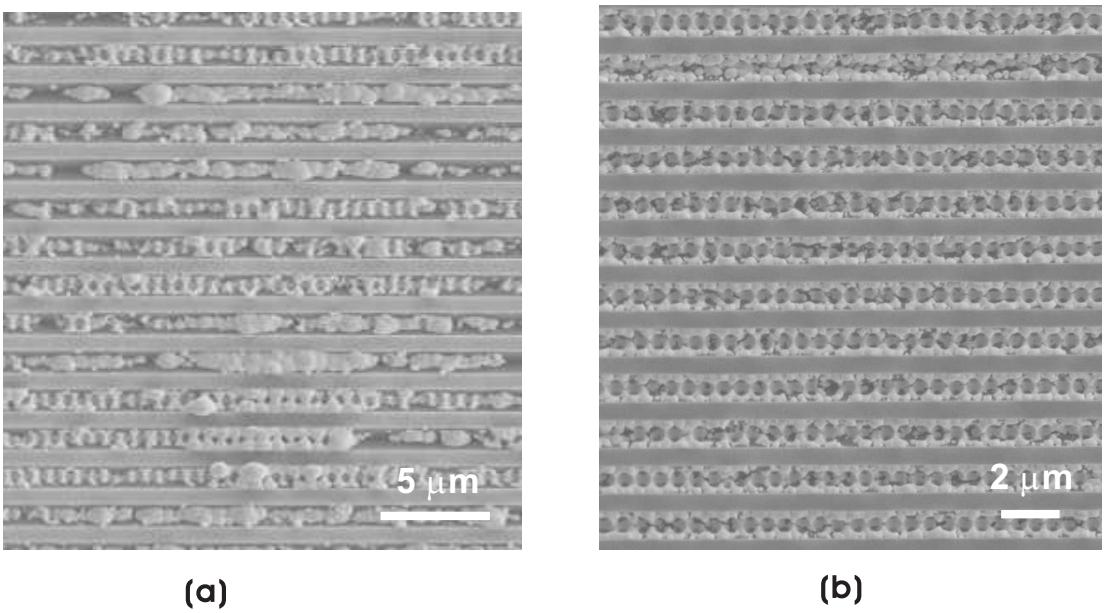

Figure 2.9: SEM images for comparison of two gold inverse sphere arrays electrodeposition on Si with/without pulse pretreatment. (a) Gold deposition without pulse pretreatment. Gold structure is not uniform. (b) Gold deposition with pulse pretreatment. Gold structure is nearly uniform.

2.4.3 Ni Film on Si

Based on a voltammogram (shown in Fig. 2.10) with the scan range from 0.4 to -1.7V with 0.02V/s scan rate, only two mechanisms occurred in Ni electrodeposition on 1-2 Ω cm Si: The nucleation started after -1.0 V/SCE; Between -1.1 to -1.7V/SCE, the cathodic current was dominated by nickel deposition accompanied by the hydrogen evolution. Like Au electrodeposition on Si, the chronopotentiometry method was used for Ni. This method supplies a constant potential to the working electrode while chronoamperometry is to supply a constant current density for working electrode. For the Si samples with different surface areas, the chronopotentiometry method is more convenient to control the electrodeposition conditions. To obtain a continuous Ni film, a pulse pretreatment from -1.3 to -1.7 V/SCE during 0.2 second or 0.4 second is necessary. Critical potential -1.1 V/SCE is indicated as the appropriate deposit potential to result in a uniform film. Moderate increase in potential improved the film brightness while moderate decrease in potential improved the adhesion between Ni and Si.

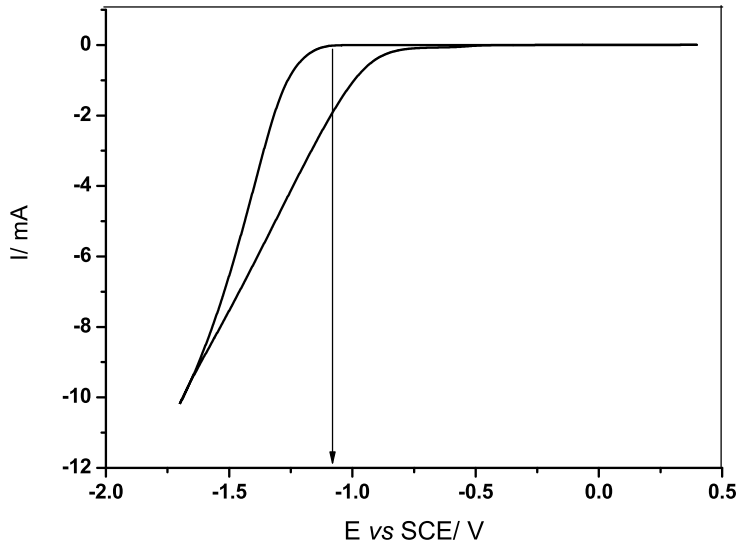

Figure 2.10: Cyclic voltammograms for Ni electrodeposition on 1-2 Ω cm Si. Potential scan rates were both 0.02 V/s and the scans both start from 0V/SCE. The wide scan range was from 0.4 to -1.7V/SCE.

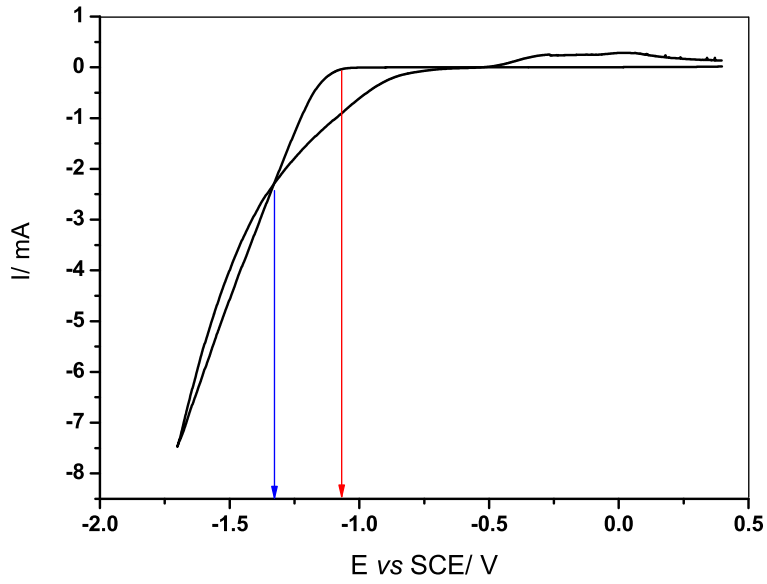

Figure 2.11: Cyclic voltammograms for Co electrodeposition on 1-2 Ω cm Si. Potential scan rates were both 0.02 V/s and the scans both start from 0V/SCE. The wide scan range was from 0.5 to -1.7V/SCE.

2.4.4 Co Film on Si

Fig. 2.11 shows an entire voltammogram of Co electrodeposition on 1-2 Ω cm Si with the the scan range from 0.5 to -1.7V with 0.02V/s scan rate. The cyclic voltmmogram indicates all types of mechanisms occurred:

- The nucleation started after -1.1 V/SCE.
- Between -1.1 to -1.3V/SCE, the cathodic current was dominated by cobalt deposition (the zone between blue and red arrows shown in fig. 2.11). The deposit potential can be selected in this zone.
- After -1.3V/SCE, the cathodic current was dominated by the hydrogen evolution. A pretreatment pulse can be selected in this zone.
- Between 0.5 to -0.5V/SCE, the cathodic current was reversed by Co reduction.

Fig. 2.12 shows two transient curves of Co electrodeposited on Si. In the Galvanostatic potential-time transient curve, a pulse of -1.09 mA during 0.4 second was

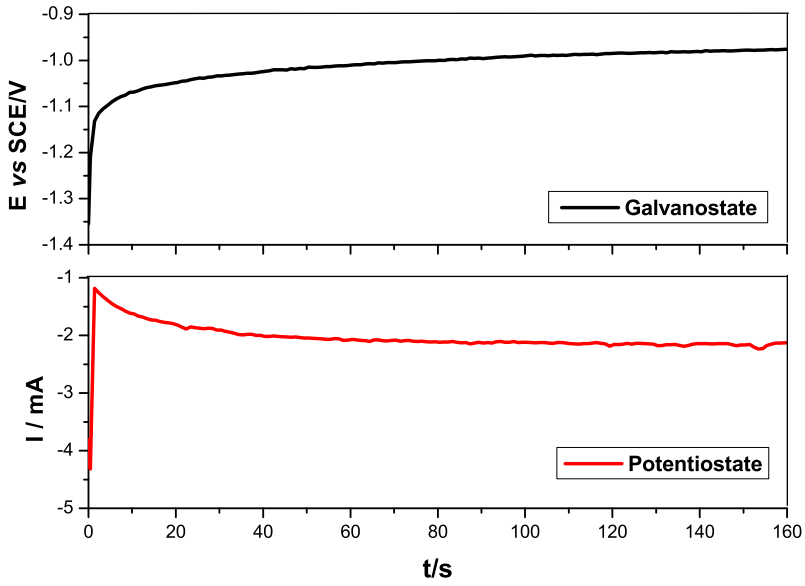

Figure 2.12: Comparison of two methods of Co electrodeposited on Si. In the Galvanostatic potential-time transient curve, a pulse of -1.09 mA during 0.4 second was given before a constant current -0.82 mA was applied. In the potentiostatic current-time transient curve, a pulse -1.5V/SCE during 0.4 second was given before a constant potential -1.1 V/SCE was applied.

given before applying a -0.82 mA constant current. This case indicates that during the sharp pulse, most of the nuclei formed on the silicon surface, then under the low deposition current density the Co film grows nearly without nucleation. In the potentiostatic current-time transient curve, a pulse of -1.5V/SCE during 0.4 second was given before applying a -1.1 V/SCE potential. This case indicates that after the sharp pulse, in the following 20 seconds, the amount of Co nuclei kept increasing. It resulted in a rough Co film.

Compared with Ni, it is more difficult to create a properly distributed Co nuclei layer on Si surface. So it requires higher accuracy of the potential-current conditions to control the electrodeposition process. As illustrated in Fig. 2.2, the current-potential relationship of electrodeposition is exponential. It is hence better to select a fixed current as the deposition condition than a fixed potential. So unlike the application of chronopotentiometry in nickel electrodeposition, chronoamperometry is used for Co electrodeposition on Si.

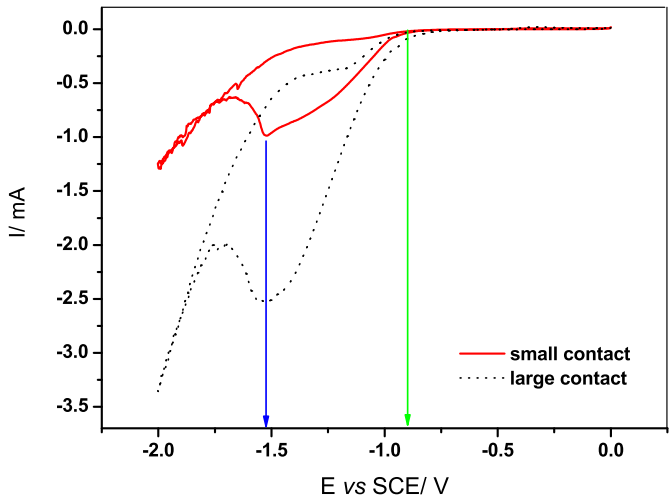

Figure 2.13: Cyclic voltammograms of Ni electrodeposition on 0.01-0.02 Ω cm Ge. Potential scan rates were both 0.02 V/s and the scans both start from 0V/SCE. The wide scan range was from 0 to -2 V/SCE.

2.4.5 Ni Film on Ge

In the voltammogram of Ni electrodeposition on 0.01-0.02 Ω cm Ge (shown in fig. 2.13), the two contacts with different areas indicate the same critical potentials at approximately -1.5V/SCE (the blue arrow in fig. 2.13) and approximately -0.9V/SCE (the green arrow in fig. 2.13). Therefore, the deposit potential zone is from -0.9 to -1.5 V/SCE.

Whether a pulse was applied or not, the Ni films on the Ge surface were developed smoothly and adhesively. This low sensitivity of the potential-current condition during electrodeposition allows the use of either the chronopotentiometry or the chronoamperometry method. Fig. 2.14 shows a typical Galvanostate potential-time transient curve of Ni on Ge. Though this process did not use a sharp pulse, the nucleation completed in the preliminary stage, and the film grew up uniformly without nucleation.

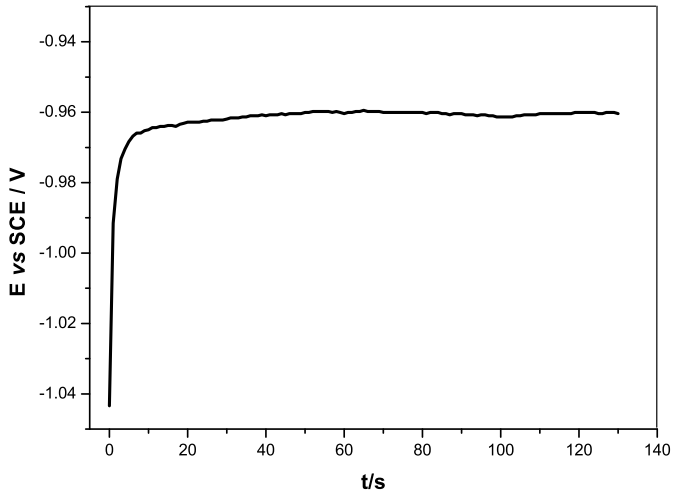

Figure 2.14: Galvanostate potential-time transient curve of Ni electrodeposition on 0.01-0.02 Ω cm Ge, applied a -1.5 mA constant current without pulse.

2.5 Conclusions

The principle of electrodeposition in the beginning of this chapter outlines the fundamental knowledge of metals electrodeposition on semiconductors. The experimental details, which includes the equipment setup and the recipes of different metal electrodeposition solutions are introduced. The results presented and discussed in this chapter reveal that different metal electrodepositions on different semiconductors require a series of distinct system parameters. For Au or Ni film on Si, it is suitable to use the chronoamperometry method after a pulse. For Co film on Si, chronopotentiometry with pulse pretreatment is the proper method. For Ni film on Ge, chronopotentiometry or chronoamperometry with or without pulse pretreatment, cause a high quality film.

Chapter 3

Ferromagnet-Si Schottky Barriers

3.1 Introduction

Metal-semiconductor contacts can be fabricated by various methods, such as thermal evaporation, chemical decomposition, electron-gun bombardment, sputtering, or plating of metals onto chemically etched substrates[18]. Both chemical vapour deposition (CVD) and physical vapour deposition (PVD) had been widely used for the deposition of (magnetic) metal films (such as Nickel, Cobalt) on semiconductor materials and these methods could fabricate a series of uniform devices. However, in our work, electrodeposition was selected. The essential distinction between electrodeposition and evaporation is that the metal atoms in electrodeposition process have low thermal energy when they deposit on the semiconductor surface, which helps to form a sharp interface between metal and semiconductor. In contrast, the metal atoms with the relative higher thermal energy in the evaporation process mix easier with the semiconductor surface and form a thin layer of metal-semiconductor compound shorting or modifying the Schottky barrier. In addition, electrodeposition is a mature technology which requires only simple equipment at low cost.

In this chapter, the background of Schottky barriers is introduced. The results of a series of electrodeposition experiments are presented. Electrodeposition of Ni and Co films directly on patterned Si substrates has been achieved through the methods introduced in section 3.3. I-V and C-V measurements were performed and the results reveal that electrodeposited ferromagnet-Si junctions show lower reverse bias leakage

for lowly doped Si and clear evidence of thermionic field emissions at high Si doping. This confirms the potential of these Schottky barriers to be used for spin injection and detection in spin FET, and will be discussed in the next chapter.

3.2 Fundamentals of Schottky Barrier

3.2.1 Working Principle of Schottky Barrier

Metals and semiconductors have different work functions. When a metal makes contact with n-type semiconductor, the Fermi levels in these two materials must be equal at thermal equilibrium while the vacuum level must be continuous. So these two requirements determine the band diagram of the ideal metal-semiconductor contact, as shown in Fig. 3.1(b). The difference between the metal work function and the semiconductor electron affinity is regarded as the barrier height Φ_B. Meanwhile, the electrons in the conduction band trying to move into the metal should have enough energy to cross a built-in potential V_{bi}, which is the difference of the barrier height Φ_B and the distance between the bottom of the conduction band and the Fermi level V_n.

A metal-semiconductor contact forms a Schottky barrier when barrier height $\Phi_B \gg$ kT, where k is Boltzmann's constant[19]. Schottky barriers work similarly to a one-sided abrupt p-n junction. But the crucial difference is that the majority carriers induce the current transport in a Schottky barrier while the minority carriers induce the current transport in a p-n junction. Actually, there are 4 basic transport processes under the forward bias [20], which are illustrated in Fig. 3.2:

1. Electrons overcome the potential barrier and move from the semiconductor into the metal. This process is dominant for the current transport in Schottky diodes if the silicon doping concentration is lower than 10^{17} cm^{-3} at room temperature.

2. Tunneling current flows through the barrier. This process will dominate significantly for heavily doped semiconductors, both in forward and especially in reverse bias.

3. Minority carriers are injected from the metal into the semiconductor.

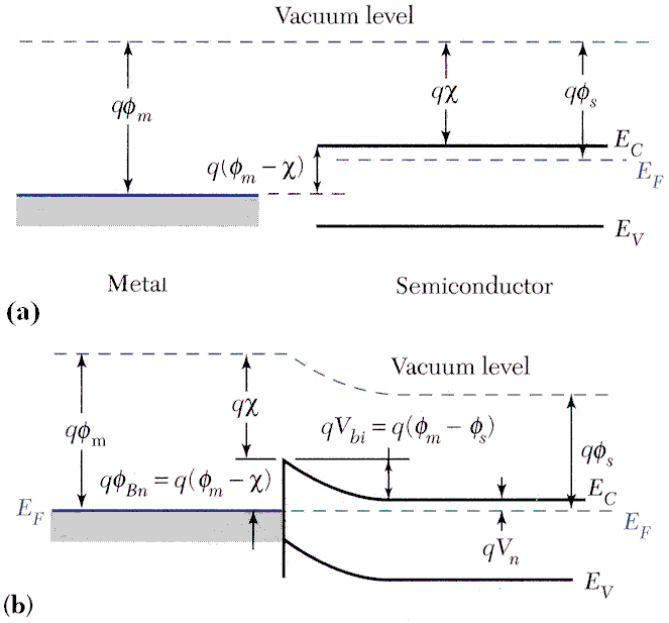

Figure 3.1: Energy band diagrams: (a) An isolated metal adjacent to an isolated n-type semiconductor under thermal nonequilibrium condition. (b) A metal-semiconductor contact in thermal equilibrium [19].

4. Carriers recombine in the space-charge region.

In addition, there is another transport type leakage current existing due to the interface quality and the high applied voltage, which is difficult to represent in Fig. 3.2. The reason for the leakage current is the high electric fields that exist at the metal periphery in Schottky diodes. These fields cause the edge effect [21].

For low-mobility semiconductors, the diffusion theory can be used to described the transport process while the thermionic emission theory is applied for high-mobility semiconductors. Silicon is a high-mobility type semiconductor, so the first transport process can be described by the thermionic emission theory [22] as shown in Fig. 3.3. In Fig. 3.3(a), the current densities balance at thermal equilibrium was shown. The electron flow from the semiconductor into the metal is equal to the electron flow from the metal into the semiconductor. So the net current is zero. When a forward bias V_F is applied to the contact (Fig. 3.3 (b)), the electrostatic potential difference across the barrier is decreased and the electron density at the interface is increased. It results in the electron flow from the semiconductor into the metal being larger than the opposite flow. The reverse bias condition is very different, as shown in Fig. 3.3(c).

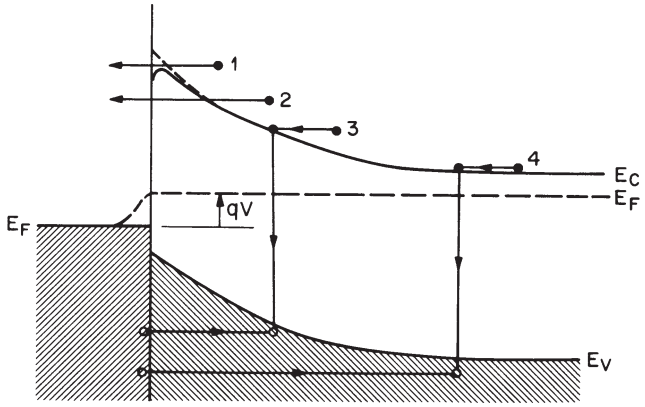

Figure 3.2: Four basic transport processes under forward bias [20].

Here, the barrier is not decreased when a voltage is applied. The reserve bias current remains very low, resulting in a rectifying behaviour.

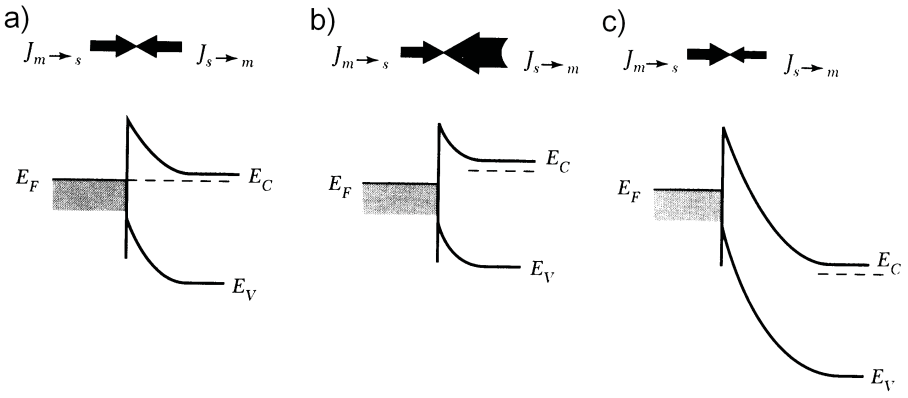

Figure 3.3: Current transport by the thermionic emission process. a) Thermal equilibrium; b) Forward bias; c) Reverse bias [19, 22].

3.2.2 I-V Characteristics of Schottky Barrier

Illustrated by the ideal I-V curve (Fig. 3.4), the Schottky barriers' parameters can be introduced: the practical current-voltage characteristic of a Schottky barrier under thermionic emission condition [23] is

$$I = I_S \cdot e^{qV/\eta kT}(1 - e^{-qV/kT}) \tag{3.1}$$

$$I_s = AA^*T^2 \cdot e^{-q\phi_{Bn}/kT} \tag{3.2}$$

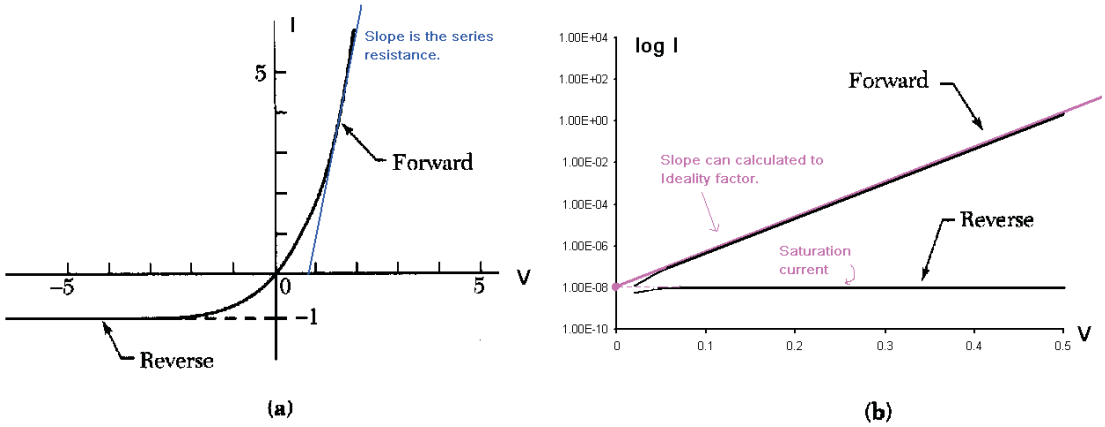

Figure 3.4: Ideal current-voltage characteristics of Schottky barriers: (a) I-V cartesian plot. (b) |I|-|V| semilog plot.

where V is the applied voltage, q is the elementary charge, which is 1.6×10^{-19} C, I_S is the saturation current, A is the active contact area, and ϕ_{Bn} is the barrier height. A^* is the effective Richardson constant (in units of A/(K^2-cm^2)), which is expressed as

$$A^* = 4\pi m^* q k^2 / h^3 \tag{3.3}$$

where h is the Planck constant ($6.63 \times 10^{-34} J \cdot s$), m^* is the semiconductor effective mass. Substituting the values of the constants in Eq. 3.3, the effective Richardson constant has the value

$$A^* = 120(m^*/m_e) A K^{-2} cm^{-2} \tag{3.4}$$

where m_e is the free-electron mass.

For semiconductors with spherical constant-energy surfaces such as gallium arsenide, A^* is independent of direction. The A^* for gallium arsenide is 8.64 $AK^{-2}cm^{-2}$. But for semiconductors with anisotropic constant-energy surfaces such as silicon and germanium, A^* depends on the orientation even if the crystal has cubic symmetry. For $< 100 >$ n-type silicon, $A^* = 246\ AK^{-2}cm^{-2}$ and for $< 111 >$ n-type silicon $A^* = 258\ AK^{-2}cm^{-2}$. It should be explained that the value of A^* for silicon is much larger then that for gallium arsenide, partly because of the larger effective-mass components and partly because of the six valleys in silicon.

If the applied voltage V is much greater than 3kT/q ($\gg$0.078V), the exponentialpart in Eq. 3.1 dominates, and the equation can be written in the simpler form

as

$$I = I_S \cdot e^{qV/\eta kT} \tag{3.5}$$

$$\ln I = \ln I_S + \frac{q}{\eta kT} V \tag{3.6}$$

In this approximation, the intercept gives the value of I_S and the ideality factor η can be derived from the slope. With the known value of the active contact area A, J_S can also be easily calculated. Using equation 3.2 and the area to convert to current density, the barrier height of the contact can be worked out:

$$\phi_{Bn} = -\frac{\ln (J_s/A^*T^2)kT}{q} \tag{3.7}$$

3.2.3 C-V Characteristics of Schottky Barriers

Although Equation 3.7 is very instructive, it requires the Richardson constant to be known to derive the barrier height. Although theoretical values can be calculated (as given in the previous section), they are subject to significant uncertainty. To enable extraction of the barrier height independent, A^*, temperature dependent measurement or capacitance voltage (C-V) measurement have to be carried out. In this section, the theoretical analysis of C-V curves as illustrated by the near ideal C-V curve in Fig. 3.5 will be described.

Neglecting the minority carriers, the definition of capacitance is

$$C = \frac{\partial Q_d}{\partial V_r} \tag{3.8}$$

where Q_d is the positive charge due to the uncompensated donors in the depletion region. From Gauss's theorem the charge due to the uncompensated donors[23] is given by

$$Q_d = (2q\varepsilon_S N_d)^{1/2}(V_{do} + V_r - \frac{kT}{q})^{-1/2} \tag{3.9}$$

where V_{do} is the diffusion voltage at zero bias. So that the expression 3.8 can be rewritten as

$$C = (\frac{q\varepsilon_S N_d}{2})^{1/2}(V_{do} + V_r - \frac{kT}{q})^{-1/2} \tag{3.10}$$

By differential C^{-2} with respect to V_r, the expression of the donor concentration is

$$N_d = \frac{2}{q\varepsilon_s}\left[\frac{1}{d(1/C^2)/dV_r}\right] \tag{3.11}$$

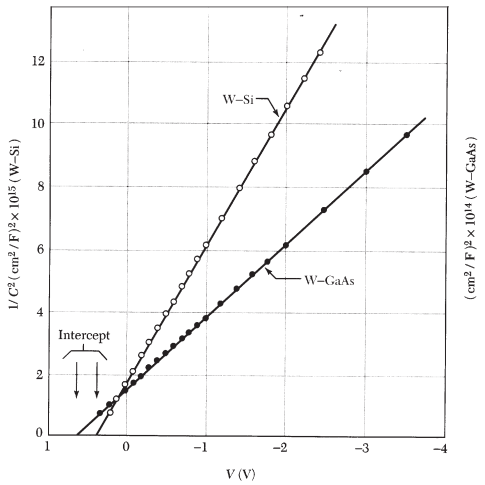

Figure 3.5: Ideal C-V characteristics of Schottky barriers[19].

The distance V_n of the Fermi energy below the conduction band is

$$V_n = \frac{kT}{q} \ln\left(\frac{N_c}{N_d}\right) \tag{3.12}$$

From the graph of C^{-2} as a function of V_r, the negative intercept (-V_i) is equal to (-V_{do}+kT/q). So that, the diffusion voltage at zero bias is

$$V_{do} = V_i + \frac{kT}{q} \tag{3.13}$$

Finally, as illustrated in Fig. 3.1, the barrier height Φ_{Bn} is equal to

$$\Phi_{Bn} = V_{do} + Vn = V_i + \frac{kT}{q} + Vn \tag{3.14}$$

3.3 Experimental Setup

Following the setup of the electrolytic cell, which has been described in section 2.3.1, the three electrodes were rinsed in nickelic electrolyte. All solvents and chemicals were of reagent quality and were used without further purification. Illustrated by Fig. 3.6(A), the process flow for the Ni-Si Schottky barriers is described. The circular and square patterns were transferred to silicon dioxide by conventional lithography. The SEM top view image of a pair of Schottky barriers is shown in Fig. 3.6(B) and (C).

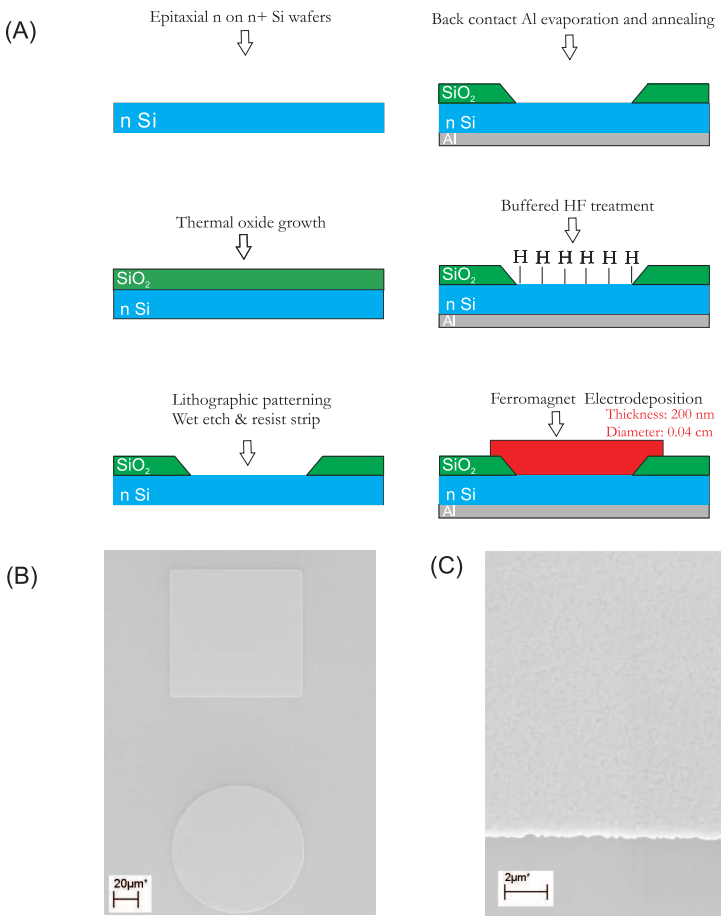

Figure 3.6: (A) Process flow for the fabrication of electrodeposited ferromagnet-Si Schottky barriers. (B) SEM image of the top view of a pair of SBs. (C) SEM image of the edge of a square contact.

There are three different resistivity type silicon substrates used in the experiments: 0.01 $\Omega \cdot cm$ - 0.0206 $\Omega \cdot cm$(low), 1 $\Omega \cdot cm$ - 2 $\Omega \cdot cm$(medium), and 10 $\Omega \cdot cm$ - 20 $\Omega \cdot cm$(high). However, the high resistivity silicon substrates are difficult to use for electrodeposition of nickel films due to the ohmic voltage drop in the Si wafers. As the medium resistivity Si wafers have low enough doping to suppress thermionic field emission, they are just as suitable for our purpose and in the following section, only the Schottky barriers on medium and low resistivity wafers are discussed. The I-V and C-V measurements of the deposited silicon substrates were taken, respectively, by an Agilent 4155C semiconductor parameter analyser and an Agilent 4280A C-V meter.

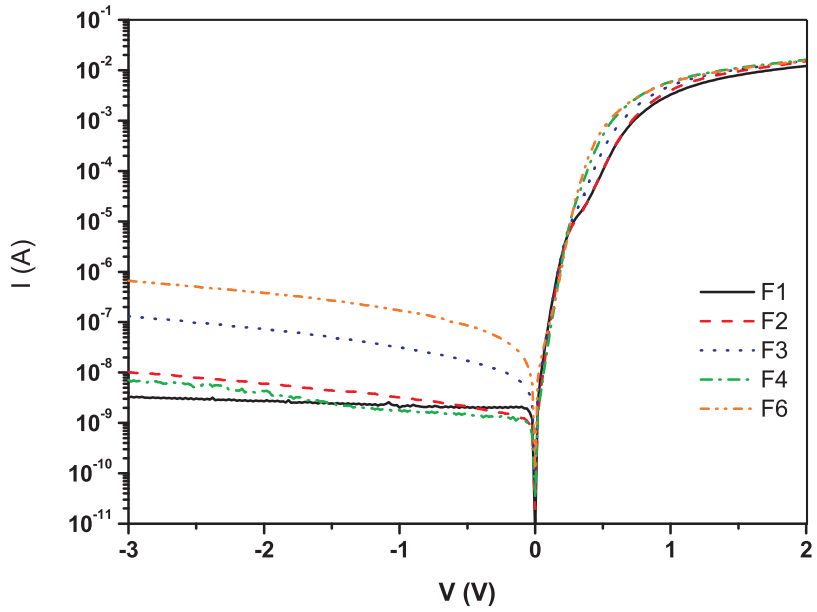

Figure 3.7: Room temperature I-V Characteristics of electrodeposited Ni-Si Schottky Barriers. The doped Si resistivity is 1-2 Ω-cm. All curves are from nominally identical circular contacts with 0.07cm diameter.

3.4 Experimental Results of Electrodeposited Ni-Si Schottky Barriers

3.4.1 I-V Characteristics Ni-Si Schottky Barriers

Fig. 3.7 shows the dependence of current on applied voltage of the Schottky contacts which were grown on the medium resistivity (1-2 Ω-cm) silicon wafer by nickel electrodeposition. All curves in this graphs are from different but nominally identical junctions. Table 3.1 lists the key parameters of these Schottky barriers.

Obviously, the Schottky barriers are high quality with low saturation currents, good barrier heights and low ideality factors. However, the I-V characteristics vary severely across nominally identical samples and exhibited a deviation from linearity appearing in the vicinity of 0.3 V at forward bias. The phenomenon of this deviation can be explained by considering the junction to be inhomogeneous. Such junctions can be described by two or several Schottky barriers in parallel as described. The total current is hence the resultant of two currents flowing in parallel:

$$I = I_{S1} \cdot e^{(V - I_1 \cdot R_{S1}) \cdot \frac{q}{kT}} + I_{S2} \cdot e^{(V - I_2 \cdot R_{S2}) \cdot \frac{q}{\eta kT}} \tag{3.15}$$

Contact Name	Side (cm)	Area (cm^2)	I_S (A)	J_s (A/cm^2)	Φ_{Bn} (V)	η	R (Ω)
D31-F1	0.07	4.90×10^{-3}	5.03×10^{-9}	1.03×10^{-6}	0.77	1.28	112.98
D31-F2	0.07	4.90×10^{-3}	2.14×10^{-9}	4.36×10^{-7}	0.80	1.14	94.49
D31-F3	0.07	4.90×10^{-3}	4.91×10^{-9}	1.00×10^{-6}	0.77	1.25	97.16
D31-F4	0.07	4.90×10^{-3}	1.17×10^{-9}	2.38×10^{-7}	0.81	1.07	100.14
D31-F6	0.07	4.90×10^{-3}	4.28×10^{-9}	8.73×10^{-7}	0.78	1.33	104.65

Table 3.1: The Parameters of Schottky Barriers' I-V Characteristics. The Schottky contacts are made on the medium resistivity (1-2 Ω-cm) silicon wafer by nickel electrodeposition. These parameters are calculated from I-V measurements. All samples are nominally identical squares.

where the first term is considered to be the current I1 from an ideal Schottky Barrier and the second term is considered to be the current I2 from a non-ideal channel. The non-ideal term can be rewritten as

$$I2 = I_{S2} \cdot (e^{V \cdot \frac{q}{\eta kT}} - e^{-I2 \cdot R_S \cdot \frac{q}{\eta kT}}) \tag{3.16}$$

$$I2 \cdot e^{I2 \cdot R_S \cdot \frac{q}{\eta kT}} = I_{S2} \cdot e^{V \cdot \frac{q}{\eta kT}} \tag{3.17}$$

This set of equations can not be solved analytically and a mathematical algorithm has to be deployed. This algorithm is based upon the Lambert W-function:

$$f(W) = W \cdot e^W \tag{3.18}$$

where W is taken equal to

$$W = I2 \cdot R_S \cdot \frac{q}{\eta kT}$$

.

Equation 3.17 can hence be written as

$$W \cdot e^W = (I_S \cdot e^{V \cdot \frac{q}{\eta kT}}) \cdot R_S \cdot \frac{q}{\eta kT} \tag{3.19}$$

In Matlab, if the value of f(W) is known, the inverse function of Lambert W-function can be derived. After using the independently derived parameters at reverse bias and high voltage of the I-V characteristics: η, Is, Rs, the value of current can be calculated according to the value of bias voltage. Therefore, the simulations to fit the experimental I-V curves were carried out by adjusting 6 variables: R_{S1}, $\eta 1$, I_{S1}, R_{S2}, $\eta 2$ and I_{S2}. Table 3.2 and Fig. 3.8 and 3.9 show the simulation results

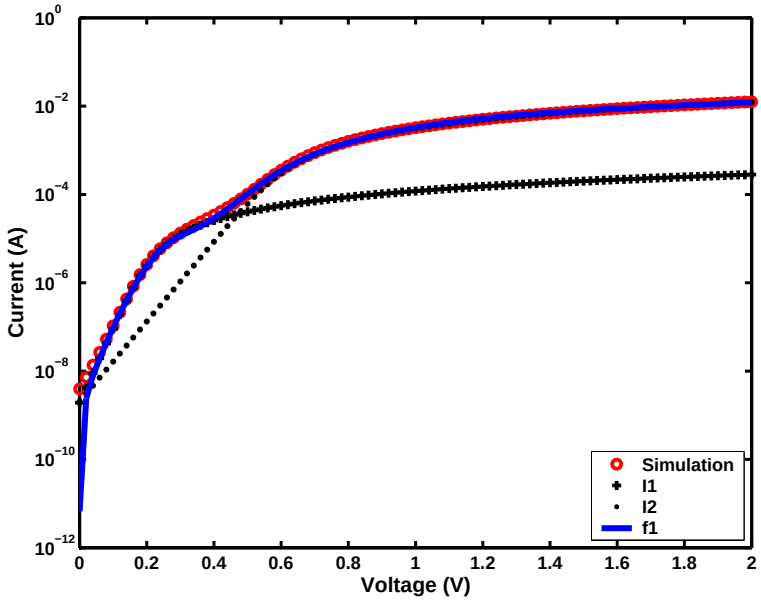

Figure 3.8: Fitting of single nominal identical Ni-Si(1-2 Ω·cm)Schottky Barrier with the phenomenological model of two parallel Schottky barriers.

which have been achieved by applying a Lambert W-function in Matlab. The results show that the experimental data can be completely reproduced by only changing the ideality factors in different contacts while other parameters are fixed. So it proves the influences of inhomogeneous junction problem are different among contacts and that the electrodeposition process is not yet optimised. In subsequent studies in the next sections we will analyze this problem in more detail and find ways to avoid to produce the inhomogeneous Schottky diodes.

	Current I			Current II		
	$Rs1(\Omega)$	Ideality factor $\eta 1$	Saturation current I_{S1}(nA)	$Rs2(\Omega)$	Ideality factor $\eta 2$	Saturation current I_{S2}(nA)
D31-F1	6000	1.00	1.912	101.86	1.85	2.0304
D31-F2					1.85	
D31-F3					1.60	
D31-F4					1.40	
D31-F6					1.30	

Table 3.2: The Parameters of Schottky Barriers' I-V Characteristics by simulation. The Schottky contacts are made on the medium resistivity (1-2 Ω-cm) silicon wafer by nickel electrodeposition. These parameters are achieved from Matlab simulations.

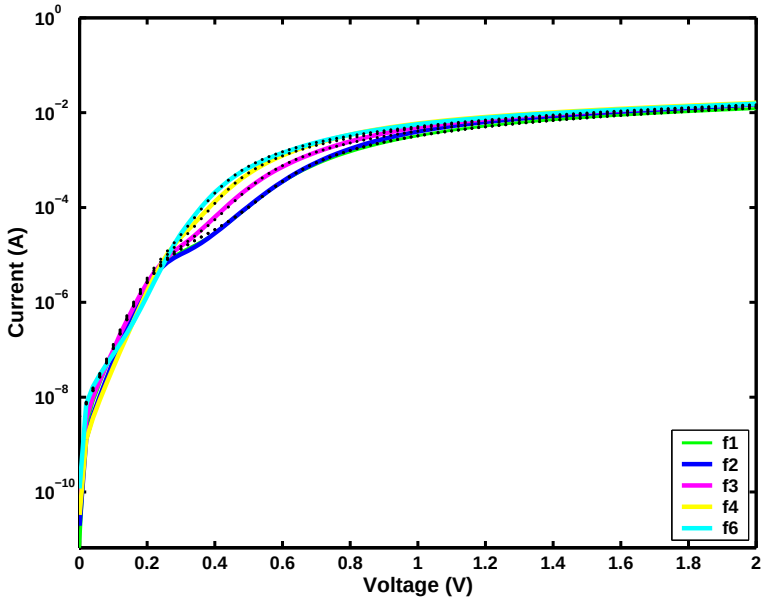

Figure 3.9: Fitting of five nominal identical Ni-Si(1-2 Ω·cm)Schottky Barriers with the phenomenological model. The black dots represent the original I-V curves from measurements. The colour lines represent the simulation curves respectively.

3.4.2 C-V Characteristics of Ni-Si Schottky Barriers

Fig. 3.10 shows the dependence of $1/C^2$ on applied voltage of the Schottky contacts made on the medium resistivity (1-2 Ω-cm) silicon wafer by nickel electrodeposition. The graph shows the predicted linear behaviour as explained in section 3.2.3. From the slope and intercept, the various parameters are extracted. For the three samples, the parameters were scaled by the different contact areas. Table 3.3 lists the doping concentration of the silicon substrates and the barrier heights of Schottky barriers from the calculation of C-V curves.

Contact Name	Side (cm)	Area (cm^2)	N_d (cm^{-3})	V_n (V)	V_i (V)	V_{do} (V)	Φ_{Bn} (V)	ρ (Ω·cm)
A31-B	0.15	2.25×10^{-2}	3.20×10^{15}	0.24	0.59	0.62	0.86	1.22
A31-D	0.10	1.00×10^{-2}	2.79×10^{15}	0.24	0.63	0.65	0.89	1.40
A31-F	0.07	4.90×10^{-3}	3.35×10^{15}	0.23	0.65	0.68	0.91	1.17

Table 3.3: The Parameters of Schottky Barriers' C-V Characteristics. The Schottky contacts are built in the medium resistivity (1-2 Ω-cm) silicon wafer by nickel electrodeposition. These parameters are calculated from C-V measurements. The calculation method was described in section 3.2.3.

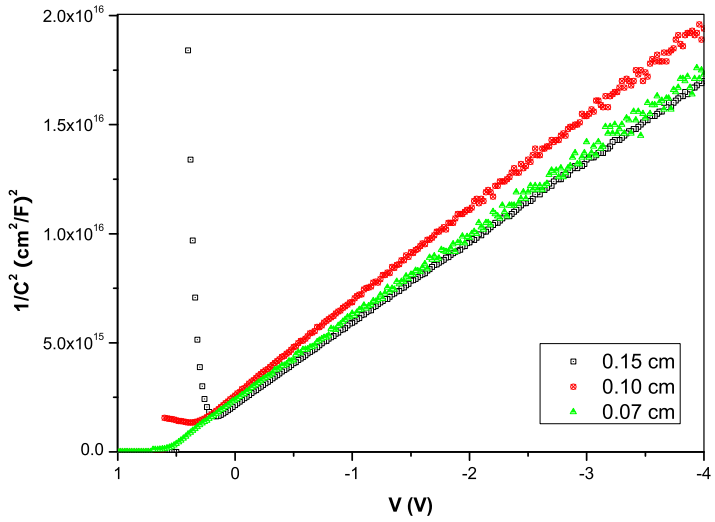

Figure 3.10: Room temperature C-V Characteristics of electrodeposited Ni-Si Schottky Barriers. The doped Si resistivity is 1-2 Ω-cm. The cross sections of all contacts were squares with 0.15cm, 0.10cm and 0.07cm side, respectively.

As explained in equation 3.11, the slope of the C-V curves in fig. 3.10 is proportional to the doping concentration in the semiconductor. In the case of the medium doped silicon wafers the doping concentration n =(3.0 ± 0.2) $\times 10^{15}$ cm^{-3}.

To convert to the more common parameter Resistivity ρ, one has to realize that ρ is the reciprocal value of the conductivity σ, defined as the proportionality constant between electric field E and current density J:

$$\rho = \frac{E}{J} \tag{3.20}$$

As the resistivity of n-type silicon is determined by electrons solely, ρ can be expressed as:

$$\rho = \frac{1}{qN_d\mu_n} \tag{3.21}$$

where N_d is the electron concentration and μ_n is the electron mobility. The bulk mobility of silicon is well known as is shown in Fig. 3.11. At the current dopant concentration, impurity scattering does not yet play a role in reducing the mobility. Hence the electron mobility μ_n can be taken as 1600 cm^2/V·s. This is used to arrive at the resistivity of the silicon substrates of $1.3 \pm 0.1\ \Omega \cdot cm$ (The corresponding values of ρ for the three different area contacts are listed in table 3.3). This value is in the

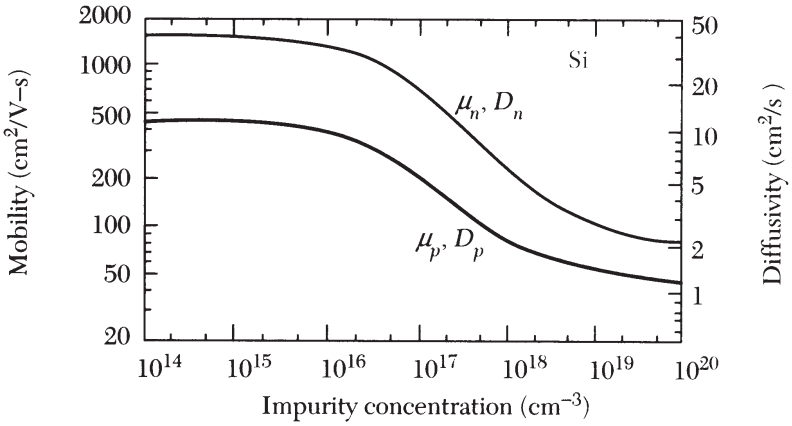

Figure 3.11: Mobilities and diffusivity in Si at 300K as a function of impurity concentration [24].

range of the specified nominal doping concentration of 1-2 Ω·cm. This shows that the fabricated devices and analysis were of a good standard. It also indicates that C-V measurements is a method for determining doping concentration or resistivity that can compete with the four-point probe method [24, 25] and Hall effect measurements [26] with respect to accuracy and convenience.

From a comparison of Table 3.1 and Table 3.3, it's clear that the Schottky barrier values determined by I-V measurements are lower than those which are calculated from C-V measurements. The difference is about 0.1 V. The main reason is the different effects of the spatial distributions of potentials on barrier capacitance and dc current measurements. The capacitance C is derived from the displacement of current:

$$\frac{dE}{dt} = i\omega C \tag{3.22}$$

In other words, the mean electric field E at the metal/semiconductor interface determines the width of the space-charge region. The frequency ω from the time periodic change of the width of the space-charge region determines the capacitance C. Short-wavelength potential fluctuations at the metal/semiconductor interface are screened out at the edge of the space-charge region. It results in the capacitance C being insensitive to potential fluctuations on a length scale of less than the space- charge width. Hence, capacitances are expected to measure only the mean values $\bar{V}_d$ and $\bar{\Phi}_b$. On the other hand, the dc current I across the interface depends exponentially on

Φ_b and thus subtly on the detailed barrier distribution at the interface. Any spatial variation in the barriers causes the current I to flow firstly through the barrier minima [27]. This confirms the earlier assumption that our Schottky contacts cannot be considered uniform and that the barrier height shows spatial variations. Up to this point we have assumed that the contacts can be described by two barriers heights without giving a justification of this assumption. In the next section, a more detailed quantitative analysis of these inhomogeneous Ni-Si contacts is carried out.

3.4.3 Thermionic and Thermionic Field Emission at Ni-Si Schottky Barriers

In order to further investigate the quality of Ni-Si SBs obtained by electrodeposition, low temperature J-V-T measurements were performed. The range was from 86 K to 320 K with steps of 10 K. The forward bias characteristics are shown in Fig. 3.12. For clarity, only 7 different temperatures are plotted in this diagram. As expected from the thermionic emission theory, J_S is reduced drastically with reducing temperature. The reverse leakage current is also reduced following J_S (not shown in Fig. 3.12). Below 190 K the reverse leakage is lower than 1 pA which is the lower current limit of the measurement setup that has been used.

The saturation current density was extrapolated from the J - V measurements for different temperatures and the activation energy diagram was acquired as shown in Fig. 3.13. A temperature independent SB height would result in a straight line on the activation energy diagram. A fit with $\phi_B = 0.70$ V is shown as a solid line in Fig. 3.13. This line fits only the high temperature experimental results. For lower temperatures a deviation from a straight line is observed, indicating a temperature dependent SB height.

Several models for the explanation of the low temperature behaviour of SBs have been proposed[28]. In the T_0 effect model[29], the experimental data are fitted for temperatures above 125 K, but no physical origin is known. In the Werner model[27], an excellent fit is obtained through the whole range of the measurements. In this model, the Schottky barrier height is assumed to be inhomogeneous with a spatial variation. The area of the junction at a certain barrier height follows a Gaussian dis-

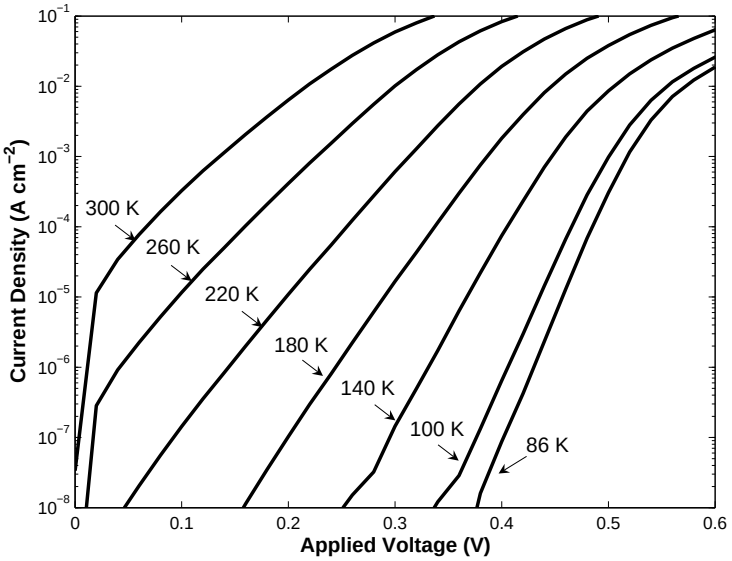

Figure 3.12: Low temperature, forward bias J-V characteristics of a circular electrodeposited Ni-Si SB with 0.15 cm diameter.

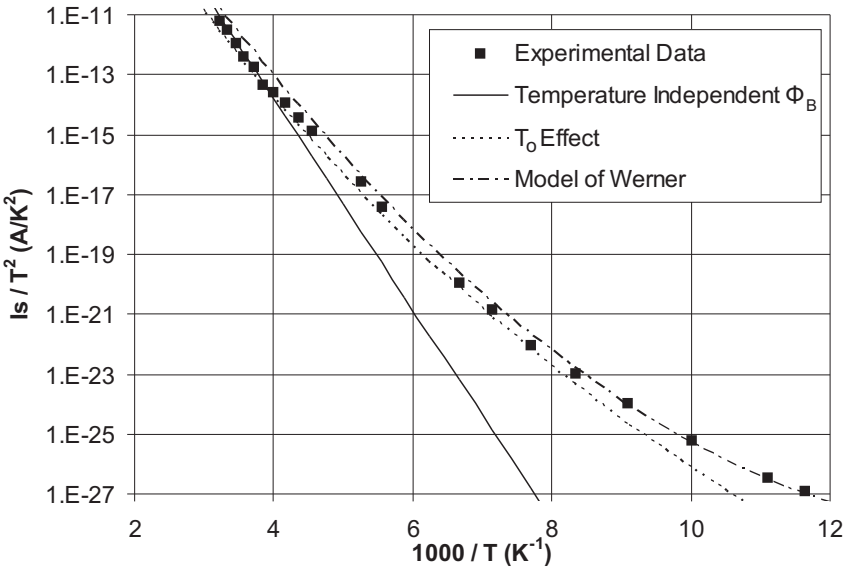

Figure 3.13: Activation energy diagram (Arrhenius plot) of the same electrodeposited Ni-Si contact as in Fig. 3.12. The measurements are fitted by using a temperature-independent SB height thermionic emission model, the T_0 effect model and the model of Werner and Guttler. The analysis of the T_0 effect model and the model of Werner and Guttler is contributed by Dr. Michail Kiziroglou.

tribution, and this model can hence be considered to be an elaborate expansion on the bimodal barrier height model introduced in the previous section. This model explains all data in a straightforward way without having to rely-on-physical parameters. The modeling analysis of the Ni-Si Schottky barriers fabricated by electrodeposition is described in more detail in our paper, cited as Ref [30], in which we further reduce the series resistance of the Si wafer by growing n-type Si on n+ type Si.

Theoretically, tunnelling current is considered as the dominant transport mechanism at highly doped Si Schottky barriers[31]. As shown in Fig. 3.14, the J-V-T plots of Ni-Si contacts are not positive current-temperature coefficients all along. These measurements were taken with a temperature step of 10 K. For clarity, only five curves are plotted in Fig. 3.14. In the forward bias, a minor increase of J with T is observed. In the low reverse bias, J also increases with T. However, for temperatures below 250 K, at around -1 V to -1.5 V a sudden slope increase is observed indicating a switch of the dominant transport mechanism. For reverse bias larger than -1.5 V, the temperature coefficient becomes negative. While Schottky barrier models predict the decrease of the barrier height with decreasing temperature[32], and the thermionic field emission theory can, under certain circumstances predict higher currents for lower temperatures[33], this is the first experimental observation of negative current-temperature coefficient at Schottky barriers. The detailed analysis of thermionic field emission at Ni-Si contacts is fully described in our paper[31].

3.5 Experimental Results of other Metal-Si Schottky Barriers

Although, it has been shown that electrodeposited Ni-Si contacts are excellent Schottky barriers, a number of limitations do exist, which hamper the application for Spintronic devices as discussed in the next Chapter. Firstly, to achieve magnetization reversal in a small magnetic field, it was necessary to improve uniaxial magnetic anisotropy. Ni electrodeposition on Si while applying a magnetic field was investigated. Secondly, the requirement to have two independently rotating magnetic materials, meant that another metal-Si contact had to be developed. For this reason, Co-Si Schottky barriers were also investigated. Thirdly, as discussed before, elec-

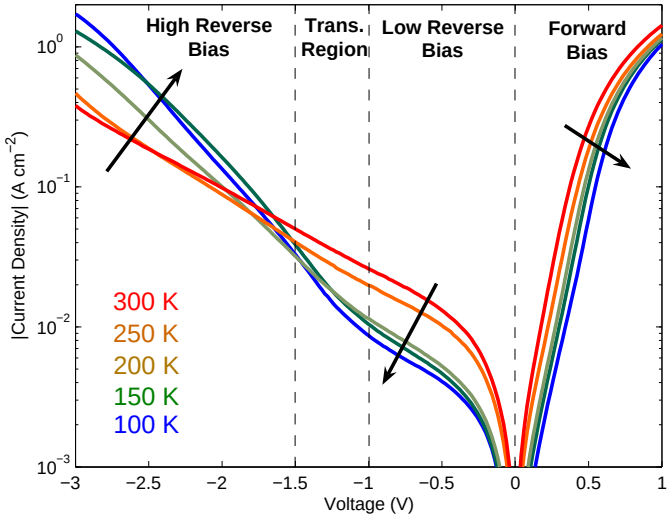

Figure 3.14: Low temperature J - V characteristics of an electrodeposited Ni-Si contact for highly doped Si. The contact was circular with diameter 1.5 mm. Arrows indicates decreasing temperature. This figure was plotted by Dr. Michail Kiziroglou.

trodeposition can only be used when the substrate is conducting enough. For the Vertical Spin Valves introduced in the next chapter this is not the case, and it was necessary to resort to evaporated junctions. Hence, evaporated Ni-Si, Co-Si Schottky barriers were also investigated and compared to electrodeposited junctions.

3.5.1 Ni Electrodeposition on Si with Magnetic Bias Field

For magnetoresistance measurements, it is important that a contact can have its magnetization reversal in a small well defined magnetic field. This requires uniaxial magnetic anisotropy, usually magnetization-induced. This plays an important role in the technical magnetization, and can be controlled in several ways. One method to create uniaxial anisotropy is inducing it by applying a magnetic field during deposition [34]. In this section some results of a series of electrodeposition experiments with a constant magnetic bias field are presented. Electrodeposition of Ni films directly on non-patterned Si substrates has been achieved through the methods introduced in section 2.4.3. The purpose of the experiments was to observe how the magnetic bias field during deposition would affect the crystal orientation, surface morphology and coercivity of the ferromagnetic film in order to have a uniaxial anisotropy emerging.

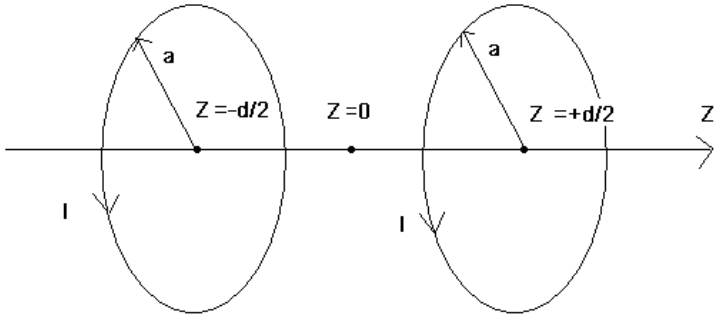

Figure 3.15: Scheme of Helmholtz coils. For a ideal Helmholtz coils, the radius of coils is equal to the half distance of the two centers of coils.

Helmholtz Coils calibration

Helmholtz coils are employed to yield the magnetic field for electrodeposition. Fig 3.15 shows the scheme of Helmholtz coils. The magnetic field of Helmholtz coils along the z-axis is expressed as

$$B_z = \frac{\mu_0 I a^2}{2[(d/2+z)^2+a^2]^{3/2}} + \frac{\mu_0 I a^2}{2[(d/2-z)^2+a^2]^{3/2}} \tag{3.23}$$

where μ_0 is magnetic permeability, and equal to 1.26×10^{-6} T·m/A. For ideal Helmholtz coils,

$$a = \frac{d}{2}$$

.

The magnetic field of the center on the z-axis (z=0) is now simplified as

$$B_z = \frac{8\mu_0 \cdot I}{5^{3/2} \cdot a} \tag{3.24}$$

Since the Helmholtz coils consists of two symmetrically parallel, coaxial circular loops, its characteristic is that the magnetic field of the center point is highly uniform [35] if each coil carries an equal electrical current flowing in the same direction. For a Helmholtz coils with N turns, the total magnetic field along the z-axis is proportional to the number of turns. Because the coils used in the experiment did not have a data sheet, the calibration was necessary before being able to use them in electrodeposition experiments. The relation of current and magnetic intensity were measured by a Hall probe, and experimental result is shown in Fig. 3.16. The H-I rate is 214.5 mT/A

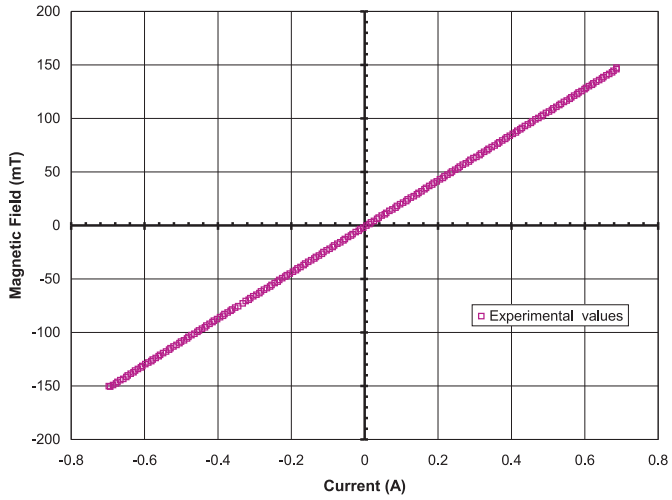

Figure 3.16: The H-I characteristics of Helmholtz coils by magnetic experiment. These coils yield the magnetic field for the electrodeposition experiment.

while the theoretical value according to Eq. 3.24 is 110 mT/A. There are two reason to cause the H-I relation not to be identical between the experimental value and theoretical value. Firstly, the number of turns is not an accurate value from a data sheet but an estimated value, as the details of the packing method are unknown. Secondly, these coils are not ideal Helmholtz coils because the radius of coil 'a' is not exactly equal to the half distance of two coil centres 'd'. So in the following experiments, the experimental values of magnetic field are used. **Experimental results**

Other than applying a magnetic field, the experiment setup of Ni electrodeposition on Si is similar to the experiment described in Chapter 2. All the samples have an electrochemical pretreatment consisting of a -1.9 V pulse voltage for 0.2 second to improve nucleation. The electrodeposit voltage is -1.3 V and the experiments are stopped when the monitoring PC shows the electrodeposition charge reached 1.17 C. This charge is calculated to get 300 nm thickness film in a 1 cm^2 area deposit window. The directions are parallel and perpendicular to the plane of the sample. Table 3.4 lists the parameters of electrodeposition in the case of zero and 75 mT magnetic field.

Scan Electron Microscope (SEM) Measurements

Deposition Time (sec)	Charge (C)	Current (mA)	Coils Current (A)	Magnetic Field (mT)	Field Direction
206.2	1.17	-5.56	0	0	-
238.2	1.17	-4.85	0.35	75	Perpendicular
172.2	1.18	-6.83	0.35	75	Parallel

Table 3.4: The parameters of electrodeposition applied the magnetic field.

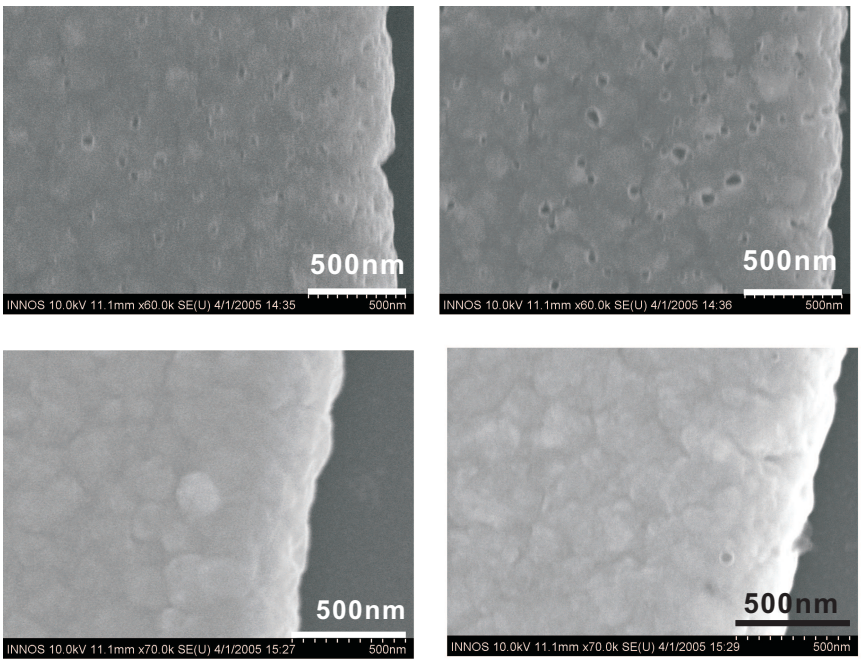

Figure 3.17: SEM micrographs of Ni films electrodeposited on Si under a magnetic field. Top-left: without magnetic field; Top-right:with a 75mT parallel magnetic field; Down-left:with a 75mT perpendicular magnetic field; Down-right:without a magnetic field.

SEM is used to observe the surface morphology. Fig 3.17 shows four samples deposited under 0 mT parallel, 75 mT parallel, 75 mT perpendicular and 0 mT perpendicular magnetic field respectively at 500 nm scale. The surfaces of parallel samples appear to have some small voids while the perpendicular samples have a continuous surface. However, this difference can not deduce any conclusion about the influence from the magnetic field because the two non-magnetic films were not identical. **X-ray Diffraction Measurements**

X-ray diffraction is a technique in crystallography, in which the pattern produced by the diffraction of x-rays through the closely spaced lattice of atoms in a crystal

Si	hkl	111	200	220	311	400		
	2θ	28.4	33.1	47.3	56.0	69.1		
Ni	hkl	111	200	220	311	222	331	420
	2θ	44.5	51.8	76.3	92.9	98.4	144.6	155.7

Table 3.5: The 2θ corresponding to crystal orientation of nickel and silicon.

is recorded and then analyzed to reveal the nature of the lattice. According to this principle of X-ray diffraction, the value of 2θ corresponding to crystal orientations of nickel and silicon can be read in table 3.5. Fig 3.18 shows a silicon $< 400 >$ peak, in the agreement with the orientation of the silicon wafer which is $< 100 >$. For a normal coupled 2θ scan, a symmetrical geometry is maintained such that the sample surface makes the same angle with respect to the incident and reflecting beams. Therefore, the diffraction from the single crystal substrate can only originate from the crystalline planes parallel to the sample surface [36]. In particular, for a $< 100 >$ oriented silicon wafer examined with Cu K radiation, the only diffraction peak expected is $< 400 >$ reflection because other $< x00 >$ reflections are forbidden due to their vanishing structure factors [37]. So the result validates that the x-ray diffraction measurements are correct. From Fig. 3.19, the effect of the Ni film electrodeposited without and with a constant magnetic bias field is rather ambigious. The film with a 75 mT perpendicular bias field, the reflection peak of (111) shows stronger preferred orientation than that of (200). However, neither of the films has perfect alignment along a direction.

Magnetic Measurements

Magnetic measurements on the samples prepared in a magnetic field were carried out to observe the coercivity. Due to the ECS fire, only the sample deposited in a parallelled 75 mT magnetic field applied was measured in-plane through three different directions, transversal, longitudinal and 45 degree angles, relative to the direction of the applied magnetic film during electrodeposition. Fig. 3.20 shows the hysteresis loops of the sample under those different directions. There was not a significant change of the coercivity in this parallel magnetic field case. The correlation between electrodeposition potential and physical and magnetic properties is further described in our paper [38].

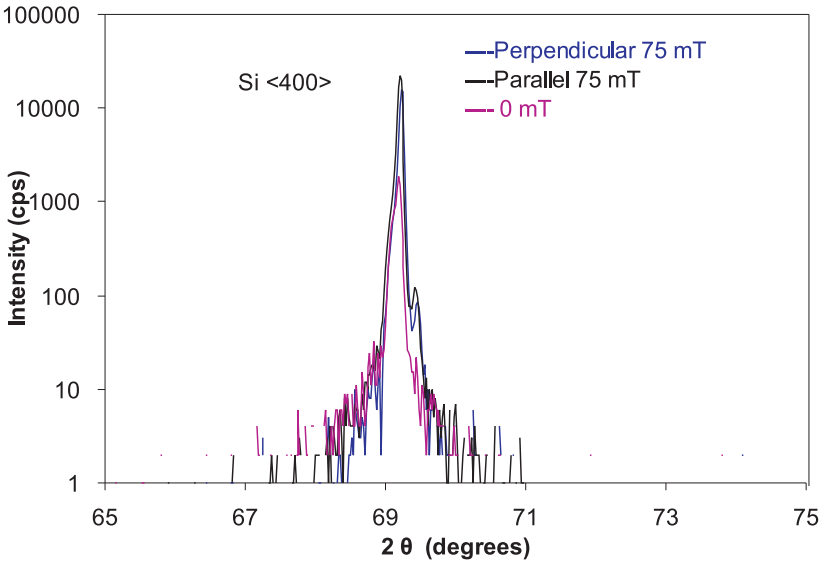

Figure 3.18: X-ray diffraction measurements of Si< 400 > crystal orientation.

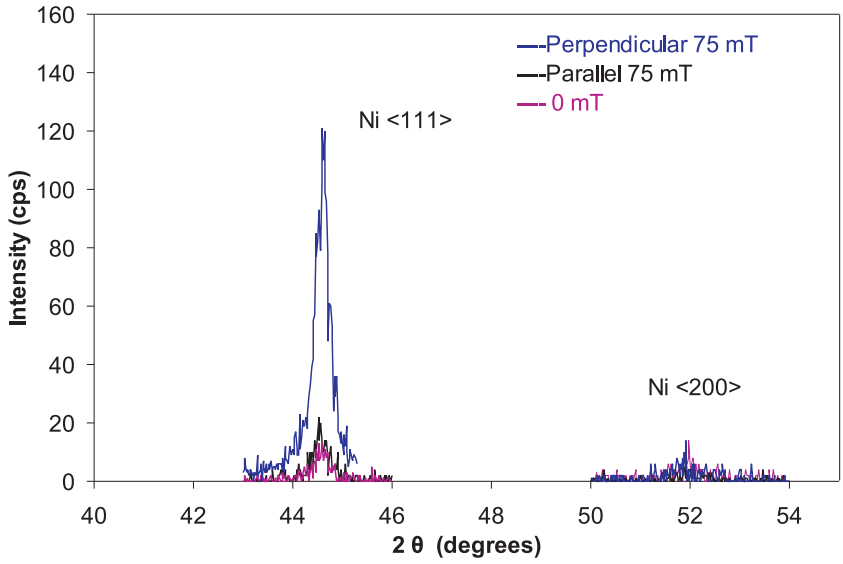

Figure 3.19: X-ray diffraction measurements of Ni crystal orientation.

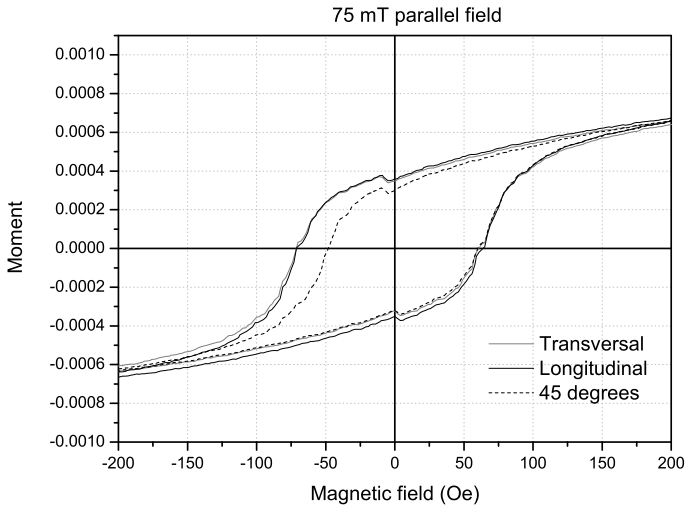

Figure 3.20: Hysteresis loop of the Ni film electrodeposited on Si under a magnetic field.

3.5.2 Electrodeposited Co-Si Schottky Barriers

As mentioned in section 2.4.4, Co electrodeposition requires the chronoamperometry method. Fig. 3.21 shows a comparison between room temperature J-V characteristics of electrodeposited Ni-Si and Co-Si Schottky barriers with the same Si doping level and same contact size. Table 3.6 outlines the extrapolated parameters of Co-Si and Ni-Si Schottky barriers. Though the optimization of Co electrodeposition is more difficult than Ni, the rectifying behaviours of Co-Si Schottky barriers on Si(1$\sim$2 $\Omega \cdot cm$)are even better than Ni-Si Schottky barriers with higher barrier height, lower saturation current density and lower ideality factor.

Low temperature J - V characteristics of an electrodeposited Co-Si Schottky Barriers is investigated by Fig. 3.22. It shows a series of J-V-T plots of a 1.5 mm diameter Co contact on 1-2 Ω·cm Si. These measurements were taken with a temperature step of 10 K. For clarity, only six curves are plotted in Fig. 3.22. This is the same as Ni, in the forward bias, a minor decrease of J as T decreases is observed, while in the reverse bias, J increases as T reduces totally. No transition stage is observed in the lower reverse bias. Hence there is a negative current-temperature coefficient at reverse bias and a positive current-temperature coefficient at forward bias.

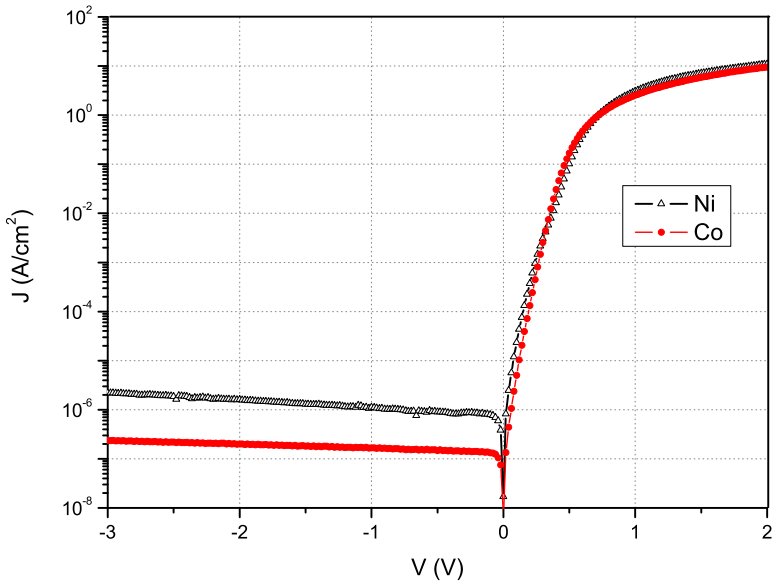

Figure 3.21: Comparison between room temperature J-V characteristics of electrodeposited Ni-Si and Co-Si Schottky barriers. The doped Si resistivity is $1\sim2\ \Omega \cdot cm$. The cross section of all contacts was 400μm diameter.

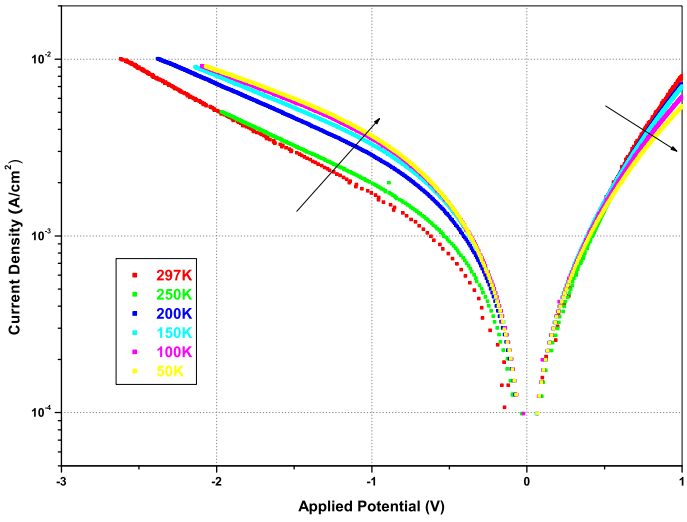

Figure 3.22: Low temperature J - V characteristics of an electrodeposited Co-Si contact for highly doped Si. The contact had a diameter of 1.5 mm.

Contact Name	Method	Pulse Pretreatment	Deposition condition	J_s (A/cm^2)	Φ_{Bn} (V)	η	R (Ω)
Ni 1-2 Ω·cm	Potentiometry	-1.7V, 0.4sec	-1.1V	1.57×10^{-6}	0.76	1.42	100
Co 1-2 Ω·cm	Amperometry	-10mA, 0.4sec	-4.5mA	2.00×10^{-7}	0.82	1.12	114

Table 3.6: The Parameters of Ni/Co-Si Schottky Barriers' J-V Characteristics. The doped Si resistivity is 1$\sim$2 $\Omega \cdot cm$. The cross section of contacts was 400μm diameter.

Contact Name	Side (cm)	Area (cm^2)	I_S (A)	J_s (A/cm^2)	Φ_{Bn} (V)	η	R (Ω)
A5-B	0.15	2.25×10^{-2}	4.33×10^{-5}	1.92×10^{-3}	0.58	1.39	38.72
A5-D	0.10	1.00×10^{-2}	1.58×10^{-5}	1.58×10^{-3}	0.58	1.26	43.48
A5-F	0.07	4.90×10^{-3}	6.64×10^{-6}	1.35×10^{-3}	0.59	1.18	47.96

Table 3.7: The Parameters of Schottky Barriers' I-V Characteristics. Contacts A5-B,D,F are made on the medium resistivity (1-2 Ω-cm) silicon wafer by nickel evaporation. These parameters are calculated from I-V measurements.

3.5.3 Evaporated ferromagnet-Si Schottky Barriers

To compare between electrodeposition samples and evaporation ones, the I-V curves of evaporation samples are modified by eliminating the effect from series resistance. The former I-V relation is

$$I = I_S \cdot e^{(V - I \cdot R_S) \cdot \frac{q}{\eta k T}} \tag{3.25}$$

The modified I-V relation is

$$I \cdot e^{IR_S) \cdot \frac{q}{\eta k T}} = I_S \cdot e^{V \cdot \frac{q}{\eta k T}} \tag{3.26}$$

Fig. 3.23 shows the original I-V curves from measurement and the modified I-V curves from modeling. It is clear that elimination of the effect from series resistance can improve the ideality factors of I-V characteristics.

Compared with table 3.1 and 3.7, it indicates evaporation samples lose some rectifying characteristics due to the decreasing saturation current density (about 10^-5 A/cm^2), decreasing barrier heights (about 0.60 V) and increasing ideality factors (about 1.20).

The reverse currents of Co-Si and Ni-Si both increase approximately 100 times from electroposition samples to evaporation samples, as shown in Fig. 3.24.

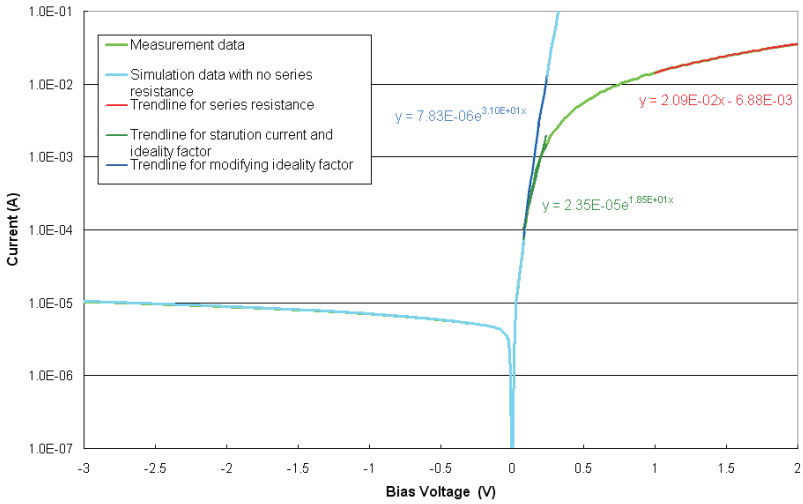

Figure 3.23: I-V Characteristics of Schottky Barriers made on the medium resistivity (1-2 Ω-cm) silicon wafer by nickel evaporation. The curves are from I-V measurements at room temperature.

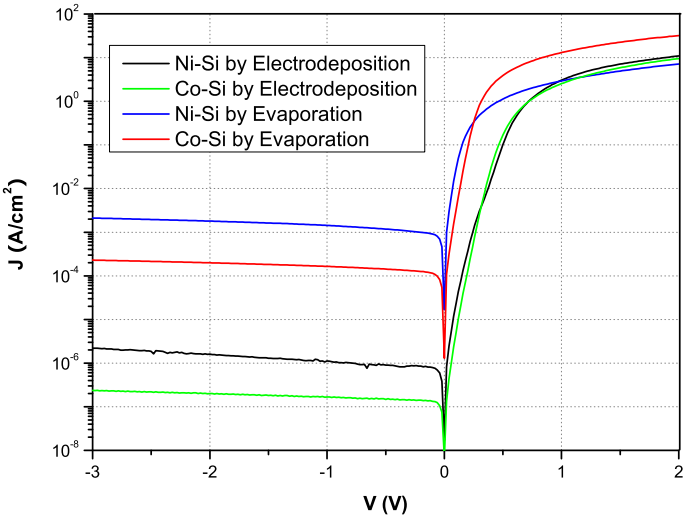

Figure 3.24: Comparison between I-V Characteristics of Schottky Barriers fabricated by Electrodeposition and Evaporation. These SBs are made on a 1-2 Ω-cm silicon wafer by Ni and Co. The contact had a diameter of 0.7 mm.The curves are from I-V measurements at room temperature.

3.6 Conclusions

The principle of Schottky barriers in the beginning of this chapter outlines the fundamental electrical characteristics of metal-semiconductor contact. The experimental results, which includes I-V characteristics of Ni-Si Schottky barriers, C-V characteristics of Ni-Si Schottky barriers and thermionic and thermionic field emission at Ni-Si Schottky barriers, presented and discussed in this chapter reveal that electrodeposited Ni-Si Schottky barriers have excellent rectifying characteristics. For further application in Spintronic devices, three other fabrication methods of Schottky barrier on Si are developed. Firstly, Ni is electrodeposited on Si with a magnetic field to improve uniaxial magnetic anisotropy. No clear progress is achieved. Secondly, Co is electrodeposited on Si to realize the independent magnetic switchings in the future Spintronics device. Electrodeposited Co-Si Schottky barriers have better rectifying characteristics than Ni-Si SBs, though these properties are harder to reproduce. Thirdly, due to the weak conductivity of the vertical spin valves, introduced in the next chapter, evaporated Ni-Si, Co-Si Schottky barriers are investigated. Though there is some loss of rectification, these two types of SBs are still promising in vertical spin valve structures.

Chapter 4

Towards Si and Ge Spin Valves and Transistors

4.1 Introduction

Spintronics or magneto-electronics is the area of research in which magnetic fields influence the electrical properties of a circuit. In this new discipline, one of the key challenges is spin injection from a magnetic metal into a semiconductor, which requires spin conservation during the transport of electrons. It is particularly interesting because it allows the integration of magnetic devices with microelectronics. The conductivity mismatch problem has been shown to prevent ohmic contacts from being used for spin injection [39]. Instead, Schottky barriers and Ferromagnet/Insulator/Semiconductor contacts have been proposed. Though the forward bias current caused by thermionic emission over a Schottky barrier is concluded to be unsuitable for spin injection and detection, because the electron transmission occurs at energies well above the Fermi level, while the reverse bias tunnelling currents could potentially be used for spin injection and detection [40]. The step toward both lateral and vertical spin valves are reported in this chapter, but due to the fire that destroyed the entire clean room, it has not been possible to progress as far on this subject as was hoped.

4.2 Spintronics

4.2.1 Magnetoresistance

In spintronics, the unique concept relating electronics and magnetism is magnetoresistance, the change in resistance of a material upon application of a magnetic field. The direct effect, called Lorentz magnetoresistance is related to the Lorentz force and is generally not considered as part of spintronics. However, various effects exist which relate the magnetic orientation of a material to its resistance, such as anisotropic magnetoresistance (AMR)[41], giant magnetoresistance (GMR)[42, 43], the large magnetoresistance in ferromagnetic thin film tunnel junctions (TMR)[44] and the domain wall magnetoresistance (DW-MR)[45]. These four types of magnetoresistances suggest semiconductor spintronics could flourish in two main orientations: passive integration (in which the semiconductor has only charge related functionality) and active integration (in which spin effects in the semiconductor are explored). The main passive integration application is MRAM. In active integration applications, several new types of spin transistors are being investigated, such as the Johnson transistor, the spin-valve transistor (SVT, hot electron transistor or Monsma transistor)[4], the magnetic tunneling transistor (MTT)[46], the Spin FET (Datta-Das transistor)[47] and the SPICE transistor. In addition, various magnetic semiconductors such as diluted magnetic semiconductors (DMS) are also studied, but this falls outside the scope of this thesis.

The magnetoresistance is the property of some materials to lose or gain electrical resistance when an external magnetic field is applied to them [48]. This is expressed as

$$MR = \frac{R_M - R_0}{R_0} \tag{4.1}$$

where R_M is the resistance with the applied magnetic field and R_0 is the resistance without an applied magnetic field.

Anisotropic Magnetoresistance (AMR) was first discovered by William Thomson (Lord Kelvin) in 1857. Anisotropic magnetoresistance (AMR) can be considered as a material property leading to an increase of electrical resistance when a magnetic field is applied parallel to the current. As a result of bulk scattering of conduction electrons by spin-orbit coupling, the AMR decreases with the thickness of the

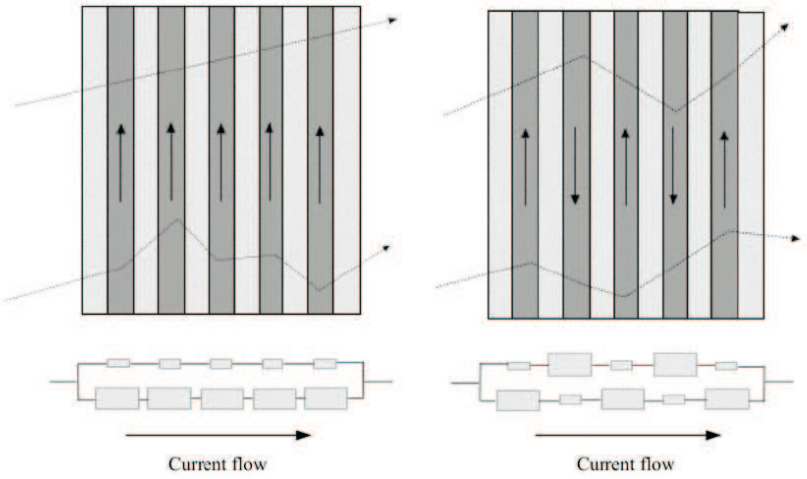

Figure 4.1: Simplified illustration of GMR effect using layout and 'resistor model' [49].

ferromagnetic film. The expression for AMR is

$$\rho = \rho_{\perp} + \triangle\rho\cos^2\theta \tag{4.2}$$

where $\Delta\rho$=$\rho_{\parallel}$-$\rho_{\perp}$;θ is the angle between the vectors of magnetization M and current. The maximum value of AMR which has been achieved is about 7% using nickel, iron or cobalt alloys at room temperature [41].

Giant Magnetoresistance (GMR) was observed independently by Fert and Grunberg *et al.* [42, 43] in 1988, and these two scientists have recently been awarded the Nobel Prize for Physics for this discovery. GMR takes place in a structure of a thin layer of paramagnetic(PM) material sandwiched between two ferromagnetic(FM) electrodes, with the parallel magnetic moment configuration corresponding to a low electrical resistance while the antiparallel state causes a high resistance as illustrated in Fig. 4.1 [49]. In the 'resistor model', the two parallel paths represent the respective spin channels and the resistors in each path represent the resistances which they experience in each of the layers. So it is easy to understand that the resistance of antiparallel state is much higher than that of parallel state. Compared with the anisotropic magnetoresistance, the giant magnetoresistance is much higher and values up to 40% can be reached.

Tunneling Magnetoresistance (TMR) was discovered by Julliere *et al.* in 1975, but large values of TMR were only achieved in 1995 by Moodera *et al.* in 1995

[44]. TMR is found in the structure of a thin insulator separated by two ferromagnets (FM/I/FM). The spin-polarized tunneling current depends on the relative orientation of magnetization M of the ferromagnetic electrodes. Magnetic-tunnel junctions (MTJ) are two-terminal spintronic devices whose magnetic resistance change is represented as TMR. To obtain a reasonable current, the thickness of tunnel barrier must be of the order of a nanometer and the quality of it is also very important. At present, the maximum TMR values that have been achieved are about 220% at room temperature and approx 300% at low temperatures with highly oriented (100) MgO tunnel barriers and CoFe electrodes [50].

Domain wall magnetoresistance (DW-MR) is a new type of magnetoresistance effect, discovered around 1996, which is caused by spin dependent electron scattering at the domain walls in a homogeneous magnetic system. The applied magnetic field moves the domain walls causing the resistance of the system to change. As Fig. 4.2 shown, the magnetic geometry of the ferromagnetic domain wall is similar to that of the GMR case. The presence of a domain wall corresponds to antiferromagnetically aligned layers. The absence of domain walls corresponds to ferromagnetically aligned layers [45, 51].

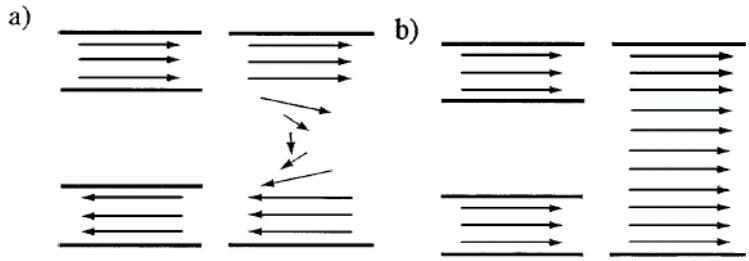

Figure 4.2: Schematic illustration of the similarity between the magnetic geometry of a GMR trilayer and a ferromagnetic domain wall. (a) The relationship between an antiferromagnetically aligned trilayer and the presence of a domain wall. (b) The trilayer in its ferromagnetically aligned state, which corresponds to the absence of the domain wall in the ferromagnet [52].

4.2.2 Spin Injection

The essential requirement for realizing a spin transistor is the injection of a spin polarized current from a ferromagnetic material into a semiconductor[39, 53]. Al-

though spin injection is the key of the future development of spintronics, the process is not very straightforward. The main obstacle is the conductivity mismatch problem for electrical spin injection from a ferromagnet to a semiconductor ohmic contacts. The spin dependent resistance of a length of ferromagnet equal to its spin flip length is very much lower than the spin independent resistance of the semiconductor up to its spin diffusion length. Once the spin polarized current is injected at the interface between ferromagnet and semiconductor, the spin-up and spin-down currents lose their polarization due to the same resistance. Therefore, if a certain current polarization survives in the semiconductor, it requires a potential difference between the two spin channels, which causes different current densities (of the order of μA) in the channels. However, in order to obtain the same potential difference at the interface as in the metal, a very high current density (of the order of mA) in the ferromagnet is required. Taking current conservation into account this cannot happen since the same currents flow through both ferromagnet and semiconductor[54].

The idea to solve the conductivity mismatch problem is to insert a resistance in one of the spin channels of the ferromagnet-semiconductor, whose value equals the difference in resistance between spin-up and spin-down channels. This resistance makes up the required potential difference at the interface between the two channels, resulting in the match of the potentials for both sides. Nowadays, there are three main practical methods to solve the conductivity mismatch problem: dilute magnetic semiconductors, tunnel contacts (ferromagnet-insulator-semiconductor) and Schottky contacts (ferromagnet-semiconductor). In this work, Schottky contacts were used to realize spin injection from ferromagnet to silicon directly. When the barriers are applied in reverse bias, the current transport is dominated by thermionic field emission. The carriers tunnel through the barriers near the Fermi energy and the density of states in the ferromagnet leads to a possibility of spin dependent tunneling. Bratkovsky *et al.* [55] showed theoretically that spin injection would be significantly enhanced by increasing the doping level of the semiconductor. The higher doped semiconductor interface results in a thinner depletion region, increasing the current at the fermi-level.

4.2.3 Spin Transistors

As a potentially important application of active (semiconductor) spintronics, various spin transistors are developed. Depending on the applied materials, spin transistors can be divided into all metal transistors such as the Johnson transistor, and hybrid spin transistors such as the Monsma transistor. Depending on the working principles, spin transistors can be divided into spin bipolar transistors such as magnetic tunneling transistors, and spin field-effect transistors such as the Datta-Das transistor. The following section will describe specific transistors in detail.

Datta-Das Transistor In 1990, Datta and Das [47] first proposed a spin transistor concept, a so called Spin FET (Datta-Das Transistor). The construction is very similar to that of a conventional FET, except that the source and drain electrodes of the spin FET are made from FM metals. The semiconductor channel is subject to a transverse electric field whose magnitude may be tuned by applying a gate voltage. Through spin-orbit coupling this electric field gives rise to an effective magnetic field (Rashba effect) around which the carriers precess. The Spin FET is expected to behave like a normal FET with the additional feature that the differential magnetization of its electrodes (and hence its electrical characteristics) are sensitive to an externally applied magnetic field. The principle of this feature is described as spin-polarized carriers leaving the source with their spins parallel to the source magnetization and precess in transit through the channel. If the drain magnetization is parallel to that of the source and the carriers perform an integral number N of precessions in transit, then the device conductance is high. However, slight modification to the gate voltage changes the precession rate and if the spins now execute N + $\frac{1}{2}$ precessions in transit, the device conductance is minimized. Although the spin FET is a model and not a realized device at present, much groundwork has already been done. Besides the low voltage and low power supply, the switching speed of a spin FET is very fast because it has no minority carriers and hence no charging effects[49].

Johnson Transistor is a three-terminal GMR device created by Johnson in 1993 [56, 57, 58]. This spin transistor is the natural progression from the two-terminal GMR device by placing a third contact attached to the intermediate PM base layer as shown in Fig. 4.3. When a current is pumped around the emitter-base circuit to cause a spin accumulation in the base layer, the collector is floated and monitors the

potential. The floating potential of the collector depends on whether its magnetic moment is parallel or anti-parallel to the magnetization of the polarizing emitter electrode which causes the spin accumulation. The collector is sampling the electrochemical potential of the appropriate spin type in the base. Though the electrical characteristics of this purely Ohmic device are magnetically tuneable, its operation only generates a very small voltage output change and no power gain due to its all-metal construction [59].

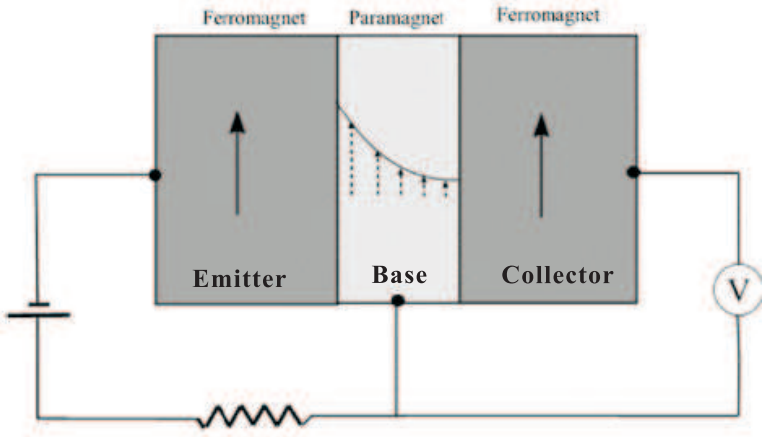

Figure 4.3: Schematic diagram of Johnson transistor [49].

The spin-polarized-injection current emitter (SPICE) transistor [49] is a spin bipolar transistor. The fundamental block of the SPICE transistor is made up of a spin-polarized injection current emitter, a semiconductor base in which a non-equilibrium spin-polarized carrier distribution is established, and a spin-dependent collector assembly as shown in Fig. 4.4(a). In the SPICE design the non-equilibrium status of the base manifests itself as an excess carrier density and also in the form of a spin accumulation. A good choice of spin-dependent collector assembly to harvest the non-equilibrium spins in the base is essential to provide a large power gain with high magnetic sensitivity and minimize the admittance between base and collector. A good quality of collector for the SPICE design is an inverted tunnel spin injector, which is heavily back biased so as to collect the non-equilibrium base carriers. Fig. 4.4 shows the cross section of the SPICE transistor fabricated by Gregg *et al.* in Southampton [49]. The current gain is considerably larger than for the SVT, but still only 1.02. Therefore the design of the SPICE transistor should be improved further.

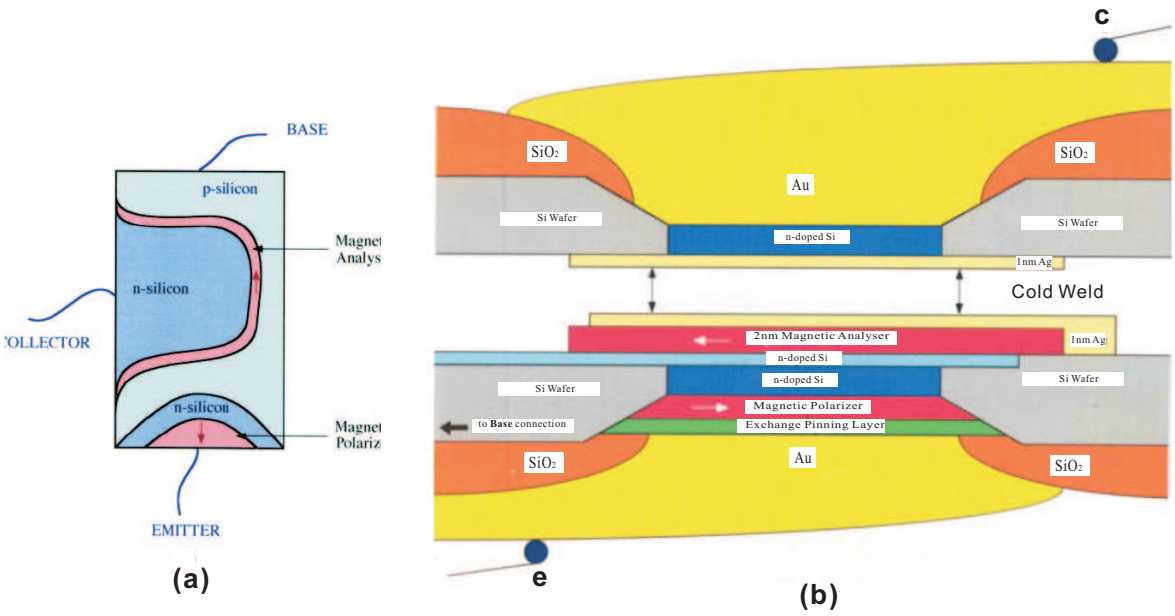

Figure 4.4: SPICE transistor.(a) The simulation schematic diagram. (b) The practical realization, fabricated at the University of Southampton [49].

Spin Valve Transistor is a FM-PM-FM structure, which is also called the Monsma Transistor, or hot electron transistor, as discovered in 1995 [4]. Unique to this transistor, the spin-valve transistor depends on hot electrons to transmit charges. The reason that the negative charge carriers are called hot electrons is the fact that they are not Fermi electrons but electrons with excess energy. The spin-dependent transport consists of these non-equilibrium electrons. It should be noticed that a remarkable characteristic of SVT is that the magnetic state of the base controls the current of the collector through spin-dependent scattering [60].

The spin-valve transistor, a three-terminal device, similar to a bipolar junction transistor (BJT), has an emitter-base-collector frame. As fig. 4.5. shows, the emitter and the collector are made from semiconductor materials, but the particular base is metallic and consists of spin-valve multilayers. This leads the hot electrons to transport perpendicularly in ultra short time with a low base resistance. Such multilayers should be made up of magnetic layers and a normal metal layer, and different type layers should be interleaved. At the rear of the emitter and the collector, ohmic contacts are deposited.

To understand the feature of spin-valve transistors, the concept of magnetocurrent

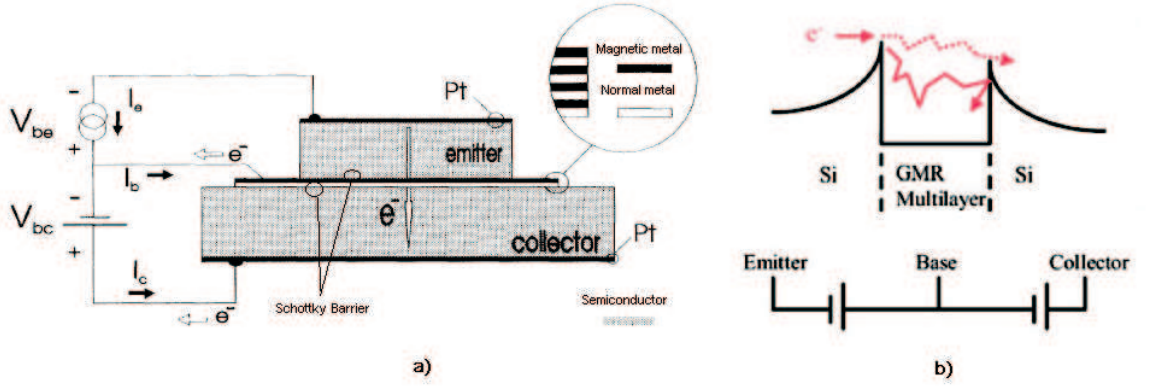

Figure 4.5: The spin-valve transistor: a) Schematic cross section [4]. b) Energy diagrams [49].

(MC) is introduced. This is defined as the change in collector current normalized to the minimum value:

$$MC = \frac{I_C^P - I_C^{AP}}{I_C^{AP}} \tag{4.3}$$

where P and AP refer to the parallel and anti-parallel magnetic state of the base spin valve, respectively. From the first spin-valve transistor to the most recent device, the magnetocurrent changed from 215% in 500 Oe applied magnetic field to 400% in a few Oe magnetic field [4, 61, 62]. However, the in-plane magnetoresistance was only 3%. These measurements have been done at 77 K, but good room temperature operations exist as well. The biggest disadvantage of the SVT is the very low output current and gain.

Monsma *et al.* used a direct bonding technique to build up Schottky barriers and adhere spontaneously the multilayers. As Figure 4.6 shows, in ultrahigh vacuum cavity, the emitter and collector are alternated to sputter with the partial layers of the base while the other one is prevented by a shutter. Later a metal-metal bond connects the base. Obviously, the quality, strength, reliability and topography of this metal bond decide the base's material selection. Gold and titanium gives the best metal bonds[63, 64, 65].

Magnetic tunneling transistor (MTT) is derived from the spin-valve transistor and also referred to as a tunnel SVT. In 1997, the first MTT was fabricated by Mizushima *et al.* [46, 66]. There are two different variations of MTTs. One type has

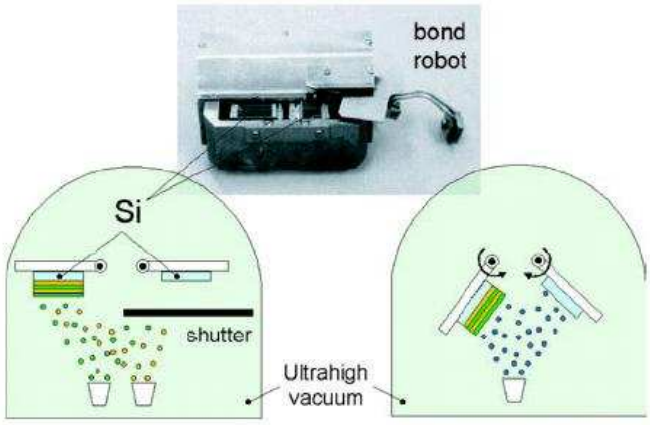

Figure 4.6: Concept of vacuum metal bonding, in which two Si wafers are joined together using freshly evaporated metal as a bond [63].

a thin insulating layer to separate the metal base from a non-magnetic metal emitter electrode. When a voltage is applied across the tunnel barrier between emitter, unpolarized electrons are injected by tunneling into the metal base. The other type has not only a tunnel barrier but also a magnetic emitter electrode. So the injected hot electrons are spin polarized as they enter the base. Fig. 4.7 shows the energy diagrams of these two variations of MTTs.

Although the emitter part is the only difference between MTTs and SVTs, these two types of transistors still have some different properties:

- SVT requires a vacuum metal bonding while MTT's emitter and base can be deposited onto the semiconductor collector in vacuum directly.
- In MTT, the energy of the injected hot electrons is given by the voltage across the tunnel barrier while in SVT, the hot electrons are across the Schottky barrier.
- MTT with a ferromagnetic emitter has only a single magnetic layer in the base, as opposed to a multilayer magnetic metal and no magnetic spacer for SVT.

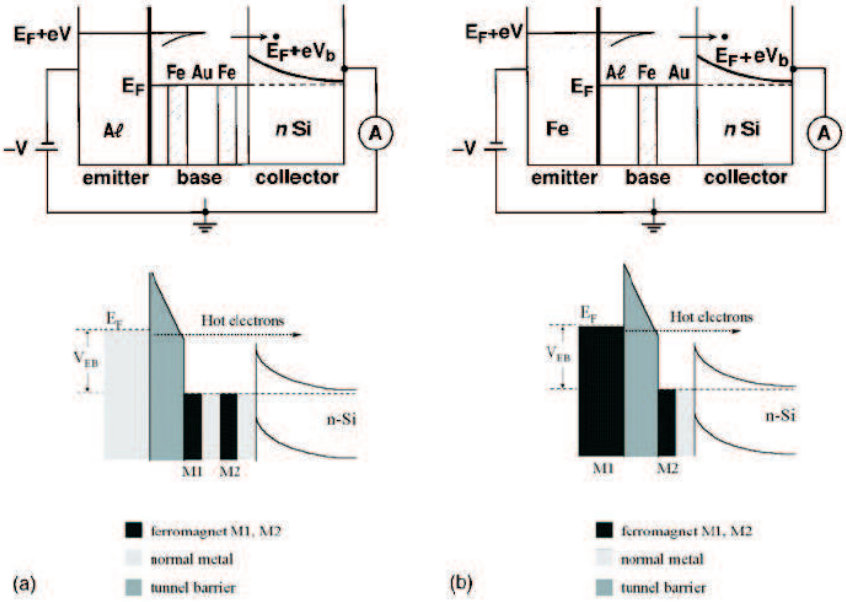

Figure 4.7: Energy diagrams of the MTT with (a) a non-magnetic tunnel injector and (b) a ferromagnetic tunnel injector to generate the hot-electron current. eVb is the Schottky barrier height [66, 63].

4.2.4 Recent Progress in Spin Injection and Detection experiments

Recently, Lou et al.[67] achieved electrical detection of spin transport in lateral ferromagnet-GaAs< 011 > devices and Berend et al. [68, 69] succeeded to demonstrate electrical spin-injection into silicon. These two groups both used a ferromagnet tunnel barrier contact to solve the conductivity mismatch problem. However, these lateral spin transport structures based on Si adopted a nonlocal detection technique, which benefits from excluding any spurious contributions from anisotropic magnetoresistance or local Hall effects on spin currents. However, electrical spin injection and detection in semiconductors for practical applications needs to take place locally. This requires additional stringent conditions such as large tunnel spin polarization (for a tunneling contact) and a proper resistance-area (RA) product[70].

Besides tunneling contacts, some researchers suggested Schottky contacts used as spin filters may be another solution. Bratkovsky et al. [55] had shown by a theoretical model that spin injection could be remarkably increased by introducing a highly doped layer between a ferromagnet and a semiconductor. When the barrier

is biased in the reverse direction and the transport is dominated by field emission, the carriers tunnel through the barrier at the Fermi energy. The density of states in the ferromagnet leads to a spin dependent tunneling probability. The use of a thin, highly doped surface region in the Schottky barrier, which reduces the depletion width as well as the effective barrier height, is supposed to enhance the probability for tunneling.

4.3 Experimental Results of Vertical Spin Valves

A vertical spin transport structure of Ni/Si/Co junctions was investigated as illustrated in Fig. 4.8. It uses Co/Si and Ni/Si Schottky contacts as the spin injection and detection electrodes. The structure also benefits from increased control over vertical scaleability of Si enhancing the potential spin transfer between the two electrodes. This structure was fabricated on Si membranes using a combination of standard lithography, oxidation, implant and KOH anisotropic etching, at the National Microelectronics Research Centre (NMRC), Cork. As discussed in Chapter 3, the rectifying behaviour of SBs fabricated by electrodeposition is better than which fabricated by evaporation. However, a smooth and continuous metal film electrodeposited on semiconductor needs to enough high conductivity of substrate. In the Si membrane structure, only the membrane areas are high doped. So that due to the lack of conductivity of Si substrate, the Ni film by electrodeposition was not a continuous film, as shown in Fig. 4.9(a). A smooth and continuous metal film by evaporation (An example is shown in Fig. 4.9(b).) had to replace it. Finally, metallization of 87 nm Ni and 50 nm Co was performed by e-beam evaporation. The nominal thickness of the membrane is 250 nm and the active Si membrane is separated from the Si handle layer by 400 nm of SiO_2.

Typical J-V characteristics of the Ni/Si/Co device measured at 300K for various Si doping density (Nd) were presented in fig. 4.10. At positive biases, J is dominated by the reverse bias current of the Co/Si junction, whereas, at negative biases, J is limited by the reverse current of the Ni/Si junction. J increases with increasing bias voltages, which is attributed to the contribution from the thermionic field emission in the respective Schottky junctions. This was confirmed by fitting the experimental

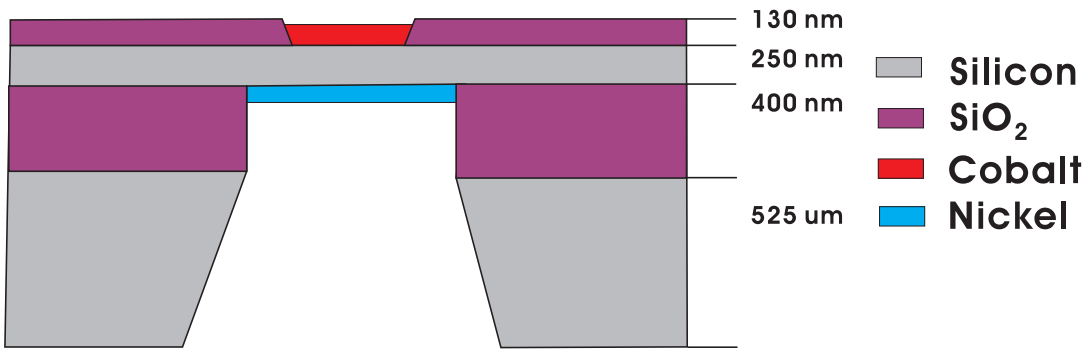

Figure 4.8: Si spin injection and detection device utilizing tunneling through electrodeposited Ni-Si contacts. The two ferromagnetic layers are asymmetrically designed to switch under different external magnetic fields.

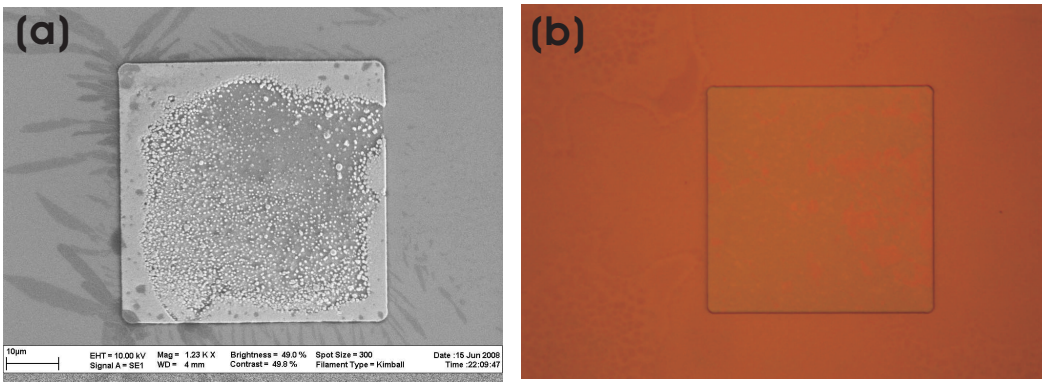

Figure 4.9: Micrographs of metal thin films on Si membranes. (a) 200nm Ni film by electrodeposition, taken by SEM microscope. (b) 50 nm Co film by evaporation, taken by Optical microscope.

curves with the theoretical curves obtained by numerical simulation tool Sentaurus Device. This uses nonlocal tunnelling models for electrons. Here Ni/Si and Co/Si Schottky barrier heights of 0.70 eV and 0.64 eV have been used.

Magnetoresistance (MR) measurements were performed on the devices using a sense current corresponding to the respective device currents at ±0.2 V. However no MR signal was observed for any of the devices. Fig. 4.11 shows a typical MR measurement results. Applied 1 nA current to the 20μm×20μm square junction with Ni(87nm)/Si(250nm)/Co(50nm) structure, where silicon doping density is 4×10^{19}cm^{-3}, the magnetic field was scanned from 500 mT to -500 mT with 10 mT step, then did a reverse scan as well. There are some jumps in the curves. However, these jumps are not reproducible. The reasonable understanding of these jumps is that it was caused by the current drift during the measurements. The reason why no MR signal was detected could be the lack of a differential switching behavior of the two FMs, which could not be readily verified in this experiment. More importantly, the RA products at ±0.2V obtained for all three Si doping densities are much higher than that required for a spin injection- extraction condition exhibiting a high MR (Fig. 4.12). However, our experiments show that an electrically well functioning back to back diode can be fabricated using the membrane technique and further experiments can build upon these results. In particular, one way of adjusting the RA product is the growth of a very thin highly n- doped (δ) Ge between the FM and n-Si that would increase the electron tunnelling transparency at the injection and extraction interfaces[55]. By numerical simulations we find that by incorporating a 2 nm Ge layer of 1×10^{20}cm^{-3} doping density at the Ni/Si and Co/Si interfaces, the RA values at ±0.2V decrease to the theoretical range for high MR as shown in Fig. 4.12.

4.4 Experimental Results of Lateral Spin Valves

4.4.1 Introduction

As discussed before, a lateral spin valve and spin transistor are virtually identical in structure to a Schottky Barrier MOSFET. In this section, we investigate Ni-Ge and NiGe-Ge contacts for Schottky barrier MOSFET's and hence for SB in Transistors as well. Ge channel MOSFETs are considered as promising devices for future high-

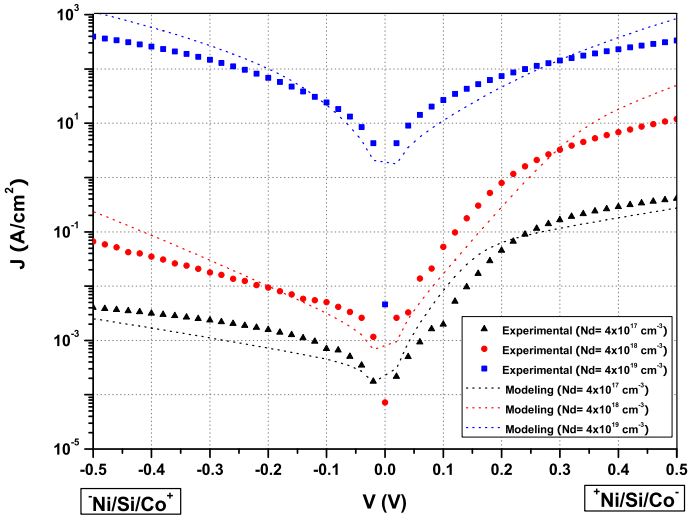

Figure 4.10: J-V characteristics (symbols) of the fabricated Ni-Si-Co spin injection-extraction device for various doping densities. The dot lines refer to the J-V curves modelled by the Sentaurus Device simulator tool. The modelling was done by Muhammad Husain.

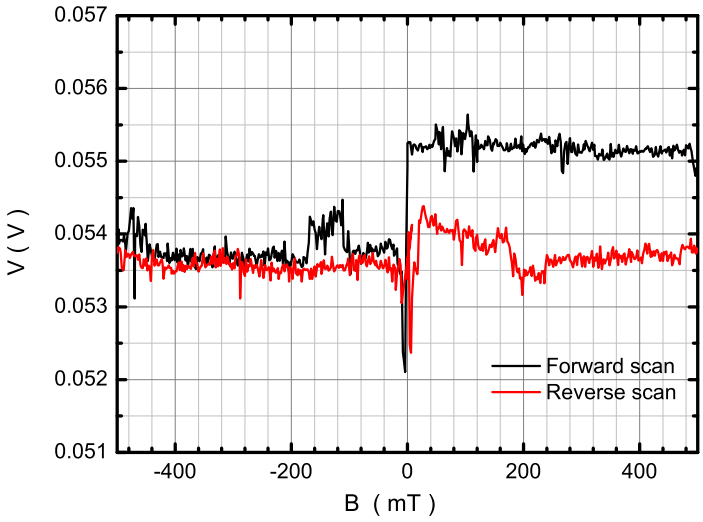

Figure 4.11: Magnetoresistance measurements of $20\mu m \times 20\mu m$ square junction with Ni(87nm)/Si(250nm)/Co(50nm) structure. The silicon doping density is $4\times10^{19}cm^{-3}$. The magnetic field is scanned from 500 mT to -500 mT with 10 mT step. The applied current is 1 nA.

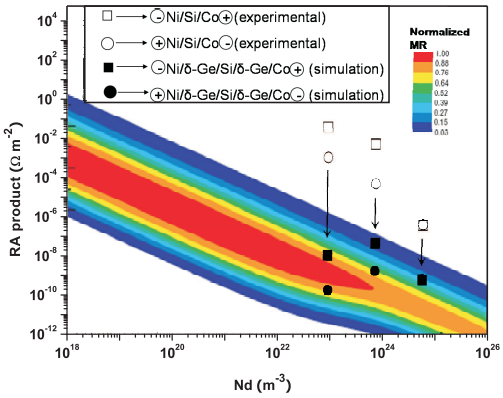

Figure 4.12: RA products of the fabricated Ni-Si-Co device and the simulated Ni/δ-Ge/Si/δ-Ge/Co device as a function of Si doping density for applied biases of $\pm$ 0.2 V. The calculated MR of a Si spin transistor as a function of the contact RA and Si doping is adopted from ref.[71], where the colour legend shows the value of normalized MR.

speed CMOS technology as they offer high carrier mobilities suitable for a large drive current. Schottky barrier (SB) source/drain MOSFETs overcome the problems faced by the conventional transistor scaling caused by the stringent conditions required for doping with low series resistance [72, 73]. The Ge based SB p-MOSFETs, however, suffer from increased leakage currents due to its narrow bandgap and low Schottky barrier height [74]. In this work, we show that electrodeposited Ni-Ge and NiGe-Ge Schottky diodes on highly doped Ge exhibit near ideal Schottky barrier behavior with low off current.

4.4.2 Schottky barrier characteristics

Fig. 4.13 shows J-V characteristics of electrodeposited Ni-Ge SBs for the three different resistivity Ge substrates (ρ1=2-2.4 Ω-cm, ρ2=0.13-0.15 Ω-cm and ρ3=0.005-0.02 Ω-cm) and of nominal 10 μm square contact area.

A high-quality rectifying behaviour is observed for the SBs. For the highly resistive (ρ1) Ge, excellent SBs are achieved with very low reverse bias current, being 5 orders of magnitude smaller than the forward bias current at 1V bias. Tunnelling effects of

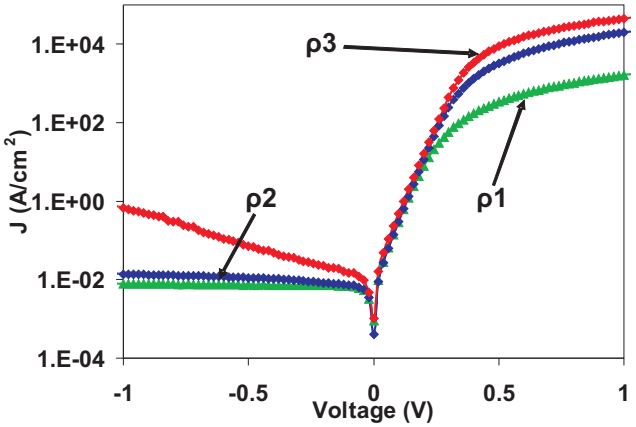

Figure 4.13: J-V characteristics of the Ni/Ge Schottky diodes (10 μm square contact) as a function of Ge resistivities (ρ1=2-2.4 Ω-cm, ρ2=0.13-0.15 Ω-cm and ρ3=0.005-0.02 Ω-cm).

this SB are negligible in the reverse bias. SBs on the medium resistive (ρ2) Ge showed similar rectifying behaviour with a little tunneling current in the reverse bias. Only on the low resistive substrate (ρ3), Ni/Ge SB showed increased tunnelling effects in the reverse bias. However, even these Ni/Ge diodes on lowly resistive Ge showed excellent rectifying behavior with the reverse bias current of the diodes. The current on the the low resistive substrate (ρ3) substrate was still 5 orders of magnitude smaller than the forward bias current. All currents can be explained by standard thermionic emission, and additionally, by thermionic field emission theory for the reverse bias. This is a significant improvement over similar work done in literature [75] where Schottky diodes grown by evaporation technique exhibited rectification of only 2-3 orders of magnitute even on highly resistive Ge substrates. Breakdown of the diodes was not observed up to -3V bias indicating that edge effects are suppressed as explained in our previous work [31].

Same as the extrapolation method mentioned in section 3.2.2, from the J-V curves in Fig. 4.13 the Ni/Ge Schottky electron barrier height (ϕ_n), ideality factor (η) and series resistance (R_s) can be extracted assuming the thermionic emission model in the forward bias[76]. The calculated Schottky barrier parameters are presented in Table 4.1 for all types of substrates. For these calculations Richardson constant (A^*) of 50 A cm^{-2} K^{-2} was used[77]. It is seen from Table 4.1 that the Schottky barrier heights are virtually constant for the Ge substrates of various resistivities. The low

Table 4.1: Comparison of the parameters extracted from J-V and C-V characteristics of the Ni/Ge Schottky diodes.

Resistivity Label	$\rho 1$	$\rho 2$	$\rho 3$
η	1.12	1.04	1.09
R_s (Ω)	30.77	16.05	11.72
ϕ_n(V) (from J-V)	0.52	0.53	0.52
ϕ_n(V) (from C-V)	0.56	0.53	0.53
N_d(cm^{-3})	8.7x10^{14}	1.45x10^{16}	2.9x10^{17}
Resistivity (Ω-cm) (nominal)	2-2.4	0.13-0.15	0.005-0.02
Resistivity (Ω-cm) (from C-V)	1.84	0.11	0.006

ideality factors indicate thermionic emission to be the dominant current conduction mechanism in the forward bias for the SBs on different substrates.

C-V measurements of SBs on Ge were performed for A*-independent measurement of the SB height. C-V characteristics for SBs on Ge substrates of various resistivity, having a contact area of 400 μm^2 square, are shown in Fig. 4.14. Same as the extrapolation method mentioned in section 3.2.3, a straight line is observed, and from its intercept on the voltage axis the SB height (ϕ_n) is calculated. Furthermore, from the slope of this characteristic, the Ge doping concentration (N_d) can be determined. For example a value of 2.9×10^{17} cm^{-3} for N_d is obtained corresponding to a resistivity of 0.006 Ω-cm, which matches the specification of the Ge substrate. Similar C-V measurements were performed on SBs on the medium (0.13-0.15 Ω-cm) and highly (2-2.4 Ω-cm) resistive Ge and barrier heights (ϕ_n) of 0.53 V and 0.56 V and substrate doping densities of 1.45×10^{16} cm^{-3} and 8.7×10^{14} cm^{-3} were obtained, respectively. The barrier heights obtained are in good agreement with those obtained from the I-V measurements as observed in Table 4.1.

The electrodeposited Ni films on Ge (0.005-0.02 Ω-cm) were annealed for 20 minutes at temperatures ranging from 300°C to 500°C to investigate their Germanidation mechanism. Phase identification and crystallographic structure determination were carried out using XRD with Cu Kα radiation (λ = 1.5418 $\mathring{A}$) in a θ-2θ geometry. Fig. 4.15 shows the XRD spectra for as-deposited and annealed Ni/Ge samples for initial Ni thicknesses of 70 nm. The initial Ni (111) peak at 44.68° completely dis-

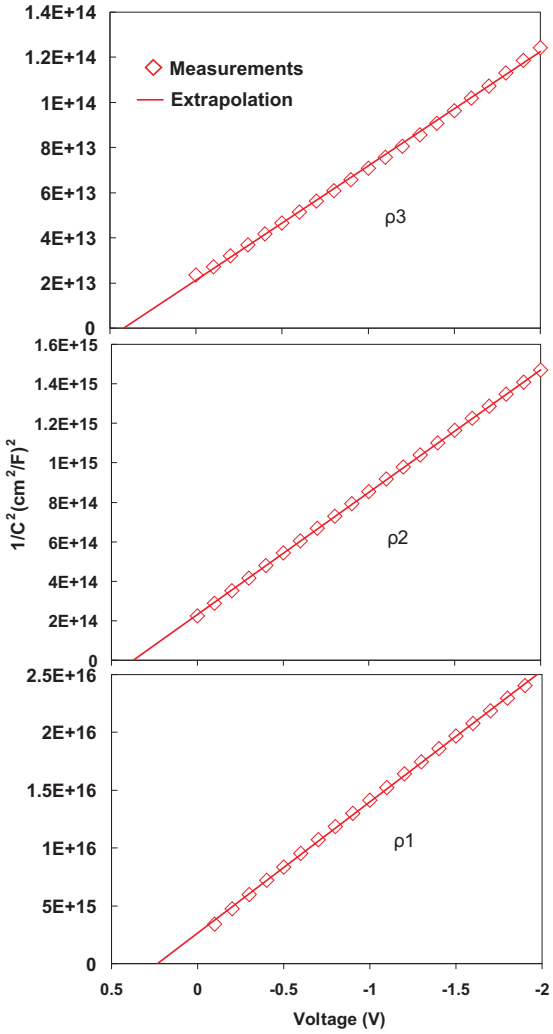

Figure 4.14: C^{-2}-V curve of an electrodeposited Ni-Ge contact (400 μm square) for various substrate resistivities (ρ1=2-2.4 Ω-cm, ρ2=0.13-0.15 Ω-cm and ρ3=0.005-0.02 Ω-cm).

appears after annealing indicating complete reaction of the Ni film with Ge. Peaks at 34.8°, 35.2°, 44.2°, 45.7°, 53.8° and 54.4° are observed when the sample was annealed at 500°C. These peaks are in excellent agreement with the θ-2θ pattern of the NiGe JCPDS standard. The peaks were identified as NiGe(111), (210), (211), (121), (002) and (301), respectively. No peaks corresponding to other Ni-Germanides, e.g., Ni_2Ge $NiGe_2$, etc. are observed. This clearly shows only polycrystalline Ni-mono-Germanide (NiGe) phase forms at the annealing temperatures. The lattice constants of the formed NiGe are determined to be a = 5.81 $\AA$, b = 5.37 $\AA$, and c = 3.40 $\AA$ from the XRD spectra, in agreement with the reported values[78, 79].

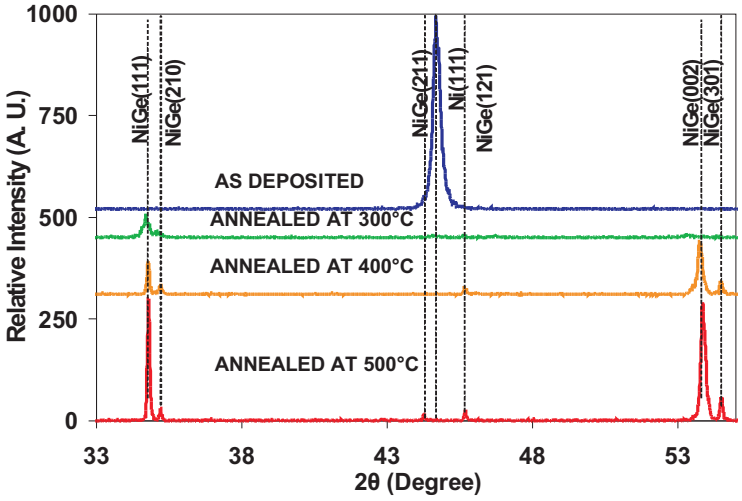

Figure 4.15: The XRD spectra for the as-deposited and annealed Ni/Ge samples showing transformation from Ni to NiGe. The annealing was done by Muhammad Husain. The XRD measurements were done by Dr. Kees de Groot and Muhammad Husain.

For the 300 °C annealed samples the NiGe peaks are very weak, while after 400 °C annealing, the peaks become quite strong. The crystallite size (t) of the grown NiGe(111) was investigated by taking further XRD scan within close intervals surrounding the peak. These are shown in Fig. 4.16 as a function of annealing temperature (T). The crystallite sizes are calculated from the peaks using the Scherrer relation:

$$t = \frac{0.9\lambda}{d\,\cos\theta}, \tag{4.4}$$

where d is the broadening of the peaks due to the crystallite size. It was observed that t increases with increasing T.

The variation of thickness of the Ni and Ni-Ge film as a function of annealing temperature (T) was determined by SEM as presented in Fig. 4.17. This thickness is seen to increase with increasing T. Theoretically the ratio of the atomic volume of NiGe and Ni is 2.44. From Fig. 4.17 the ratio of the film thickness of NiGe at 500 °C to that of Ni is 2.53. This confirms complete reaction of the 70 nm Ni and formation of NiGe at that temperature.

In order to further exploit the Germanidation mechanism the sheet resistance

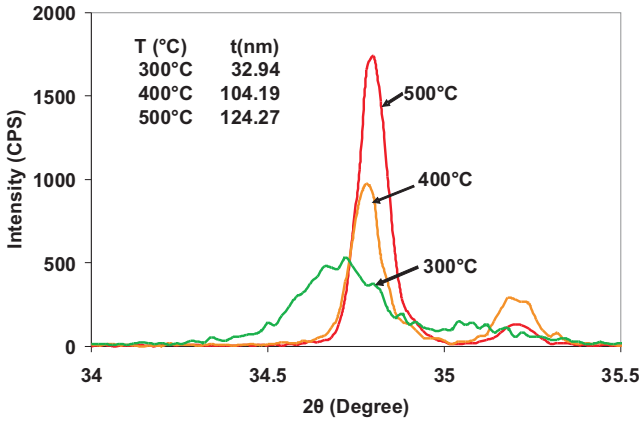

Figure 4.16: XRD spectra showing the NiGe(111) peak of the Ni(70nm)/Ge samples when annealed at various temperatures. The calculated crystallites are presented in the insert. This plot was prepared by Muhammad Husain.

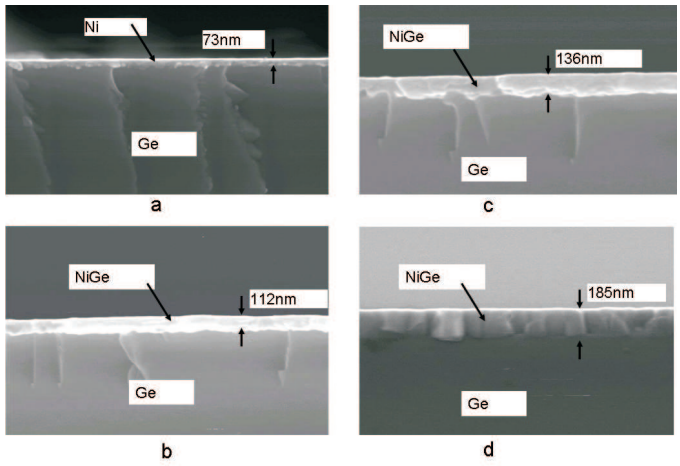

Figure 4.17: Cross sectional SEM images of the various Ni/Ge samples: (a) as-deposited, (b) annealed at 300 °C, (c) annealed at 400 °C, and (d) annealed at 500 °C.

(R_{sh}) of the grown films was measured using the four-point probe method. The obtained R_{sh} values were multiplied by the film thicknesses to calculate the film resistivities (ρ). The results are plotted as a function of annealing temperatures in Fig. 4.18. It is observed that R_{sh} decreased with increasing T. The measured R_{sh} of NiGe is 0.23 Ω/sq when annealed at 500 °C. The low R_{sh} could be attributed to the increase in crystallite size at 500 °C as observed in Fig. 4.16. The resistivity of Ni-Ge also decreased when the films were annealed above 300 °C.

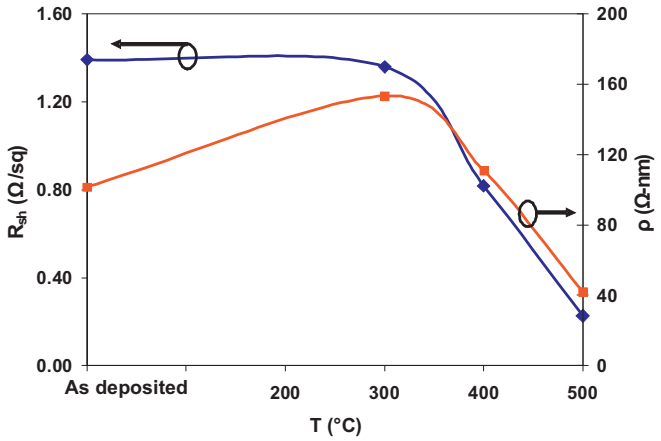

Figure 4.18: R_{sh} and ρ of Ni and Ni-Ge films at various annealing temperatures. The initial Ni thickness was 70 nm. The substrate resistivity was 0.005-0.02 Ω-cm. This plot was prepared by Muhammad Husain.

Typical I-V characteristics of the grown Ni(70nm)/Ge Schottky diodes under the as-deposited and annealed conditions on lowly resistive (0.005-0.02 Ω-cm) Ge are presented in Fig. 4.19 for a contact pad size of 20 μm square.

A high quality rectifying behaviour (4-5 orders in magnitude) is observed for all annealing conditions. Again, ϕ_n, η and R_s are calculated assuming the TE model in the forward bias region and are presented in Table 4.2. The values of ϕ_n are virtually constant at 0.52 V. Assuming a Ge band gap of 0.66 V the corresponding hole barrier height (ϕ_p) is 0.14 V. This value is low enough to guarantee a large ON current in a SB-MOSFET. At low forward bias there is a considerable overlap of the current curves of the non-annealed Ni-Ge, and NiGe-Ge samples as observed in Fig. 4.19. This indicates both thermal stability and Fermi level pinning in the Ge band gap as the barrier height is independent of the metal work function. The reverse current at 1V bias is 1 μA for the various annealed diodes. This is a significant achievement as this value is more than an order of magnitude smaller than the reported value in literature[75] for NiGe/Ge diodes formed by evaporation on highly resistive (4-6 Ω-cm) Ge.

The low values of ideality factor for the Schottky diodes presented in Table 4.2 indicate TE to be the dominant current conduction mechanism in the forward bias. The series resistance decreases with increasing T (see the insert of Fig. 4.19) indicating

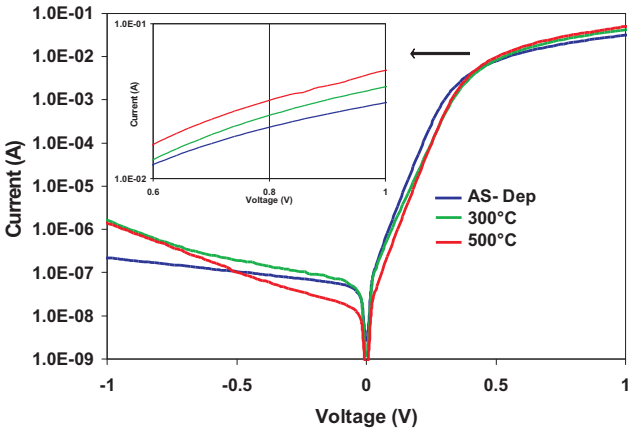

Figure 4.19: I-V characteristics of the Ni/Ge Schottky diodes, having a contact area of 20 μm^2 square, as a function of annealing temperatures. Ge resistivity was 0.005-0.02 Ω-cm. The high forward bias region is magnified in the insert.

T (°)	ϕ_n(V)	η	R_s (Ω)
RT	0.52	1.1	21.32
300	0.52	1.27	14.79
400	0.55	1.13	11.83
500	0.55	1.08	10.85

Table 4.2: The Parameters of Schottky Barriers' I-V Characteristics. The Schottky contacts with contact area of 20 μm^2 square are built on Ge (0.005-0.02 Ω-cm) by nickel electrodeposition under the different annealing temperature.

lower specific resistance of NiGe than Ni. This is consistent with the four point probe measurement presented in Fig. 4.18. Simulations of the operation of Ge Schottky barrier FETS based on our experimental diodes is described further in our publication Ref.[80].

4.5 Conclusions

The reviews of Spintronics in the beginning of this chapter outlines the fundamental concepts and recent developments in this new discipline. In the study of vertical spin valves, our experimental results clearly show that an electrically well functioning back to back diode can be fabricated using the membrane technique and further experiments can build upon these results though no MR signal was observed at present.

In the study of lateral spin valves, Ni/Ge Schottky barriers formed by electrodeposition on highly doped substrate shows high rectification with low leakage current in reverse bias. The fabricated Ni/Ge diodes transformed into NiGe/Ge diodes upon annealing at 500 °C. Despite the compositional change the Schottky barrier properties were virtually unaltered due to Fermi level pinning. The series resistances of NiGe decreased with annealing temperature which is important for a high drive current in SB-MOSFETs. Therefore, it is proposed that electrodeposition should be used for source drain formation of a highly doped, Ge based SB-MOSFET to achieve low sub-threshold leakage current.

Chapter 5

Magnetic Switching in Ni Nanoscale Void Arrays

5.1 Introduction

Nano-patterned magnetic materials are very attractive for fundamental studies on magnetism, applications such as patterned storage media, and spintronic devices. However, the limitations of conventional lithography, and the high cost of e-beam lithography, limits widespread use of applications in this field. To overcome these restrictions, self-assembly has been widely proposed as an alternative technique. Self-assembly is the autonomous organization of components into patterns, or structures, without human intervention [81]. Such structures can be used as templates to transfer the pattern to magnetic materials. A variety of natural systems with self-assembly properties has been used for this purpose including lyotropic liquid crystals [82], anodised alumina membranes [83], block copolymers [84] and close packed arrays of polystyrene latex and silica spheres [85, 86].

While these systems provide well-ordered, short range periodic templates, they lack long-range order, the ability to determine the precise position, and direction of the periodic structure. In order to address these issues, guiding of the self-assembly has been proposed. This is a hybrid method involving pre-patterning of the substrate using conventional fabrication techniques to assist the self-assembly process. Guided block copolymer self-assembly has been studied showing remarkable guid-

ing effects [87] and lithographically defined patterns have been used to aid the self-assembly of close packed spheres [88, 89, 90, 91, 92, 93]. In this chapter, we will introduce the techniques used for self assembly, expand on the fabrication of templates, and discuss the results of guided self assembly.

5.2 Theory of Self-Assembly

Currently, there are two approaches to fabricate the ordered nano structures: top-down and bottom-up. A top-down model establishes an overview of the system without detail for any part of it. Each new part may be defined in more detail until the entire specification is detailed enough to begin development. Top-down has been the traditional approach to miniaturization by different lithographic tools, such as electron beam lithography, X-ray lithography, laser interference lithography, scanning probe lithography, step growth methods [94]. But lithography is very costly once it scales down. This is where the bottom-up approach becomes promising. A bottom-up model designs individual parts of the system in detail, and a complete system is formed by linking parts together. Bottom-up is self-assembly from molecular-precursor building blocks. Though self-assembly encompasses the domains of chemistry and biology, it is not limited to these domains, or length scales. The obvious advantages of bottom-up fabrication are attainment of three-dimensional assembly, achievement of atomic sizes, and low-cost fabrication [95]. Certainly, these two strategies can be combined. Ross *et al.* [96] combined 'bottom-up' self-assembly with 'top-down' patterned templates to achieve long-range ordered block-copolymer nano structures.

"Self-assembly" has become an applied approach in more and more scientific fields in recent years. How to define the exact concept of self-assembly looks very difficult because the applications of this technology are too extensive. Different from 'formation' or 'growth', self-assembly is an autonomous process. The unique characteristic of self-assembly is that the components can be voluntarily organized to construct stable, robust and well-ordered aggregates or networks. In addition, several other vital characteristics have caused self-assembly to become popular in the field of device fabrication [97, 98, 99]. Firstly, self-assembly is a very low-cost process. Secondly, the

fabrication process is relatively easy. Thirdly, the system consumes minimum energy. Finally, this technology is a very good way to assemble nanostructures, which can be applied in various scientific fields from organic molecules to bioelectronic sensor, from semiconductor quantum dots to robotics and computer networks.

There are several different points of view of how to sort self-assembly [100, 99, 101]: From the thermodynamic point of view, self-assembly is divided into static self-assembly and dynamic self-assembly. The difference is that the system dissipates energy in the latter process. From the fabrication point of view, self-assembly is classified as Langmuir-Blodgett (LB), electrostatic, surface forces, chemical and biomolecule-assisted self-assembly techniques. From the nanostructures' morphology point of view, self-assembly is sorted as 2D arrays and 3D networks.

5.2.1 Langmuir-Blodgett Assembly

Before self-assembly techniques were common knowledge, the traditional method of ultrathin film fabrication was the Langmuir-Blodgett (LB) technique, which was published by Blodgett, K. B. and Langmuir, I. in 1937 [102]. This method consists of one molecular layer deposited at a time on a crystalline film at the air-water interface, by dipping the substrate into water containing a polymer that forms a single layer of molecular chains on the surface. This layer is then transferred from the water to the substrate. The dipping can be repeated to create an ordered multilayered film that does not require poling to orient the molecules. As shown in Fig. 5.1, the first step of the LB method is that the surfactant is spread on the water surface within a highly volatile solvent. After the evaporation of the solvent, the molecules start to reorganize. At this point, some spaces exist among the molecules and the film is not continuous. The second step is that a barrier on the water surface pushes the molecules together. A feedback (Wilhelmy plate) controls the position of the barrier and thus the pressure. Before this step, the pressure-area isotherms of the surfactant must be studied. After these two steps, the deposition on a solid substrate can be carried out. In recent years, the LB technique has been shown to transfer a nearly defect-free long range ordered monolayer from aqueous solution surface to a solid substrate[103]. However, the LB technique can not overcome several disadvantages, such as the high cost of equipment and maintenance, time-consuming and cumbersome.

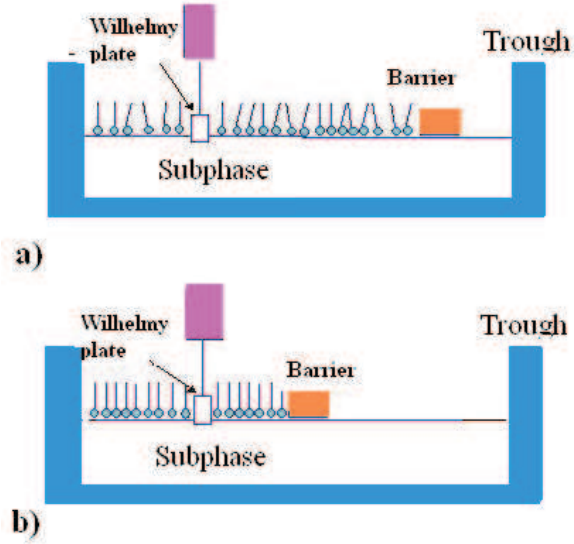

Figure 5.1: The Langmuir Blodgett method steps: (a) The surfactant is spread on the water surface within a high volatile solvent. (b) Then a barrier on the water surface pushes the molecules together.

5.2.2 Self-assembly Monolayers

Self-assembly monolayers (SAMs) address the disadvantages discussed in LB techniques [100, 104, 105]. The self-assembled monolayer, a type of tightly arranged monolayer achieved by spontaneous formation, can be prepared simply by immersing the substrate into the appropriate solution which contains the desired molecule and washing off the excess. Here, the molecules arrange without guidance, or management, from an outside source, such as the barrier used in the LB method. Typically, it is carried out with oxide-bearing substrates with organosilanes, or coinage metal, substrates with alkanethiols (Ref.[100]). At present, there are two main types of method to format SAMs. The first method is the silanation of the substrate (typically glass) by surfactant silanes, or siloxanes. The second method is formation of sulphur coinage-metal (typically gold) covalent bonds. These two methods both have no high requirement of mechanical manipulation, so a SAM is cheap and easy to fabricate. In addition, the surfactant organization in SAMs is primarily dependent on the nature of the substrate while that in a LB film is determined by the parameters of the monolayer formation[101].

Lateral Capillary Forces

In nature, the driving forces of aggregation are different from macro world to micro world. In the large scale world, gravity, which is proportional to the mass, is the dominating force. While in the micro scale world, the intermolecular force, which is proportional to the surface area, is the most important force. Therefore, the mechanism of self-assembly is based on the intermolecular force. The capillary force is the dominating intermolecular force. In general, capillary forces are depicted as the interactions between particles, mediated by fluid interfaces. There are two main types of capillary forces: normal capillary forces and lateral capillary forces [106]. As shown in Fig. 5.2, in the normal capillary force case, the liquid phase or gas phase forms a liquid-in-gas, or gas-in-liquid, capillary bridge between two particles or bodies. Then the capillary force is directed normal to the planes of the contact lines on the particle surfaces due to the particle-particle and particle-wall interactions. The forces can be attractive or repulsive depending on whether the capillary bridge is concave or convex. Attractive forces of this type lead to three-dimensional aggregation and consolidation of bodies built up from particulate. A spontaneous formation of sub-micrometer, gas-filled capillary bridges in water is caused by the hydrophobic surface force. In the lateral capillary forces case, because each individual particle has some meniscus in the shape of a liquid interface or film, the forces are formed by the overlap of the menisci around two particles. Different from the former, this force is parallel to the contact line. It can also be attractive or repulsive depending on whether the overlapping menisci, formed around the two particles, are both concave or convex, or one is concave and the other is convex. Attractive forces of this type cause two-dimensional aggregation.

Furthermore, the lateral capillary forces are divided into flotation forces and immersion forces. The flotation lateral capillary force, the effect due to particle weight and buoyancy force, is employed for self-assembly of floating meso-scale objects. The immersion lateral capillary force is the effect due to the wettability of the particles, or bodies, because the wetting properties of the particle surface, such as position and shape of the contact line, and the magnitude of the contact angle decides the degree of deformation of the menisci. This force is acted on in the 2D aggregation and ordering of micrometer-sized, and sub-micrometer, particles confined in the wetting film.

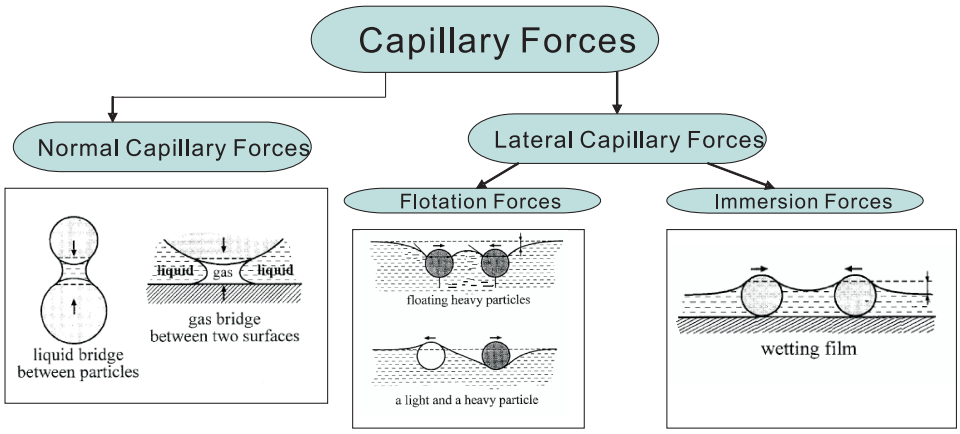

Figure 5.2: Types of capillary forces [106].

Formation Mechanism of SAMs

There are five essential requirements for 2D assembly: 1) stable wetting substrate. 2) repulsive nano spheres with identical size. 3) lateral capillary force. 4) convective assembly due to evaporation and 5) the saturated water vapour at the suspension surface. The typical process of formation of well ordered 2D arrays of latex spheres is generally the evaporation of the drops of colloidal suspensions on solid hydrophilic substrates. The formational mechanism and the governing forces of this type of 2D assembled array were clarified by Nagayama et al. [107, 108]. The process had two stages: nucleus formation and crystal growth. The nucleus formation happened under the action of attractive capillary immersion forces and the crystal growth took place through convective particle flux caused by the water evaporation from the already ordered array. Through an appropriate adjustment of the shape of the liquid film surface and of the water evaporation rate, it is possible to control the production of ordered mono- or multi-layers of sphere arrays. Subsequently, the new concept 'convective assembly' was introduced to identify this mechanism of sphere ordering under the action of capillary immersion force and hydrodynamic drag force [109].

In suspension, the colloidal spheres are liberated from gravity and obtain the intermolecular force, particularly the microscopic attraction between surfaces, by means of surface tension. In the beginning, the nano spheres only make the Brownian motion in a sufficiently thick liquid film. However, once the thickness of the liquid film becomes a comparable size to the particle, two new phenomena emerge, which are

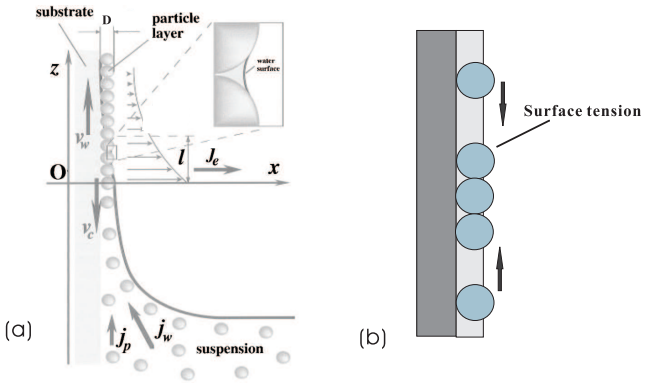

Figure 5.3: Sketch of the movement of the particles suspended in the thin liquid film. (a) Directional movement of particles carried by convective flow of water moving from the meniscus area toward the array boundary where water is removed by evaporation and hence particles are left dried. (b) Movement of particles forced by the attractive interaction (lateral capillary force) exerted between two particles protruding their heads from the water surface. The deformed water surface in conjunction with the surface tension is the origin of the 2D force. [110, 109]

shown in Fig. 5.3. One is convective assembly (Fig. 5.3(a)). The spheres in the thick liquid film are carried to the liquid film edge by water current. The water current is caused by evaporation of water in the meniscus area. The water current is a type of convection that causes water from thick liquid areas to flow to the dry area in order to wet it when the suspension at the edge dries by evaporation. The other is the lateral capillary force (Fig. 5.3(b)), which originated from the surface tension between the spheres which protrude from the surface, and which packs spheres into hexagonal arrays. It should be noticed that the diameters of the spheres are larger than 100 nm if the self-assembly takes place on the silicon or silicon dioxide substrate because the minimum thickness of stable wetting film of silicon and silicon dioxide is about 100 nm.

5.2.3 Guided Self-Assembly

Following the pioneer work on the assembly of 2D colloidal sphere arrays by the Nagayama's group, many studies took place to progress high quality 2D self-assembly arrays. Instead of dropping the suspension, the suspension spreading has been facilitated by applying the spin-coating technique [111]. The quality of the final ordered array can be improved if appropriate agitation by ultra sound is applied during the

film drying process [112]. In addition, tilting the horizontal substrate to an appropriate angle is also a way to help the self-assembly. The array formation starts at the upper edge of the drop and proceeds downwards [113].

However, the essence of above improved methods was that the substrate, where self-assembly happened, was a flat surface. It has not intrinsically changed the mechanism of spheres' assembly. Researchers began to consider if patterned substrates could act in a new type of driving force opposite to capillary force. Hence, physical constraint and lateral capillary force are combined to control the process of self-assembly. This type of self-assembly technique is called guided self-assembly. For colloidal spheres, the interaction between them are often non-directional(in a sense, very similar to ionic bonding and metallic bonding). However, the physical constraint, which is the excluded volume interactions between spheres and the walls of the templates, is directional. Therefore, the orientation of colloidal crystals is primarily laid on physical constraint.

In the case of colloidal spheres self-assembly on a plane substrate, the lattices is often close-packed structures since the lateral dimensions of these channels are relatively large in comparison to the sizes of the colloidal spheres. Well-defined trenches, with the comparable size of the spheres, will lead to additional packing structures besides close-packed structures based on physical confinement and attractive capillary forces.

These trenches could serve as physical traps for the liquid and the colloidal spheres. As the edge of the meniscus moved slowly via a dewetting process, the capillary force exerted on this edge will drag the colloidal spheres across surface of the bottom substrate until they were physically trapped by the trenches [114]. The colloidal spheres retained in each trench always tend to be in physical contact as a result of the attractive capillary forces formed during solvent evaporation. The meniscus-induced capillary force is strong enough to remove the extra spheres along with the dewetting liquid [115]. As shown in Fig. 5.4(D), the angle θ is determined by

$$\sin\theta = \frac{W - D}{D} \tag{5.1}$$

When W is equal to or smaller than D, θ is always zero. Fig. 5.4(A) shows this case, where the spheres align into a straight, linear chain. Fig. 5.4(B) shows the angle was consistent with the calculated value by applying equation 5.1. Fig. 5.4(C) shows a

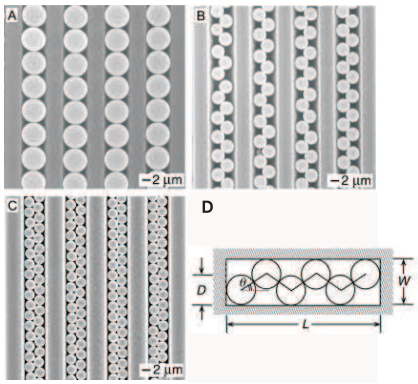

Figure 5.4: (A,B,C) The SEM images of three typical chain-like aggregates that were assembled in 2D arrays of channels that had L = 2 cm, W = 5.0 μm, and H = 2.3 μm. The polystyrene beads used here were 5.7, 3.1, and 2.5 μm in diameter, respectively. [116].

special case when W is equal to, or bigger than, 1.866D, the colloidal spheres only prefer to form in a centre close-packed structure since this type of structure has the highest density.

The first computational model of assembly of colloidal spheres into helical chains was performed by Pickett et al., where they were packed under cylindrical confinement [117]. This process was mainly driven by the excluded volume interaction (between colloids and the walls of cylindrical holes, and among colloids), a constraint that requires no overlapping between any two physical bodies. By controlling the ratio between the diameters of cylindrical holes and colloids, a number of helical structures were observed, albeit the right- and left-handed spirals appeared with roughly the same probability and the final product was a racemic mixture.

The first experimental study of these kinds of helical chains aggregated by colloidal spheres were fabricated by Xia et al., where V-shaped groove with triangular cross sections were used instead of cylindrical holes [118]. As shown in Fig. 5.5(A), the physical constraint provided by the walls of these grooves can drive monodisperse spherical colloids to assemble into helical chains. The structural arrangement among these colloids is determined by the ratio between the width of the V-grooves (W) and the diameter of the colloidal sphere (D). When W/D falls between 2.70 and 2.85, double-layered structures with a helical morphology will be formed (Fig. 5.5(B-D)). The bottom layer will be an array of discrete particles that are only connected to each

other through the "dimers" sitting atop. As the suspension dewetted from the fluidic cell, a meniscus was formed at its rear edge. The capillary force (F_c), originating from this meniscus, was strong enough to push all colloidal spheres into the V-grooves and left almost no beads on the top surface of the Si(100) wafer. In addition, they further investigated the factors determining the chirality of these spiral chains and made the conclusion that the direction of capillary forces relative to the longitudinal axis of the V-grooves was the dominant factor. The corresponding structures observed in different regions are shown in Fig. 5.5(B-D). Obviously, regions (B) and (D) were left-right mirror images, and helical chains obtained from these two regions exhibited opposite signs of rotation. The exact rotation of these spiral chains depends on how the liquid front was curved relative to the flow direction. When the edge of the meniscus moves towards the right hand side (as viewed along the direction of liquid flow, region B), the capillary force (F_c) drives the spherical colloids into left-handed spirals, and bending to the left side (region D) led to the formation of the other pure enantiomer. In region (C) where the capillary force was parallel to the longitudinal axis of V-grooves, both left- and right-handed helical senses were equally probable, and intrachain helical reversal might also occur. As illustrated in Fig. 5.5(c), the handedness of each segment within an individual spiral chain were randomized.

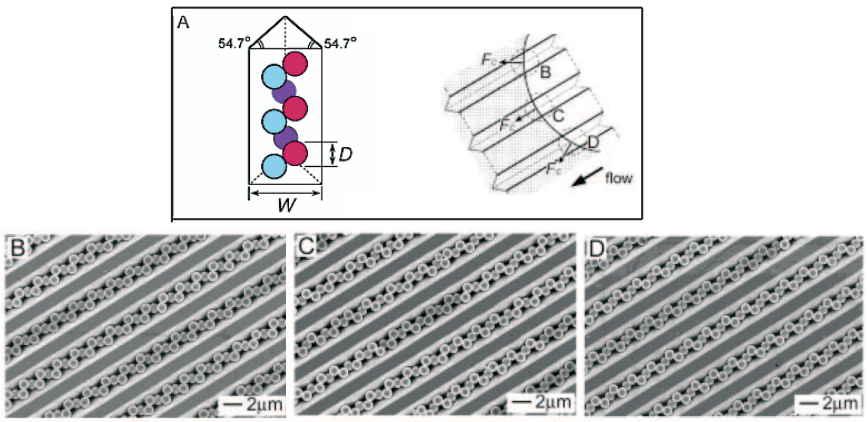

Figure 5.5: Self-assembly of spherical colloids into Helical chains in V-shaped grooves. (A) Schematic illustration showing the formation of a helical structure. (B-D) SEM images of helical chains with different chiralities that were obtained with the capillary forces oriented toward different directions relative to the longitudinal axis of the V-grooves. [118].

5.3 Template Fabrication

Generally, the etching methods are divided into anisotropic etching and isotropic etching [19]. If h_f is the thickness of the layer material and l the lateral distance etched underneath the photoresist mask, the degree of anisotropy A_f is defined as

$$A_f \equiv 1 - \frac{l}{h_f} = 1 - \frac{R_l t}{R_v t} = 1 - \frac{R_l}{R_v} \tag{5.2}$$

where t is the time of etching, R_l and R_V are the lateral and vertical etch rates, respectively. For isotropic etching, R_l=R_V, then A_f=0.

5.3.1 Silicon Dioxide Etching

A wet chemical silicon dioxide etch is a perfectly isotropic etching technique, in which SiO_2 etches in all directions at the same rate, thus it produces round sidewalls as illustrated in Fig. 5.6(a). The disadvantage of wet chemical etching for pattern transfer is the undercutting of the layer underneath the mask, resulting in a loss of resolution in the etched pattern. In practice, for isotropic etching, the film thickness should be about one-third, or less, of the resolution required.

If patterns are required with resolutions much smaller than the film thickness, the anisotropic etching method(i.e., $0 < A_f \leq 1$) must be selected. In practice, the value of Af is chosen to be close to unity. Fig. 5.6(b) shows the limiting case where A_f=1 and the etching produces vertical sidewalls. The current SiO_2 dry etching techniques are based on plasma-assistance. There are several different techniques that use plasma in the form of low pressure discharges, such as basic plasma etching, reactive ion etching (RIE), sputtering etching, magnetically enhanced RIE (MERIE), reactive ion beam etching and high-density plasma (HDP) etching [19].

For this work, both wet etching (Buffered HF) and dry etching (CHF_3 + CF_4 + A_r) were used for pattern transfer. The dry etch achieves the nearly exact dimensions of the pattern, while in the wet etching case, the widths of the trenches always enlarge due to under-etching.

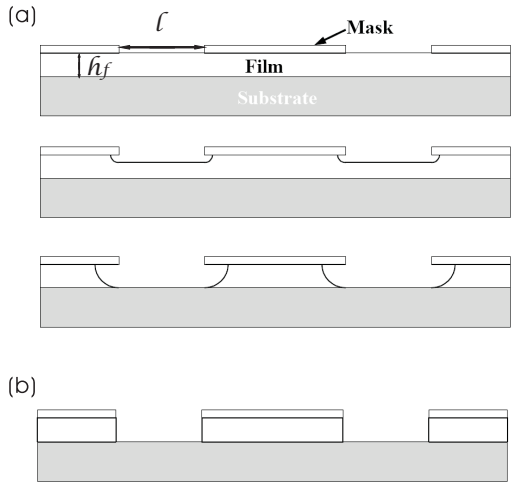

Figure 5.6: Comparison of wet chemical etching and dry etching for pattern transfer. (a) Wet chemical etching is isotropic; (b) Dry etching is anisotropic.

5.3.2 Photolithography Mask Design

On a 6 inch Si wafer, a 5cm × 5cm designed photolithography mask was replicated to cover the whole wafer. In this mask unit, a quarter-cell was rotated by 90°, 180° and 270° respectively and lay out at four corners. As shown in Fig. 5.7, 5.8 and Table 5.1, a quarter-cell is made up of two main parts (part A and part B), where every part is composed of 14 blocks. The length of block (L) is 500 μm. The distance from the upper block's base line to the lower block's is 250μm. In every block, the trench array had 1000 nm gaps in part A and 500 nm gaps in part B. In different blocks the trench's widths (w) vary from 400 nm to 1700 nm. It should be noted that due to the limitation of the photolithography resolution, the blocks (w=400nm & t=250nm, w=500nm & t=250nm and w=400nm & t=350nm) are not successfully developed.

Parameters	Symbols	Dimensions
Si trench length (μm)	L	500
Si trench width (nm)	w	400 to 1700
SiO_2 width (nm)	b	500 or 1000
SiO_2 thickness (nm)	t	250 or 350
Si trench and SiO_2 pitch (nm)	Λ=w+b	900 to 2700

Table 5.1: The dimensional parameters of photolithography mask.

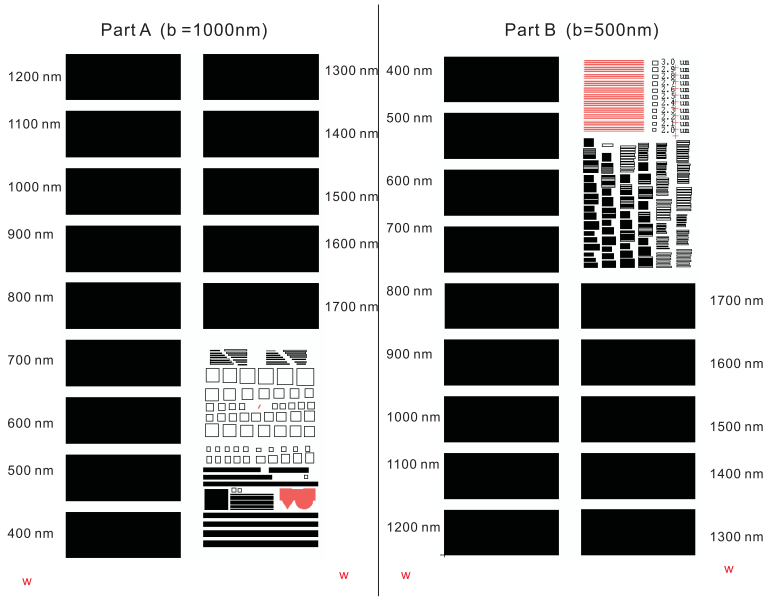

Figure 5.7: The topview of a quarter-cell of the photolithography mask.

5.3.3 Fabrication Process

The process flow for the 2D self-assembled inverse sphere metal arrays guided by a trench is illustrated by Fig. 5.9. On the polished side of an N-type $< 100 >$ silicon wafer with resistivity 0.01∼0.02 $\Omega \cdot cm$, a silicon dioxide layer with 250 nm thickness was thermally grown and a photoresist layer was spun on top. A designed pre-pattern, including strips and trenches, was transferred to the photoresist surface by a Nikon NSR-2005/i9C step and repeat system. Whereafter, the wafer was immersed in a 20:1 Buffered Hydrogen Fluoride (BHF) solution to etch the oxide until the silicon at the selected area was exposed. The photoresist layer was then removed by a fuming nitric acid clean. Finally, the whole piece of silicon wafer was sawn in 6 mm $\times$ 12 mm pieces and processed by an RCA clean. This is a standard 2-step semiconductor industry clean procedure. The stages are : 1) immersing in an aqueous mixture of hydrogen peroxide and ammonium hydroxide; 2) followed by immersing a mixture of hydrogen peroxide and hydrochloric acid. It is aim to remove organic contaminants from the wafer surface; then to remove any oxide layer that may have built up; and finally to remove any ionic or heavy metal contaminants.

The procedure of assembly of the colloidal spheres required that piece of patterned Si wafers and a piece of microscope specimen glass are stuck together by a trapeziform

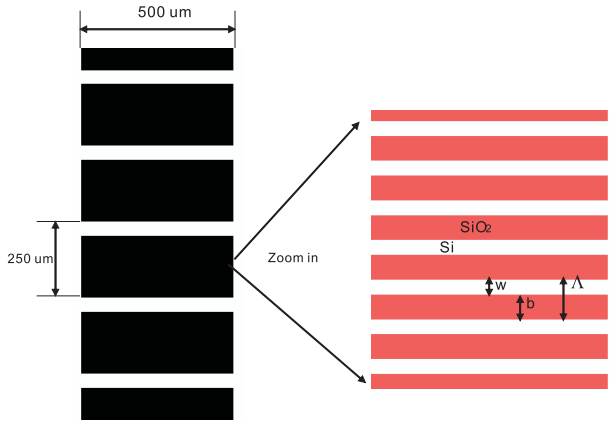

Figure 5.8: The zoomin view of the trench structure. The width of a certain block is round 200um but can not precise to 200 μm because of the fixed Λ.

template to form a sandwich structure. The patterned and polished side of the wafer face to the glass. The groove template was made by one layer of parafilm, which effectively prevents the leakage. A hatch between wafer and glass was left to fill in with the colloidal solution, which was produced by Duke Scientific Corporation and contained 1wt% of 520($\pm$5) nm diameter polystyrene spheres in water. The sandwich sample was placed vertically on glassware using gum and left in a temperature and humidity controllable fridge. The colloidal solution was allowed to evaporate over a period of 36 hours enabling the lateral capillary forces and physical constraint to pack the spheres into the trenches. After all of the water had evaporated, the groove template was dismounted to leave a groove-shape template area covered by the polystyrene latex spheres on the silicon substrates. If the self-assembly template appeared clearly opalescent with colors from green to red, depending on the angle of observation, when the samples were illuminated from above by white light, the templates were robust with good adhesion to the silicon substrates. It was then possible to continue to the next step – metal electrodeposition. After electrodeposition, the sample was placed into dimethylformamide (DMF) solvent and washed in an ultrasonic tank for 2 hours in order to dissolve the latex spheres. Finally, inverse sphere metal arrays were achieved.

In this self-assembly method, the latex sphere template was assembled as a monolayer. If a multilayered template was required, another self-assembly method with the same colloidal solution could be applied. In this case, a 1.0 cm diameter thick

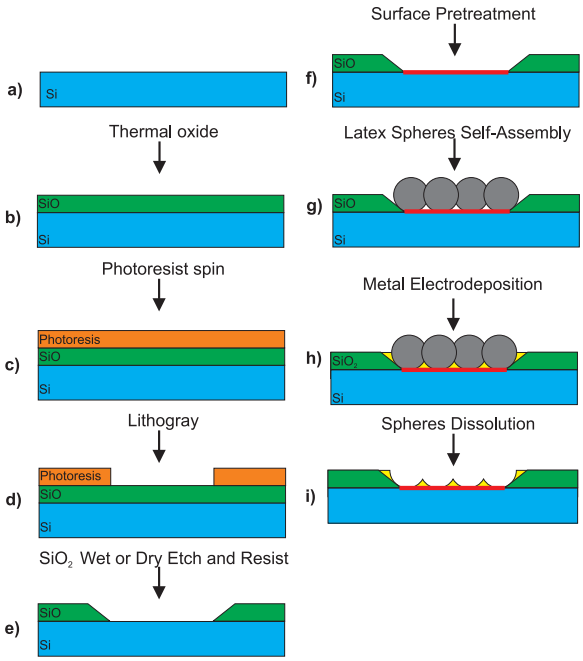

Figure 5.9: Process flow for guided self-assembly of inverse sphere metal arrays guided by flat trench.

Teflon ring, instead of the grooved laboratory sealing film template, was stuck onto the silicon substrate using double sided tape. The substrate was placed flatly and the colloidal solution was spread over the area of the silicon surface enclosed by the Teflon ring. So not only the attractive capillary force but also sedimentation influences the packing of the spheres. The sedimentation process would take about 3 days. Once a clear water layer was observed on the top of the deposit, the sedimentation was finished and it took an another stage of evaporation, which was similar to the monolayer case.

5.4 Experimental Results of Guided Self-assembly

Mentioned in section 5.2.3, the attractive capillary force among the nano spheres is the driving force to pack them in the trenches. Furthermore, this force tends to maximize the density of the remaining structure [107]. Because the maximum density of spheres is achieved by close packing [119], this mechanism leads to self-assembled, face-centered or hexagonal close packed, monolayer or multi-layers.

In order to study the dependence of the self-assembly process on the size of the

guiding patterns, trenches with various widths were fabricated. It is shown in Fig. 5.10 that the width of the trenches has a strong influence on the assembly paths. Referring to Fig. 5.11, it is easy to distinguish three main types of packing mechanism. In Fig. 5.10(a), a 3.6 μm wide trench is too wide for a sphere array of 6 rows and too narrow for 7 rows settling down to the bottom of the trench. As shown in Fig. 5.11(a), 6 rows of spheres adhered at the bottom of the trench and the extra 2 rows are respectively fitted into the voids at both edges of the trench. From the cross section view, they lay on the inclines of the trench. In Fig. 5.10(b), a trench of width of 3.7 μm is used as a guide. This trench is too wide for a 7-row sphere row and too narrow for an 8-row. As a result, a structure of 7rows, with traigonal symmetrical fractures forms to achieve the maximum density. In Fig. 5.10(c), a 3.9 μm wide trench processes a perfectly guided sphere array because its width is commensurate with a close packed sphere array of 8 rows settling down to the bottom of trench. Similarly, in Fig. 5.10(d), an array of 9 rows of spheres crowded in a 4.2 μm wide trench. In Fig. 5.10(e) an array of 8 rows of spheres is guided by a 4.2 μm wide trench resulting in a distorted array. In Fig. 5.10(f) an array of 9 rows of spheres is guided by a 4.3 μm wide trench resulting in perfect guidance.

It should be noted that in some cases, spheres are observed on the SiO_2 as well. But because electrodeposition is chosen as the metallization method to fabricate the metal arrays, and the SiO_2 as an insulator can not become an electrode, the metal arrays do not form on SiO_2. So these templates on SiO_2 are not an obstacle. More details and magnetic measurements of inverse sphere Ni arrays on Si can be found in our paper [9].

As long as the width of trenches is not twice diameter of the colloidal spheres, the spheres in the trenches always assemble into zigzag aggregates, albeit the packing densities are different, depending on the ratio of W and D. Fig. 5.12 shows the experimental result is coincident with the theoretical simulation, as discussed in section 5.2.3. However, the defects that appear in Fig. 5.13 can not be reproduced theoretically. In general, besides the surface tension from silicon, every sphere has two physical contacts with the two side adjacent spheres and one physical contact with silicon dioxide trench walls. These three forces are in the same plane and neutralize each other to achieve the free energy state. Some of the spheres miss one contact

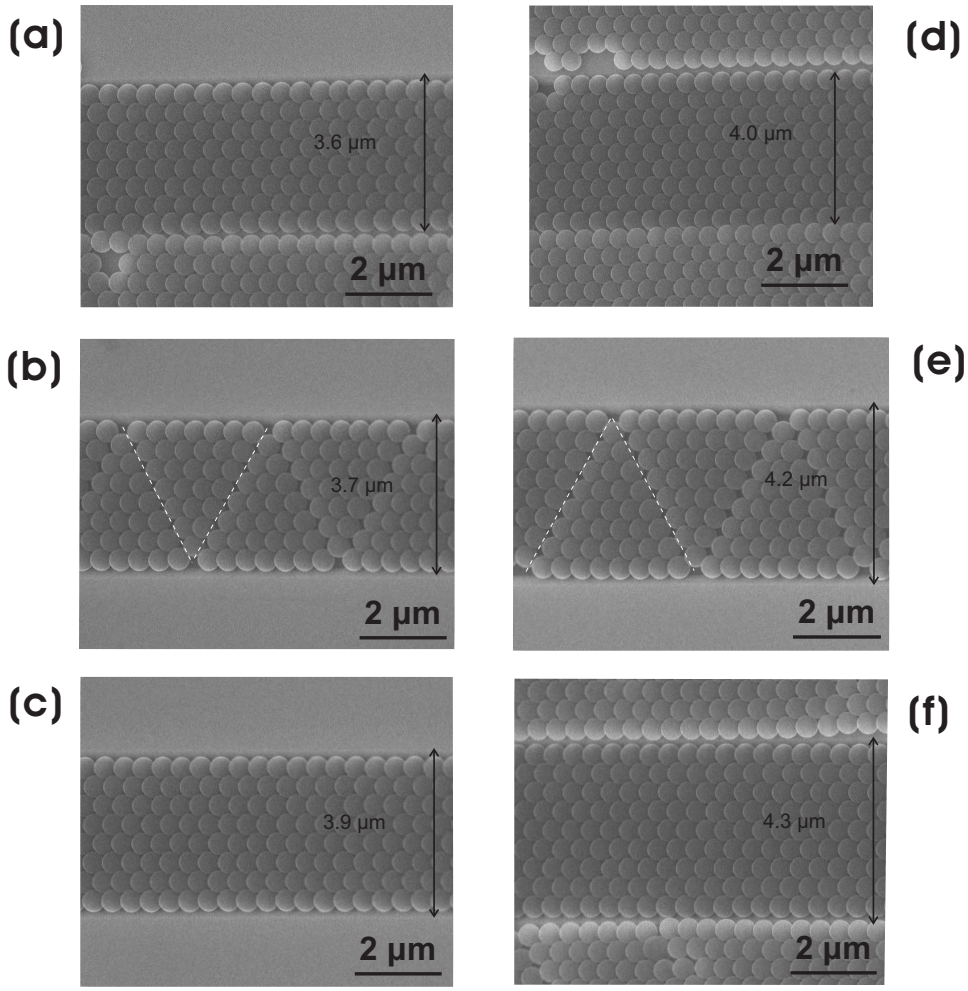

Figure 5.10: Commensurability of guiding patterns is demonstrated by six sizes of trenches. In (a), an array of 8 rows of spheres is guided by a 3.6 μm wide trench. But the two rows at the edges of trench lays on the incline. In (b), an array of 7 rows of spheres is guided by a 3.7 μm wide trench. This excessive width allows for a natural, triangular distortion of the array which increases the sphere density. In (c), an array of 8 rows of spheres is guided by a 3.9 μm wide trench. The dimensional match results in a perfectly guided sphere array. Similarly, in (d) an array of 9 rows of spheres crowded in a 4.2 μm wide trench. In (e) an array of 8 rows of spheres is guided by a 4.2 μm wide trench resulting in a distorted array. In (f) an array of 9 rows of spheres is guided by a 4.3 μm wide trench resulting in perfect guidance.[9]

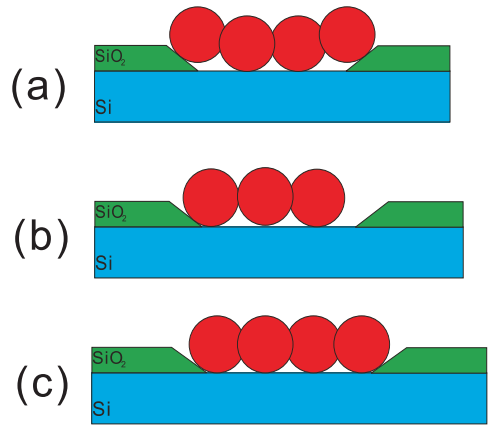

Figure 5.11: Scheme of the cross sections of the guiding patterns. Case (a) relatives to Fig. 5.10(a,d). Case (b) relatives to Fig. 5.10 (b,e). Case (c) relatives to Fig. 5.10(c,f).

either with another sphere or the trench wall. This structure is not very stable.

5.5 Magnetic Characteristics

The excellent rectifying behaviour of the electrodeposited Ni-Si SBs analysed in chapter 3 is now used to prevent substrate leakage currents and allow magnetoresistance measurements to be performed on self-assembled Ni nanovoid arrays directly on Si.

For magnetoresistance measurements, a single layer Ni nanovoid arrays was prepared, shown in fig. 5.9(h). The Ni thickness, controlled by electrodeposition charge, varied from 0 to the sphere diameter. For instance, the thickness of Ni nanovoid arrays was approximately 250nm in fig. 5.14(b). Predetermination of the position of the array allowed Ag pads to be defined, and 4-probe magnetoresistance measurements to be performed. A description of the measurements setup is shown in fig. 5.14(a). Room temperature magnetoresistance measurements were performed using a square modulated current with frequency 68 Hz and a lock-in detection technique. The amplitude of the current was 1 μA for measurements with the magnetic field parallel and 10 μA for those with the magnetic field perpendicular to the current direction.

Magnetoresistance measurements were performed at room temperature on one of the rectangular Ni nanovoid arrays with in-plane dimensions 230x10 μm and height 500 nm. The net current flow was parallel to the long dimension of the rectangle.

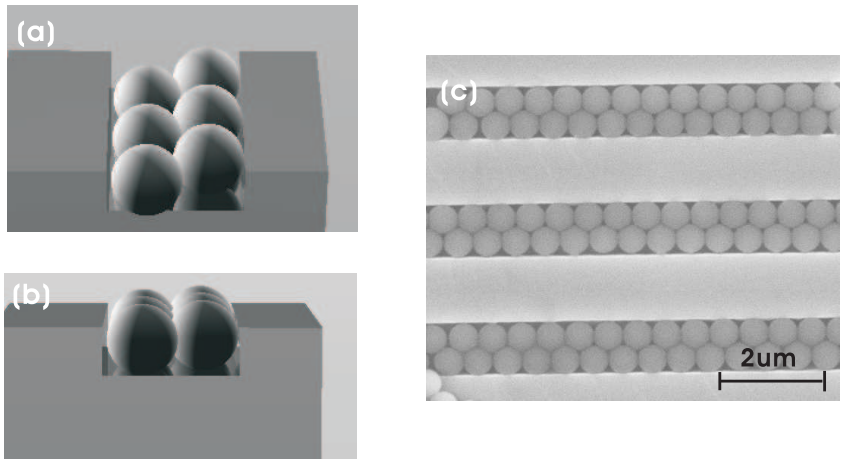

Figure 5.12: a,b) Top view and cross section view of computable models of 2D lattices that were assembled from 520nm colloidal spheres in arrays of trenches that was 1000nm in width. The depth of these trenches was 350 nm. c) SEM image of 2D lattices corresponding to the simulation model.

The resistance of the array at remanence was R(0) = 12.2 Ohm. The in-plane measurements with the magnetic field parallel to the current are shown in fig. 5.15(a. The resistance is at its maximum when the magnetic moments in the array are parallel to the current flow. During the magnetisation reversal process, the magnetic moment turns perpendicular to the current flow resulting in lower resistance. The two distinct minima at -8 mT and +8 mT indicate some hysteresis in the array. Fig. 5.15(b) shows magnetoresistance measurements with the in plane magnetic field perpendicular to the current. The resistance is at its minimum when the magnetic moments in the array are aligned perpendicular to the current flow by the magnetic field. No significant hysteresis is observed indicating a reversible rotation. The maximum resistance for this case is observed when no magnetic field is applied.

According to Eq. 4.2, the Anisotropic magnetoresistance(AMR) of the array can be calculated from Fig. 5.15. The AMR ratio is found to be 0.85%. Similar results have been observed in CoFe anti-dot arrays fabricated by anodised alumina techniques but with weaker AMR effects [120]. This can be attributed to the unique geometry of the inverse sphere arrays which causes interesting magnetisation phenomena [121, 122].

It is noted that smaller resistance variation is observed for magnetisation reversal in the perpendicular direction. This difference could be attributed to the 3-dimensional magnetisation pattern of the zero-field state outweighing the easy axis

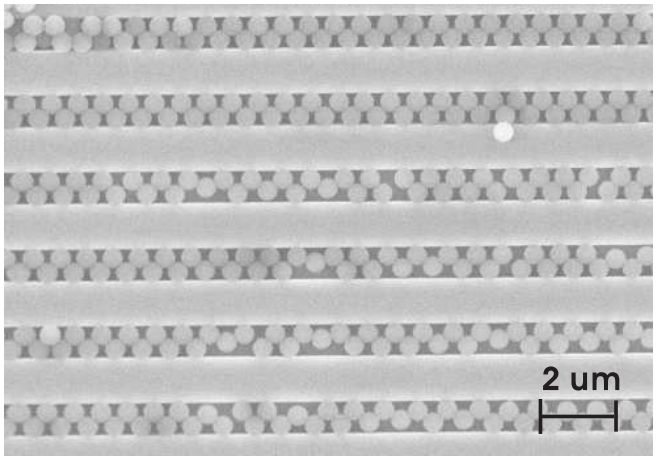

Figure 5.13: SEM image of zigzag aggregates that were generated by assembling 520 nm colloidal spheres into an array of trenches having 700 nm. The depth of these trenches was 350 nm.

preference. However, closer examination of the magnetisation reversal mechanisms in such structures is required for a full explanation of this effect. More detailed studies on the magnetoresistance of these arrays should take into account that the current is not exactly parallel, or perpendicular, to the magnetisation as it follows the inverse spherical geometry.

5.6 Conclusions

The reviews of three main types of self-assemblies in the beginning of this chapter outlines the fundamental theory of self-assembly. The experimental details, which includes silicon dioxide etching, photolithography mask design and the fabrication process of Ni nanovoid arrays are introduced. The results presented and discussed in this chapter reveal that by tailoring the dimensions of the guiding patterns, switching between perfect and triangularly distorted close packed self-assembly symmetries is possible. These patterns are successfully transferred to Ni nanovoid arrays by electrodeposition. The anisotropic magnetoresistance of Ni nanovoid arrays was achieved up to 0.85% at present, which exceeded values obtained from similar structures. This effect is attributed to the unique 3D geometry of the arrays. It is promising for further micromagnetic studies and applications such as patterned storage media and magnetoresistance devices.

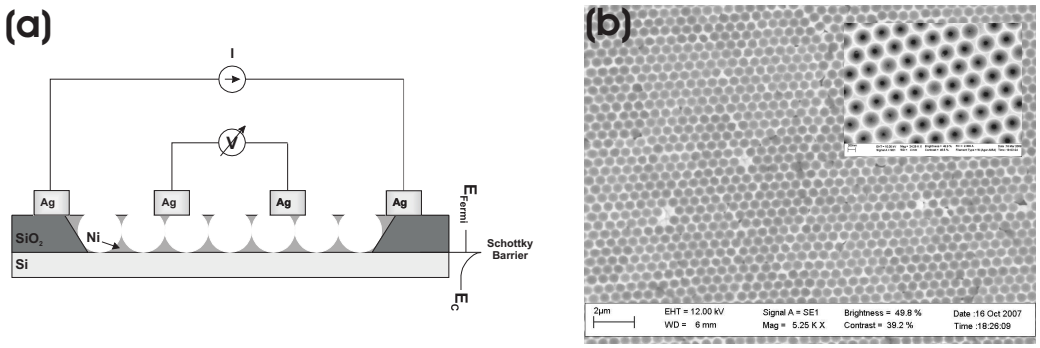

Figure 5.14: (a) Four-probe measurements on guided self-assembly of Ni nanovoid arrays on Si. The size of the spherical voids is not in scale. (b) SEM images of Ni nanovoid arrays with sphere template intact in a 20μm width trench. The nanovoids are grown along the 3D template that was assembled from colloidal spheres with 500 nm nominal width. Inset: The Ni nanovoid arrays after spheres removed.

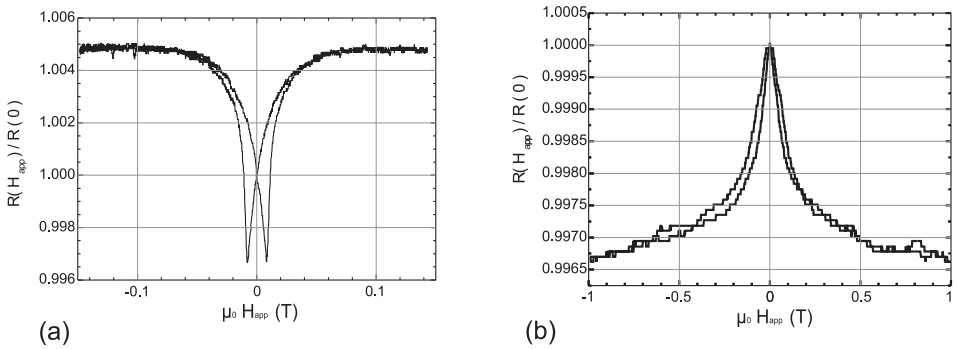

Figure 5.15: Room temperature magnetoresistance measurements at guided self-assembly of Ni nanovoid arrays on Si for in-plane magnetic fields, (a) parallel and (b) perpendicular to the current flow. The MR measurements were done by Dr. Alexander Zhukov.

Chapter 6

Plasmonic modes in Au Nanoscale Void Arrays

6.1 Introduction

Mono-dispersed spherical colloids can self-assemble into one, two, or three-dimensional lattices[123, 124, 109] by various types of driving forces, such as gravity[125], convection[107], spin-coating[111], or electrostatics[126]. To achieve long-range, well-ordered colloidal lattices, a promising approach is guided self-assembly, in which colloidal spheres self-assemble on a patterned substrate[127, 9]. This method allows the formation of shapes of a size which is at least an order of magnitude smaller than that of the pattern made by (photo-) lithography. On flat substrates, spheres self-assemble due to capillary forces into hexagonal close packed mono or multi-layers, as a maximum packing density is the energetically favourable structure[107]. However, on patterned substrates, the main packing force is the surface interactions between the spheres and the walls of the template. Therefore the packing structure of spheres on a patterned substrate is primarily directed by local physical constraints, as shown in Ref. [128, 88, 116, 129, 115]. In this work it has been possible to assemble single layer and multi-layer guided self assembly structures on a sub-micron scale and it is shown that these structures assemble in a different orientation than on an un-patterned substrate.

Such high quality three dimensional colloidal sphere arrays have attracted attention due to their potential to act as a template for the fabrication of 3D photonic

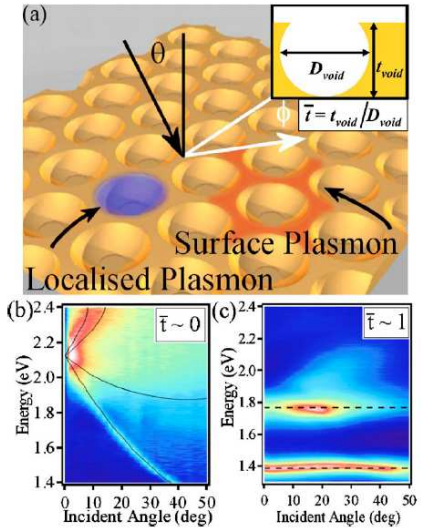

Figure 6.1: (a) Schematic of surface and localized plasmons on nanostructured gold surfaces. Inset shows definition of normalized thickness $\bar{t}$. (b) Typical dispersion of a Bragg plasmon; black lines indicate theoretical dispersion modeled using the Bragg scattering equation. (c) Mie plasmon dispersion; dashed black lines indicate guide to eye. Color scale in both images is blue for 0% plasmon absorption to white for 80% of incident light coupled into the plasmon mode [130].

crystals for waveguide structures, optical filters or switches. In particular it has been shown that spherical nanoscale voids in metal possess different, and potentially more useful, plasmonic modes than nanoscale metal particles. In previous work, it was shown that spherical nanoscale voids, fabricated using a substrate of hexagonal close-packed self assembled spheres as a template, support both propagating and localized plasmon modes, as shown in Figure 6.1[130, 131]. However, in that approach, it has not been possible to control the direction of plasmon propagation. The sub-micron guided self assemblies of spheres fabricated in this work are used as templates to fabricate two- and three-dimensional arrays of nanoscale Au voids in a array with void diameters down to 500nm. This allows us to probe both self assembly formation and plasmon modes with visible light. Plasmon modes are detected and the energy of the plasmons is shown to depend on the dielectric constant at the Au interface. All processes used in the fabrication have the potential to be scaled up and down.

Surface Plasmon Polaritons (SPPs) were first discovered by R.W.Woods in 1902 as he studied the reflected light with a diffraction grating [132] and observed drops in the reflected light at some specific wavelengths. The full theoretical description

of SPPs was given by R.H.Ritchie in the 1950s [133] and improved by H. Raether in the 1960s [134]. On a metal surface, light can be coupled into a surface mode which propagates along the surface of the metal, causing the drop in the reflected light. Nowadays, this field of research is called plasmonics.

To investigate SPPs, incident light should be applied to a nanostructured metallic surface. In this chapter, the method and process of fabrication of these nanostructured metallic surfaces is introduced. Nowadays, self-assembly is regarded as an alternative to overcome restrictions found in both conventional and e-beam lithographic methods for transferring patterns. However, the self-assembly alone can not provide long-range well-ordered arrays. Hence, the hybrid self-assembly method called guided self-assembly, which involves the pre-patterning of the substrate using conventional fabrication techniques to assist the self-assembly process, emerged. It uses the conventional fabrication techniques to make the pre-patterning on the silicon surface, including stripes and trenches, which assist the self-assembly process to reduce the state-of-the-art defect rate. This guided self-assembly method, which could fabricate long-range well-ordered nano latex sphere arrays on a thermally oxidized Si wafer, is applied in this project. The high quality nano sphere arrays are used as a template for metallization to form inverse sphere metal arrays. Because this type of three dimension template has an inverse sphere shape, the common metallization methods, such as evaporation, sputtering, molecular-beam epitaxy (MBE) can not be used as they are line-of-sight techniques. Electrodeposition, as a three-dimensional growth method which can overcome this disadvantage, is applied in this project.

6.2 Basic Theory of Surface Plasmon Polaritons

A coherent fluctuation of surface charges on a conductor boundary is called a surface plasma oscillation. Simply speaking, quantized plasma oscillations are called plasmons. The alkali metals, such as Mg , Al, and the noble metals, such as Ag, Au exhibit this plasmonic behaviour. Plasmons can exist within the bulk metals, and their existence was used to explain energy losses associated with electrons beamed into bulk metals[135]. Under the irradiation of an electromagnetic wave, the free electrons are driven by the electric field to coherently oscillate at a plasma frequency

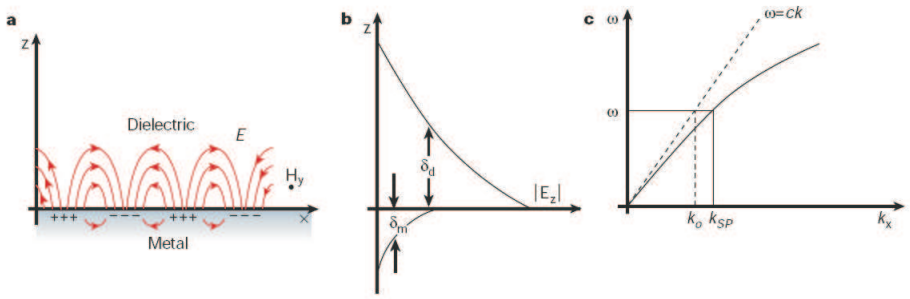

Figure 6.2: (a) the SPPs are a coherent fluctuation in electron density in the surface of a metal, with an E-field normal to the surface, (b) the field above the metal is evanescent and therefore non-radiative, (c) the dispersion relation of SPPs lies to the right of the light line, which represents a free space photon of the same frequency[137].

of ω_p[136]. For a bulk metal of infinite size, ω_p can be described by

$$\omega_p = (Nq^2/\varepsilon_0 m_e)^{1/2} \tag{6.1}$$

where N is the number density of mobile electrons, ε_0 is the dielectric constant of a vacuum, and m_e is the effective mass of an electron.

In reality, any metallic structure of finite dimensions has an interface with surrounding materials, which have different dielectric properties. Surface plasmons (SPs) are a type of plasmon, which can be understood as the electromagnetic waves that propagate along the surface of a conductor, usually a metal. These waves occur at a metal/dielectric interface, where a group of electrons is collectively moving back and fourth[137, 138]. Longitudinal SPs coupled to an EM field are called SPPs. Illustrated in fig. 6.2(a), as the waves of electron density travel along the metal surface, alternating regions of positive and negative charges are produced. To describe the behaviour of SPPs at such a dielectric to metal boundary, it is necessary to solve Maxwell's equations under the appropriate boundary conditions. The electric fields, produced by these regions of differing charge, have z components of electric field exponentially decaying from the interface into both media. In the metal, free electrons undergo longitudinal oscillations, with associated electric field, which penetrate to the skin depth of the metal (<50 nm for Ag and Au[136]). As shown in fig. 6.2(b), above the metal, there is an evanescent field with maximum field at z = 0. Since transverse electric(TE) light has no z component of electric filed, it cannot couple to SPPs and is not considered. Solving the appropriate equations, the SPPs dispersion

relation is yielded[139]. The frequency-dependent SP wave-vector k_{SP} is expressed as

$$k_{SP} = k_0 \sqrt{\frac{\varepsilon_d \varepsilon_m}{\varepsilon_d + \varepsilon_m}} \tag{6.2}$$

where $k_0 = \omega/\mathrm{c}$ is the free-space wavevector, ε_d is the frequency-dependent permittivity of dielectric materials and ε_d is the frequency-dependent permittivity of metal. For k_{SP} having a real component, the absolute value of ε_m needs to be larger than the absolute value of ε_d, and ε_m needs to be negative. The imaginary component of ε_m determines the frequency dependent absorption in the metal, which in turn determines the SPPs propagation length δ_{SP}. In addition, δ_{SP} is also dependent on surface roughness.

As shown in fig. 6.2(c), k_{SP} lies to the right of k_0 and tends toward $\omega_p/\sqrt{2}$, which is the limiting frequency of a 2D plasma. Therefore, the SPPs cannot be coupled by free space photons. To overcome this momentum mismatch, Barnes *et al.* summarized three main solutions[137]: prism coupling, scattering from a defect on a surface, and scattering from a periodically corrugated metal surface. In this work, the third method is applied. Nanoscale void arrays, as a periodic corrugation, will scatter a photon, incident at some angle θ_0, giving it extra momentum, xG, where x is an integer, $\mathrm{G} = 2\pi/\mathrm{y}$ is the void wave-vector and y is the period of the void. k_{SP} is expressed as

$$k_{SP} = k_0 \sin\theta_0 \pm xG \tag{6.3}$$

As illustrated in fig. 6.3, tuning of θ_0 and y allows direct coupling to the SPPs. On the other hand, the periodicity of the metal surface allows the reverse process and the coupling of non-rediative SPPs back to free space photons.

6.3 Template Fabrication

6.3.1 Silicon Wet Etching

Silicon wet etching by KOH belongs to the anisotropic etching techniques. Typical values for the relative etch rate for the three planes of interest are $< 111 >$ (reference) $= 1$, $< 100 > = 300$ to 400, and $< 110 > = 600$ [140]. As shown in Fig. 6.4(a) and (b), orientation-dependent etching of $< 100 >$-oriented silicon through a patterned silicon

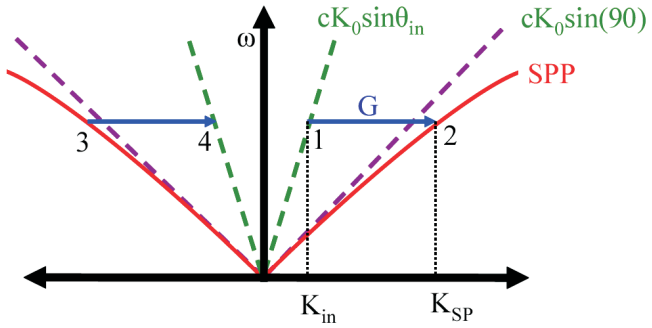

Figure 6.3: Incident light of wave-vector $k_0 \sin\theta_0$. When $k_i n$ is at point 1, the photon is given momentum G and transformed to $k_S P$ at the point 2. The reverse process occurs at point 3 and $k_S P$ decays to the light at point 4 via G.

dioxide mask creates precise V- or U-shaped grooves, the edges being $< 111 >$-planes at an angle of 54.7°. After prolonged etching, the $< 111 >$ plane is exposed down to their common intersection while the $< 100 >$ bottom plane disappears. In addition, fig. 6.4(c) and (d) show that no under-etching of the etch mask is observed due to the perfect alignment of the concave SiO_2 mask [141].

To further study KOH etching, it is important to note that when etching at concave corners on $< 100 >$ Si, it stops at $< 111 >$ intersections while convex corners are underetching, illustrated in Fig. 6.5(a). The SEM images in Fig. 6.5(b) demonstrate how to make a suspension layer from a $< 100 >$ Si wafer.

6.3.2 Fabrication Process

The templates were made using mono-disperse polystyrene latex spheres (Duke Scientific Corporation) supplied as a 1 wt.% solution in water (manufacturer's certified mean diameter of 499 nm ± 5 nm, coefficient of variation in diameter 1.3%). Before use, the suspensions were homogenized by successive, gentle inversions for 5 min followed by a sonication for 15 s. All solvents and chemicals were of reagent quality and were used without further purification. The commercial cyanide free gold plating solution (Tech. Gold 25, containing 7.07 g dm^{-3} gold) was obtained from Technic Inc. (Cranston, RI, USA). Fuming nitric acid and dimethylformamide (DMF) was obtained from Aldrich. 20:1 Buffered hydrogen fluoride (BHF) was obtained from

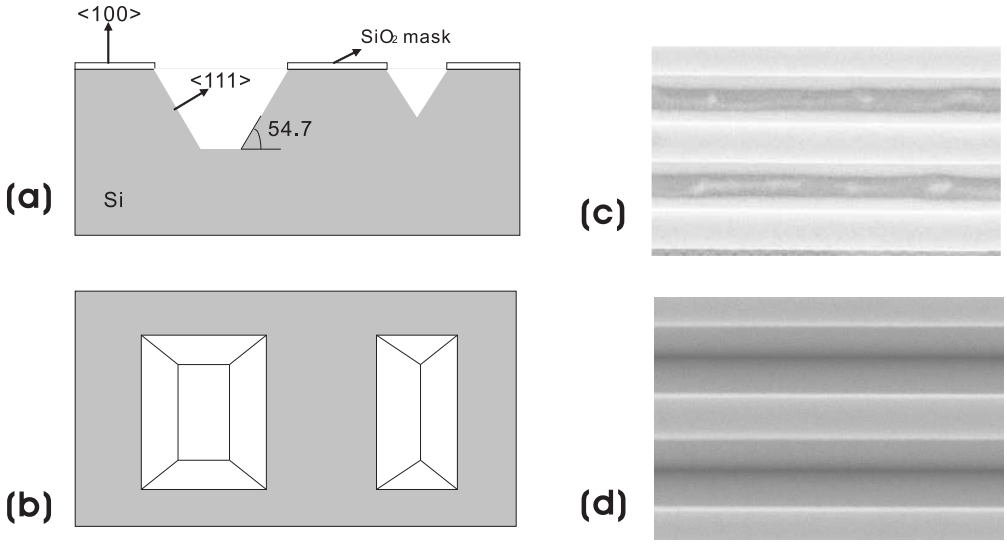

Figure 6.4: Orientation-dependent etching on $< 100 >$ wafer. (a) Cross section; (b) Top view. (c) and (d) SEM images of resulting actual V- and U-grooves by rectangular mask.

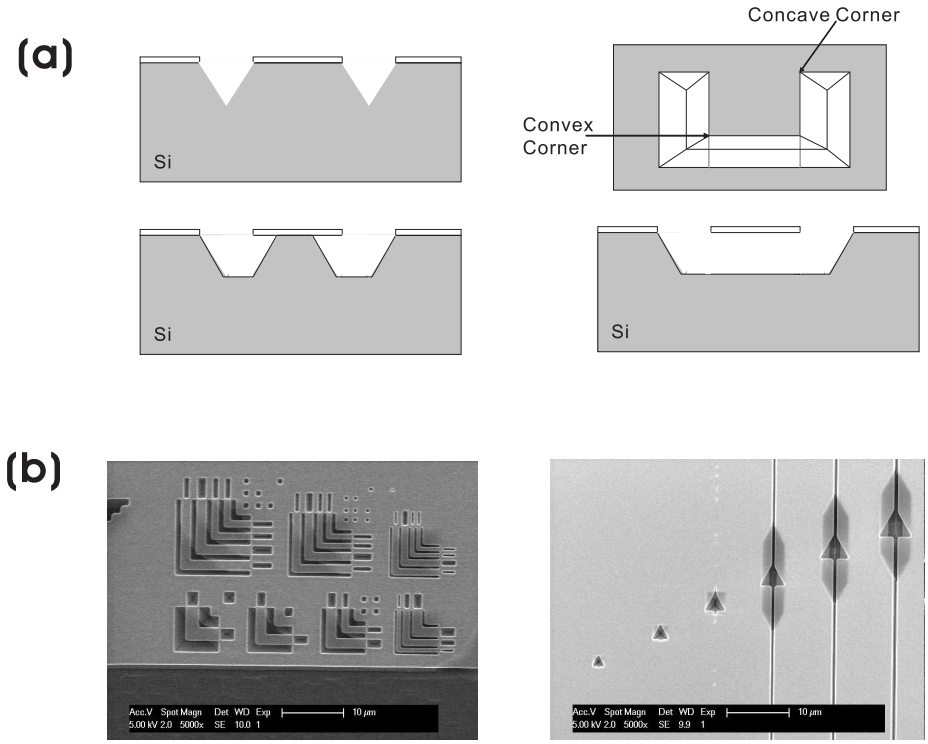

Figure 6.5: (a) Illustration how to make a suspended bridge from a $< 100 >$ Si wafer. (b) SEM images to demonstrate how concave and convex corners act as stop and underetching, respectively. The images were taken by INNOS processing engineer.

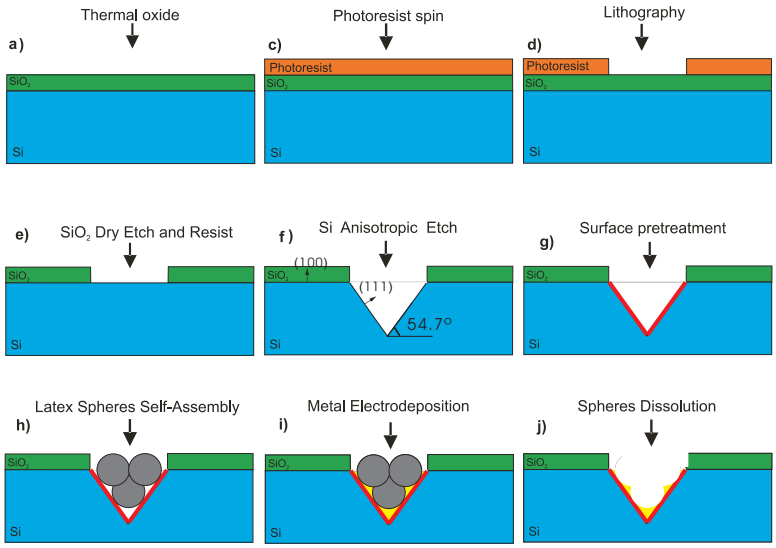

Figure 6.6: Process flow for guided self-assembly of nanoscale void metal arrays in v-shaped trenches.

Rockwood. All solutions were freshly prepared using reagent-grade water (18 MΩcm) from a Cartridge Elga deioniser system.

The pre-patterned Si substrates were prepared from n-type (100)-polished Si substrate wafers with 0.01-0.02 Ω·cm resistivity. The process flow for the samples is outlined in Figure 6.6. A 250 nm layer of SiO2 was thermally grown. A photolithography pattern was then transferred onto the wafer surface using a Nikon NSR-2005/i9C step and repeat system. The oxide was dry etched down to the underlying Si, creating linear trench arrays of 400 μm length, with widths W varying from 500 nm to 1700 nm with a step size of 100 nm and separation between the strips of either 500 nm or 1000 nm. To obtain v-shaped trenches, Si wet etching by KOH was carried out, as shown in Figure 6.6(f). This is an intrinsically anisotropic etching technique. However typical values for the relative etch rate for (111)/(100) planes of Si is about 300 to 400 [140]. Therefore orientation-dependent etching of (100)-polished Si through the patterned SiO2 mask creates precise v-shaped trenches, with an angle of 70.6° between two (111)-planes. Wafers are cleaned using the two-step RCA clean. Prior to the deposition of spheres, a 20:1 BHF dip is used to etch the native oxide layer off the exposed Si. In order to assemble the colloidal spheres on the patterned Si wafer, a clean uncoated microscope slide was attached to the wafer forming a water-tight cell. A layer of Parafilm was used to prevent the leakage from the cell, and a hatch was

left to allow the injection of the colloidal solution. The cell was clamped vertically and the solution allowed to evaporate naturally over 10 hours, enabling assembly of the spheres in the trenches, as shown in Figure 6.6(h). Prior to electrodeposition, a second 20:1 BHF dip (6 s) was necessary to remove the native oxide and leave the Si surface H-terminated. Electrodeposition of gold was then performed at ambient temperature using a conventional three-electrode configuration controlled by an Autolab PGSTAT12. The sample was the working electrode with a platinum gauze counter electrode and a saturated calomel reference electrode (SCE). A pulse of -1.1 V vs. SCE was applied for 0.2 s to nucleate electrodepostion. The gold nanoscale voids were gradually electrodeposited under potentiostatic conditions at -0.7 V vs. SCE. Since SiO_2 is an insulator, electrodeposition only takes place on the Si trench walls, as shown in Figure 6.6(i). After electrodeposition, the sample was placed into dimethylformamide (DMF) solvent and washed in an ultrasonic tank for 2 hours in order to dissolve the latex sphere template. The morphology and nanostructure of both the colloidal templates and gold nanovoid arrays were characterized using Scanning Electron Microscopy (LEO 1455VP SEM).

In this work, we investigated the possible aggregate structures of colloidal spheres with well-define trenches based on physical confinement and attractive capillary forces. Fig. 6.7 is a top view of one sample in low magnitude. The horizontal and vertical blocks of trenches (marked by black rectangles) are clearly identified. The concave curves (marked by white dashed lines) on the surface are the imprints of menisci during evaporation. As section 5.2.3 mentioned, the chirality of sphere chains was determined by the concave curve and direction of the meniscus. Either vertical or horizontal blocks which are located in the middle of the menisci have smaller spans of concave curve than those in sides. Furthermore, in the same positions of menisci, the vertical blocks have smaller spans of concave curve than those in the horizontal blocks. Thus, coherence of assembled structures in the vertical blocks is higher than for those in the horizontal ones corresponding to the same position. Vertical blocks also obtained a higher quality of self-assembly structures.

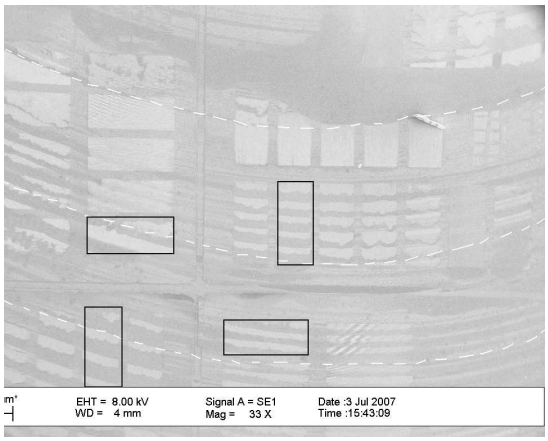

Figure 6.7: SEM image of the top view of one sample in low magnitude. The cambered curves (white dashed) on the surface are the imprints of menisci during evaporation. The black rectangles mark the vertical and horizontal blocks of trenches.

6.4 Experimental Results of Guided Self-assembly in V-shaped Grooves

A 250 nm layer of SiO_2 was thermally grown on a (100)-polished Si substrate and dry etched through a photo-lithographically defined mask to expose the Si as is shown in Figure 6.6. To obtain V-shaped trenches, Si wet etching by potassium hydroxide (KOH) was carried out. As the relative Si etch rate for the (100) planes compared to the (111) planes is about 300 to 400[140], this is in effect an atomically smooth intrinsic anisotropic etching technique, which exposes all the (111) planes. The angle of the trenches is hence well defined, being 70.6° between two (111)-planes, or, equivalent, 54.7° between the horizontal plane and the trench, with the depth of the trench also uniquely defined by the width. Latex spheres are self-assembled in these trenches, as explained in detail in the experimental section. Using a scanning electron microscope (SEM), spheres with nominal diameter $D_n = 500$nm, can be seen assembled three-dimensionally in a trench of nominal width $W_n = 1800$ nm in Figure 6.8.

From the right most trench in the SEM image in which the layer below the top layer is revealed, it is clear that the spheres assemble in a face centred cubic (fcc) lattice with the (001) plane in the plane of the wafer and the (110) direction parallel to the trench length and the Si (110) direction. The number of spheres observed in

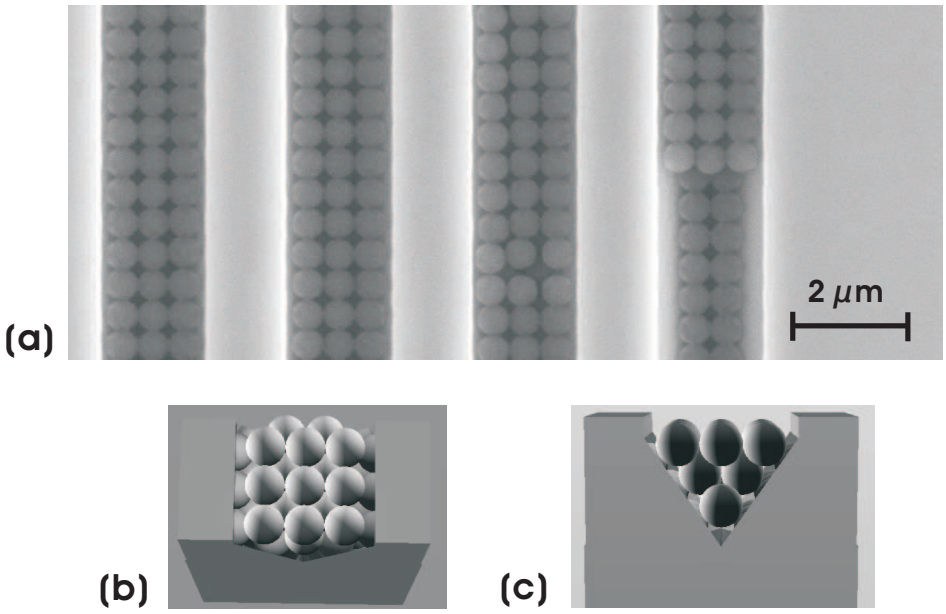

Figure 6.8: (a) SEM image of single dot discrete chain arrays that were assembled by 500 nm colloidal spheres into trenches with 1800 nm nominal width. (b, c) Schematic top view and cross section of structures.

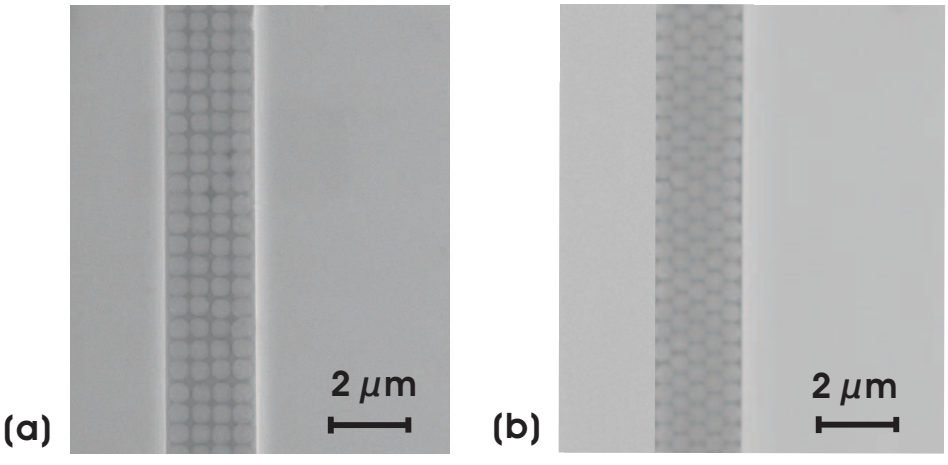

Figure 6.9: Comparison of SEM images of 3D (100) oriented lattices that were assembled from 500 nm colloidal spheres in (a) v-shaped trenches of 2400 nm nominal width and (b) flat bottom trenches of 2300 nm nominal width.

the top layer perpendicular to the trench corresponds to the number of dense packed planes of the colloidal crystal within the V-shaped trenches. The angle in the shown fcc stacking of the spheres with its (111) plane parallel to the crystal Si (111) planes means that the fcc latex sphere lattice has an identical angle to the horizontal plane as the Si. This suggests that the (111) packing of the sphere lattice forms parallel to the trench angled sidewalls, maximising the number of spheres touching the Si wall. Hence fcc is the closest packed arrangement in a KOH etch Si trench when the trench width is commensurate with the sphere size. As comparisons, in Fig. 6.9 both an anisotropically Si etched pattern and a rectangular trench consisting of only a dry etch in the 250 nm layer of SiO_2 are shown. Using the same self assembly process virtually perfect assembly is achieved in both cases but for the flat bottom structure the hexagonal lattice is instead favoured which will build up to an fcc lattice with the (111) plane in the plane of the wafer as shown in Ref[142]. The orientation of the assembled structure is hence predictably controlled by the geometry of the trench.

The full range of sphere packing geometries as a function of trench width and depth is illustrated in Figure 6.10. The trench is tapered from nominal width W_n = 700 nm to 2800 nm with sphere nominal diameter D_n = 600 nm. With increasing trench width the packing includes a transition from a single line of spheres to a helical arrangement, followed by the double, triple, and quadruple structures already discussed above. It is surprising that the transitions between the evidently stable structures is realised within a length of a few micron. Within the 75 micron length of the trench not only are the fcc lattices clearly distinguishable but also the helical structure between single sphere line and two-layer fcc (as shown in Figure 6.10(b)) and another stable structure between the two-layer fcc and the three-layer fcc. The orientation angle of the helical chains as seen in the plane of the Si wafer rotates from 0° to 90° with increasing trench width, providing a smooth transition from the single line to the two-layer fcc lattice. For larger trenches such a defect-free transition does not exist and more disordered areas are evident. However, the many stable structures indicate that the process of self-assembly is one of surprisingly subtle nature in which the latex spheres have enough time, energy, and movement to settle in their lowest energy state.

The best ordering is expected for a commensurate trench size with the width W of

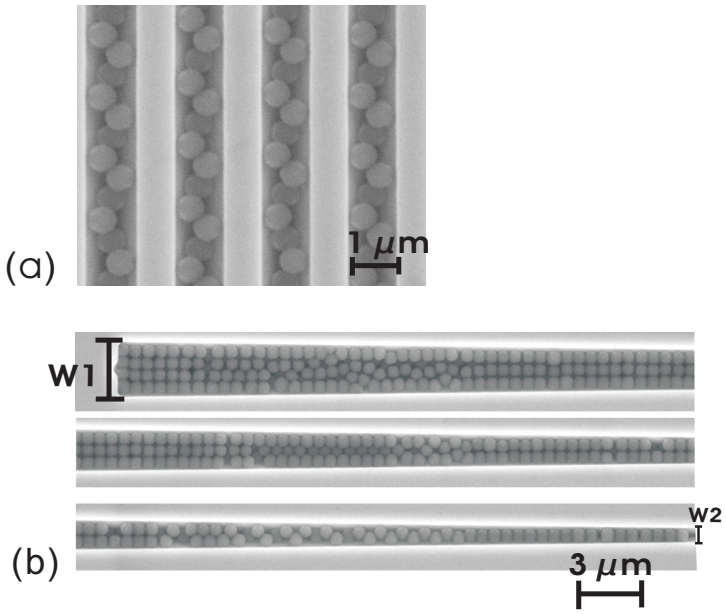

Figure 6.10: (a) SEM images of 3D (100) oriented lattices that were assembled from 500 nm colloidal spheres in trenches of 1100 nm nominal width. (b) Sequential SEM images of 600 nm colloidal spheres assembled in a 3D lattice inside a graded trench. The dimension of trench is L= 75μm, nominal W1 = 2800 nm and nominal W2 = 700 nm.

the trench equal to W = nD+A with n = the integer identical to the number of layers, and A = an offset due to spheres not being able to get to the bottom of the trench. However, as nothing would stop the spheres partially assembling in the anisotropically etched SiO_2 above the Si, the effective off-set can be essentially zero. Although there is some fluctuation, experimentally for sphere diameter D = 500 nm, the four-layer structure assembles best in a trench of nominal width W_n = 2400 nm, the three layer structure in W_n = 1800 nm, the two-layer in W_n = 1200 nm, and the one layer in W_n = 600 nm as shown in Figures 6.8, 6.9 and 6.11. However, due to the small size of the lithographically defined structure, the actual size of the pattern is somewhat smaller than the nominal size. The measured width of the v-shaped trench after KOH etch is given by the equation W_e=(0.92±0.02)W_n-(80±40)nm. The relations between experimental width and sphere diameter for commensurate structures fits very closely the relation W_e = nD. The data suggests that for wider structures it needs to be slightly larger than the commensurate size to accommodate both the variation in sphere size (1.3%) and aligned movement as the fcc phase forms. With respect to this,

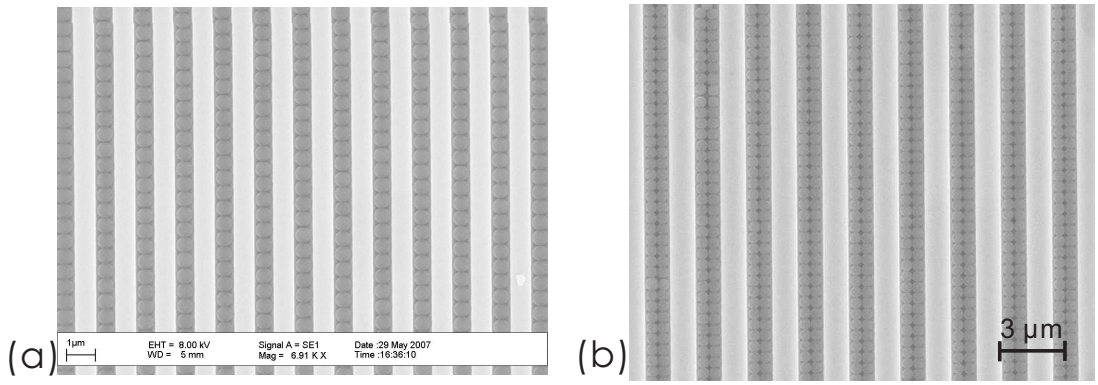

Figure 6.11: SEM images of 3D (100) oriented lattices that were assembled from 500 nm colloidal spheres in trenches of (a) 600, (b) 1200 nm nominal width.

it is also worth noting that the latex spheres do not assemble on SiO_2 surfaces in the vicinity of the Si trenches. On un-patterned planar Si or SiO_2 surfaces, latex spheres assemble into a close packed array driven by strong lateral capillary forces, which develop at the meniscus between the solution and substrate and between adjacent spheres, as illustrated in Figure 6.12(a). In contrast, as illustrated in Figure 6.12(b), on the patterned Si wafer, the mechanism of self-assembly is altered as competing surface energies play a role. The buffered hydrogen fluoride dip used on the Si surface before self assembly leaves the surface H- terminated, and thus hydrophobic. Hence it is expected that the SiO_2 has a smaller contact angle and higher surface energy than the Si surface. The liquid wets the SiO_2 better thus retracting from the Si trenches first and is only retained in the vicinity of the polystyrene spheres which are lifted up to the rim edge and brought into contact with the previously deposited spheres. The combination of maximising (a) the electrostatic attraction between the spheres and the Si trench sidewalls, and (b) the capillary forces developed by the different wetting of trench and rim appears to guarantee dense ordered packing in this system.

6.5 Optical Characteristics of patterned and self-assembled structures

Un-patterned Si wafers appear dark grey in dark field microscopy. The intrinsic colouration of our wafers is due to the micro patterning of the surface, shown in

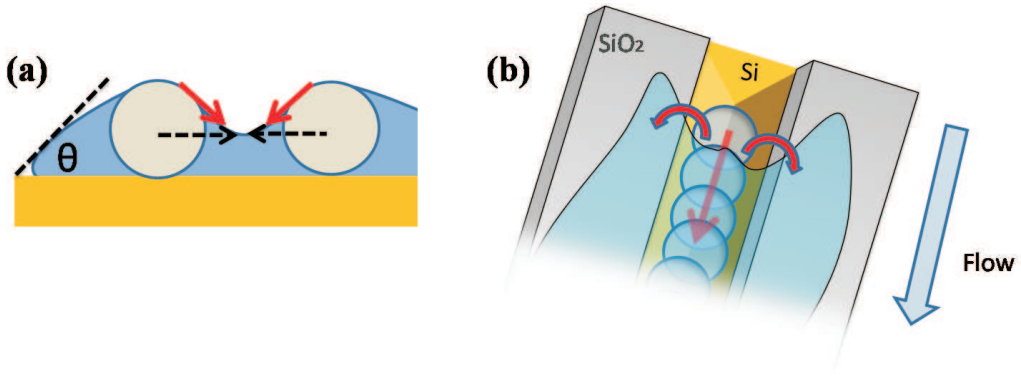

Figure 6.12: (a) On unpatterned flat Si or SiO_2 surface, strong capillary forces which develop at the meniscus between the solution and substrate and between adjacent spheres assemble the spheres into a hexagonal close-packed array. θ is the contact angle of substrate. (b) On the patterned Si wafer, the liquid wets the SiO_2 better thus retracting from the Si trenches first.

Figure 6.13. Periodic patterning of the Si surface at the sub-micron scale results in optical diffraction. Trenches of widths from 500 nm to 1200 nm were imaged in dark field configuration, shown in Figure 6.13(a). In dark field imaging, only scattered (i.e. here diffracted) light is collected by the objective, shown schematically in Figure 6.13(c). A simple calculation of the peak diffracted wavelengths as a function of trench pitch shows excellent agreement with the microscope image colours (Figure 6.13(d)), providing a rapid method to verify the trench pitch and substrate uniformity at precise locations. Figure 6.13(b) shows the same substrate with spheres placed in the trenches. The spheres modify the local refractive index, tuning the effective pitch of the trenches, and hence tuning their colour. From the uniformity of sample colour, sphere packing density can be inferred, as shown in Figure 6.13(e). Well ordered samples with good adhesion to the patterned substrate appear opalescent.

6.6 Metallisation through colloidal sphere template

After self-assembly, the 3D lattices are used as templates to fabricate gold nanoscale void trench arrays on Si by electrodeposition. A pulse of -1.1 V vs. SCE (see Experimental Section) for 0.2 s is used to form a layer of uniform Au nucleation. With semiconductor Si as the electrodeposition interface, instantaneous uniform nucleation is crucial to obtain a continuous gold film[38, 30]. A potential of -0.7 V vs. SCE was

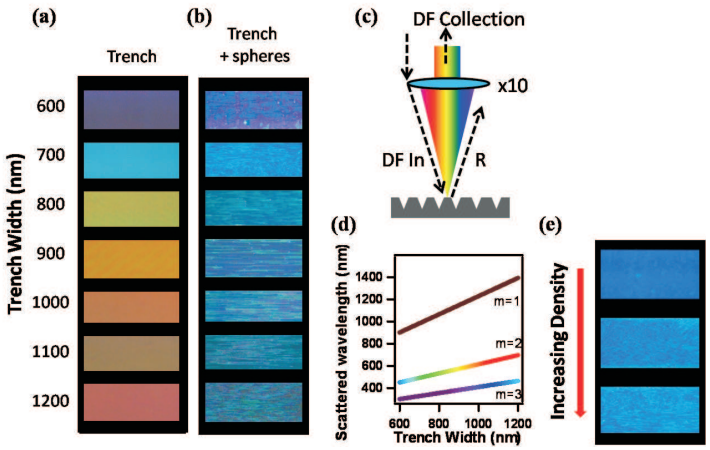

Figure 6.13: Dark field microscope images of (a) bare trench arrays from 600 nm to 1200 nm width and with fixed spacing between trenches of 500 nm, (b) with self assembled latex sphere templates. Colour changes across each sample are due to changes in the local refractive index, which is directly related to the sphere packing density and uniformity. (c) Schematic of light collection by microscope in dark field configuration. (d) Calculated diffracted wavelengths for the three lowest diffraction orders as a function of trench width. m is the diffraction order. (e) Sphere packing density can be inferred from each image. Images (b) and (e) were taken by Prof. Jeremy Baumberg and (c) and (d) were drawn by Robin Cole.

selected to allow the gradual electrodeposition of Au without any further nucleation. As shown in Fig. 6.14, using 500 nm diameter colloidal spheres a single dot chain of gold inverse spherical nanovoids are grown in the 800 nm trenches, whilst double dot chains are grown in 1500 nm trenches. Gold electrodeposition occurs only on the Si surface but not on the top insulating SiO_2, resulting in confinement of the metal arrays exclusively to the Si trenches. Illustrated in Fig. 6.15, gold growth begins from both walls of v-shaped trenches, where the orientation of Si is (111). Due to the trench geometry, gold growth is most rapid at the bottom apex of the trench. Compared with nanovoids grown on a flat substrate, the structure of the Au grown into v-shaped groove trenches is of a more complicated nature. The volume of the gold deposited is estimated from the charge passed during electrodeposition and is well controlled. A range of structures from shallow dishes, to triangular islands and truncated spherical cavities can be fabricated depending on the volume of Au deposited. For a given electrodeposition volume, the void shapes in the v-shaped trenches form deeper cavities than those on flat bottom trenches.

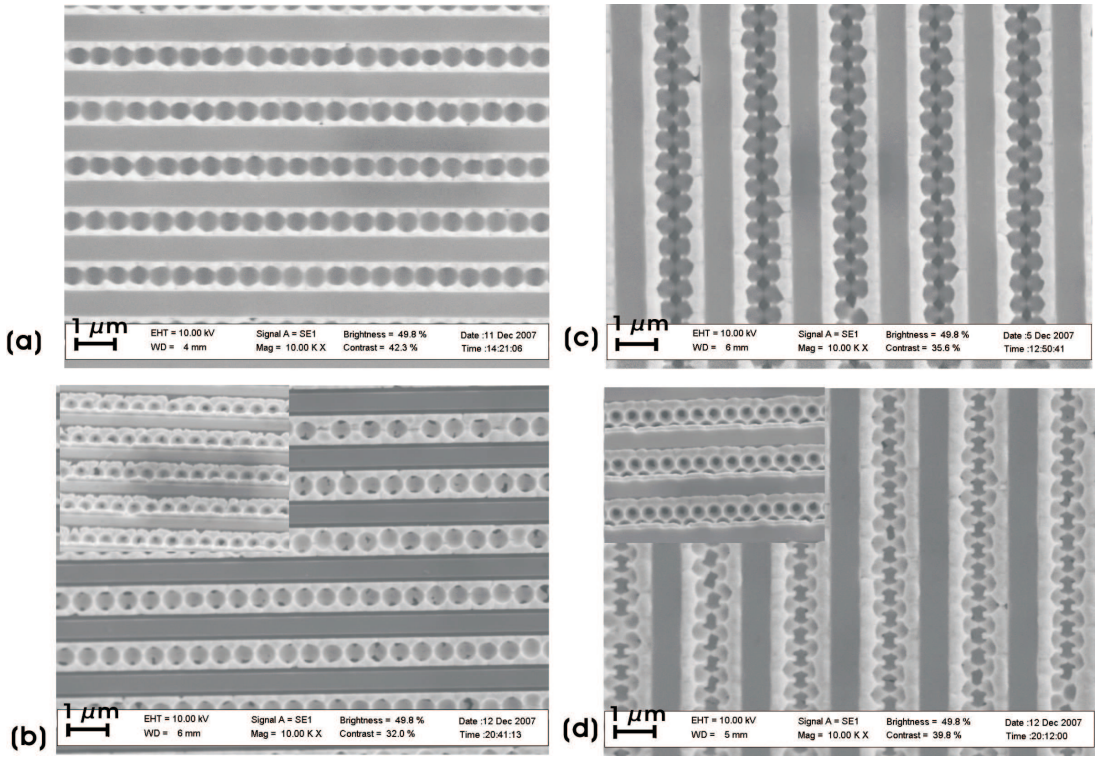

Figure 6.14: SEM images of single and double gold nanovoid chains arrays. The nanovoids are grown along the 3D template that was assembled from 500 nm colloidal spheres in arrays of trenches with 800 nm (a,b) and 1500 nm (c,d) in nominal width, respectively. (a,c) With sphere template intact. (b,d) with spheres removed. Inset: the view at 45° angle tilted.

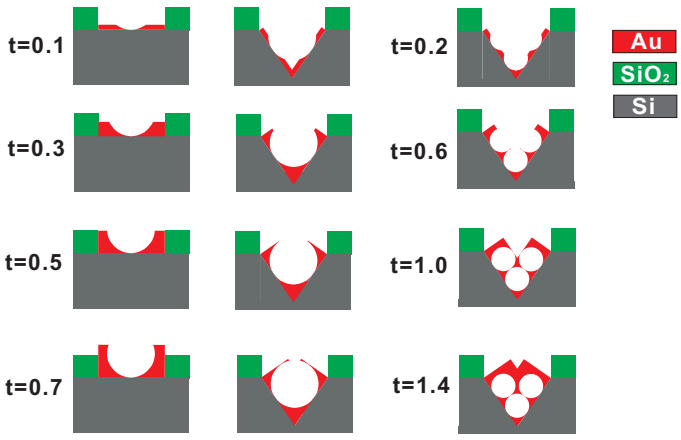

Figure 6.15: Schematics of the cross section of gold inverse spherical nanovoids with different thickness. In the left two columns, comparison of the single dot chain mode grown on a flat bottom trench and a v-groove one. t is the ratio of film thickness to sphere diameter. In the right column, the double dot chains mode grown on v-groove trench.

6.7 Optical Characteristics of Gold Nanovoids

Angle-dependent optical characterisation of these structures reveals a rich variety of optical and plasmonic modes, which are strongly dependent on the lattice structure and Au thickness. Dispersion analysis reveals the nature of the observed plasmon modes, as illustrated in Fig.6.1.

A fibre-coupled spectrometer (Ocean Optics, spectral range 400-1700 nm, resolution 1 nm) placed in the focal plane of the reflection image was used to obtain the spectral response from the selected area (approximate diameter 50 μm). Optical reflectivity measurements in TM polarization for two different samples are shown in Fig.6.16. The samples were illuminated with visible light from 400 nm to 1700 nm, and incident scan angles from 0° to 80°. The thickness ratio t/D is 0.5, corresponding to a semi-truncated spherical cavity. First we identify weak but highly dispersive (i.e. strongly angle dependent) modes which correspond to propagating plasmon modes, where the plasmon frequency depends on the incident photon wave vector. The dispersion of these modes corresponds to plasmons propagating along the length of the trenches. The data also reveals highly localised modes, which due to their confined nature, have a well defined plasmon frequency. These modes are characterised by a very flat dispersion, and are predominant in high aspect ratio nanoscale void structures.

Hopping of localized plasmons between neighbouring spheres can be identified from the presence of 'nearly' localised plasmons with mixed Bragg-Mie dispersion. Whereas light incident on a 2D hexagonal nanoscale void array can couple to plasmon modes at any incident azimuthal angle to the crystal lattice, in the trench structures only light incident parallel to the trenches will couple strongly to plasmon modes, with only weak coupling to localised plasmons by light incident perpendicular to the trenches. This highlights the crucial role of the trenches in guiding and confining the propagating plasmons. Initial analyses shows that both localized modes and dispersive modes are better defined with the colloidal spheres left in place (providing a high refractive core which confines the plasmons better). It can also be seen that the localized plasmon present in the single layer structure shifts to higher energy when the spheres are removed. This is a direct consequence of the lower dielectric constant of the air as compared to the colloidal spheres, as described in detail in Ref.[143].

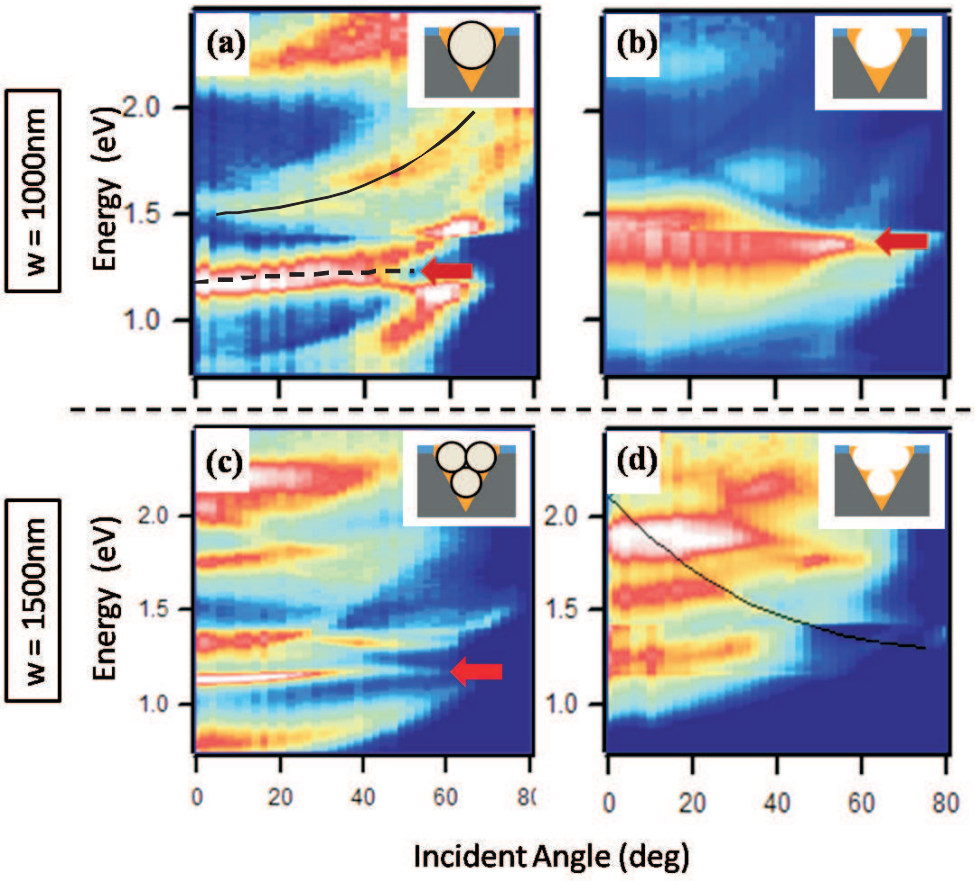

Figure 6.16: Dispersion plots, red corresponds to absorption: (a) 1000 nm in a nominal width trench containing 500 nm diameter spheres in Au. The arrow identifies the localized plasmon. (b) with spheres removed, the localized plasmon shifts to higher energy. (c) double layer spheres in an Au structure in a 1500 nm nominal width trench, arrow indicates mixed Bragg-Mie mode which 'hops' between neighbouring sphere. (d) with spheres removed, black line indicates theoretical dispersion of a plasmon propagating along a 1D chain of voids, modeled using the Bragg scattering equation. Flat dispersions are indicative of localised plasmon modes. The theoretical dispersion line was calculated by Robin Cole.

6.8 Conclusions

We have demonstrated a method to fabricate gold nanovoid trench arrays. In this method photolithography is used to pre-pattern a Si surface, which is then selectively etched in KOH to create a series of v-shape groove trenches. The geometric confinement of the trenches, together with electrostatic interactions and surface tension, guides the (110) fcc assembly of the spheres on this patterned Si surface. Zero-defect arrays were found to assemble along the entire length of some trenches, leading to state of the art defect-free areas of $0.5 \times 0.2\ mm^2$ (this is the full range of a certain size trench.) for 500 nm diameter spheres, allowing characterisation with visible light. The array formation was found to be highly dependent on the width of the trenches. Various array formations, including single dot chains, fcc, and helical chains, were achieved by modifying the trench width. Currently there is no microscopic explanation for the formation of stable repeating spiral chains which are of great interest for their chiral behaviour. These long-range well-ordered sphere strip arrays are used as templates to form gold nanoscale void strip arrays by electrodeposition. By varying the film thickness, void shapes ranging from shallow dishes to encapsulated voids were fabricated. The gold strip arrays are of high quality with respect to lateral symmetry and allow the detection of plasmonic signals. Further understanding of the different plasmon modes will aid research into slow-light and active waveguides, and potentially allow on-chip optical communication.

Chapter 7

Summary

Practical applications of electronics and nanotechnology depend largely on their compatibility with conventional microelectronics technology and hence on their integration with semiconductors. In this thesis, metal electrodeposition on semiconductor substrates is investigated. We show that electrodeposition of metals on n-type Si and Ge is an excellent method to create Schottky barriers and that this method has a number of unique advantages over other (physical) deposition methods and that these advantages can be used to improve the prospects of applications in the area of Spintronics and Plasmonics.

Firstly, the low reverse bias leakage of the Schottky diodes allows the use of highly doped Schottky barriers in which all reverse bias current is due to tunneling. Hence, for magnetic metals, these Schottky barriers allow spin-conserved conduction which is a necessary step towards semiconductor spin valves and spin transistors. Secondly, electrodeposition is not a line-of-sight-technique and can hence be used to grow three dimensional structures when an appropriate pattern is created. Photonic crystals are created by using electrodeposition of gold around a latex sphere pattern nanovoid array.

In Chapter 2, the principle of electrodeposition of metals on semiconductors are outlined and the experimental details, which includes the equipment setup and the recipes of different metal electrodeposition solutions, are discussed. The results reveal that each metal semiconductor combination requires a series of distinct system parameters. For Au or Ni on Si, chronoamperometry with nucleation pulse is suitable.

For Co on Si, chronopotentiometry with pulse pretreatment is the proper method. For Ni on Ge, either chronopotentiometry or chronoamperometry can be used and a nucleation pulse is not essential.

In Chapter 3, the principles of Schottky barriers and its electrical characteristics are discussed. Experimental results of current-voltage and capacitance-voltage Ni-Si Schottky barriers are presented, and analysis of thermionic and thermionic field emission as a function of temperature is discussed. This demonstrates that electrodeposited Ni-Si Schottky barriers have excellent rectifying behaviour, which might make them ideally suitable for spintronic devices. A number of additional experiments is presented on electrodeposition in a magnetic field, electrodeposition of Co on Si, and a comparison with evaporated diodes is made.

In Chapter 4, a review of Spintronics is given. In the study of vertical spin valves, our experimental results clearly show an electrically well functioning back to back diode can be fabricated using the membrane technique and further experiments can build upon these results though no MR signal was observed at present. In the study of lateral spin valves, Ni/Ge Schottky barriers formed by electrodeposition on highly doped substrate shows high rectification with low leakage current in reverse bias. The fabricated Ni/Ge diodes transformed into NiGe/Ge diodes upon annealing at 500 °C. Despite the compositional change the Schottky barrier properties were virtually unaltered due to Fermi level pinning. The series resistances of NiGe decreased with annealing temperature which is important for high drive current in Schottky barrier-MOSFETs.

In Chapter 5, self-assemblies are reviewed and the fabrication process of self-assembled latex spheres is shown. The results reveal that by tailoring the dimensions of the guiding patterns, either perfect, or triangularly distorted, close packed self-assembly symmetry is possible. These patterns are successfully transferred to Ni nanovoid arrays by electrodeposition. The anisotropic magnetoresistance of these Ni nanovoid arrays is 0.85%, which exceeds values obtained from similar structures, due to the unique 3D geometry of the arrays.

In Chapter 6, a method to fabricate gold nanovoid trench arrays using self assembly into v-grooves and electrodeposition is demonstrated. Various array formations, including single dot chains, face-centered cubic, and helical chains, were achieved by

modifying the trench width. These long-range well-ordered sphere strip arrays are used as templates to form gold nanoscale void strip arrays by electrodeposition. By varying the gold thickness, void shapes ranging from shallow dishes to encapsulated voids were fabricated with high quality with respect to lateral symmetry. Plasmonic signals corresponding to localized modes are detected from these guided self assembled structures.

Bibliography

[1] *Electroplating*, http://en.wikipedia.org/wiki/Electroplating, June 2005. Wikipedia, the free encyclopedia.

[2] G. Oskam, J. G. Long, A. Natarajan, and P. C. Searson. Electrochemical deposition of metals onto silicon. *Journal of Physics D: Applied Physics*, 31(16):1927–1949, 1998.

[3] C. Ji, G. Oskam, and P. C. Searson. Electrodeposition of copper on siliconfrom sulfate solution. *Journal of The Electrochemical Society*, 148(11):C746–C752, 2001.

[4] D. J. Monsma, J. C. Lodder, Th. J. A. Popma, and B. Dieny. Perpendicular hot electron spin-valve effect in a new magnetic field sensor: The spin-valve transistor. *Physical Review Letters*, 74(26):5260, 1995.

[5] M. Schlesinger and M. Paunovic, editors. *Modern electroplating 4th ed.* Wiley, New York, 2000.

[6] M. Paunovic and M. Schlesinger. *Fundamentals of electrochemical deposition.* John Wiley & Sons, INC., 1998.

[7] Southampton Electrochemistry Group, editor. *Instrumental Methods in Electrochemistry.* Ellis Horwood Limited, 1985.

[8] F. A. Lowenheim. *Modern electroplating.* Wiley, New York, 1974.

[9] M. E. Kiziroglou, X. Li, D. C. Gonzalez, C. H. de Groot, A. A. Zhukov, P. A. J. de Groot, and P. N. Bartlett. Orientation and symmetry control of inverse sphere magnetic nanoarrays by guided self-assembly. *Journal of Applied Physics*, 100:113720–113725, 2006.

[10] E. Budevski, G. Staikov, and W.J. Lorenz. *Electrochemical Phase Formation and Growth.* VCH Publishers, 1996.

[11] Southampton Electrochemistry Group. Instrumental methods in electrochemistry-southampton electrochemistry summer school notes. Technical report, University of Southampton, 2004.

[12] M. Schlesinger. *Electrochemistry Encyclopedia*, chapter Electroplating. Ernest B. Yeager Center for Electrochemical Sciences (YCES) and the Chemical Engineering Department, Case Western Reserve University , Cleveland, Ohio, 2002.

[13] O. J. Kwon, S. H. Cha, and J. J. Kim. Ruthenium bottom electrode prepared by electroplating for a high density dram capacitor. *Journal of The Electrochemical Society*, 151(2):C127–C132, 2004.

[14] C. Gabrielli, G. Maurin, G. Poindessous, and R. Rosset. Nucleation and growth of calcium carbonate by an electrochemical scaling process. *Journal of Crystal Growth*, 200(1-2):236, 1999.

[15] E. J. Tull, P. N. Bartlett, and K. R. Ryan. Controlled assembly of micrometer-sized spheres: Theory and application. *Langmuir*, 14:7859–7873, 2007.

[16] M. S. Wrighton. Surface functionalization of electrodes with molecular reagents. *Science*, 231:32, 1986.

[17] R. G. Freeman, K. C. Grabar, K. J. Allison, R. M. Bright, J. A. Davis, A. P. Guthrie, M. B. Hommer, M. A. Jackson, P. C. Smith, D. G. Walter, and M. J. Natan. Self-assembled metal colloid monolayers: An approach to sers substrates. *Science*, 267(5204):1629–1632, 1995.

[18] S. M. Sze. *Physics of Semiconductor Devices 2nd Edition.* John Wiley & Sons, INC, 1981.

[19] S. M. Sze. *Semiconductor Devices: Physics and Technology 2nd Edition.* John Wiley & Sons, INC, 2001.

[20] E. H. Rhoderick. Transport processes in schottky diodes. In *Conference on metal-semiconductor contacts*, Manchester, Lancs., UK, April 1974. Institute of Physics.

[21] A. Y. C. Yu and E. H. Snow. Surface effects on metal-silicon contacts. *Journal of Applied Physics*, 39(7):3008 – 3016, 1968.

[22] V. L. Rideout. A review of the theory, technology and applications of metal-semiconductor rectifiers. *Thin Solid Films*, 48(3):261, 1978.

[23] E. H.(Emlyn Huw) Rhoderick and R. H. Williams. *Metal-semiconductor contacts 2nd Edition.* Clarendon, Oxford, 1988.

[24] W. F. Beadle. *Quick Reference manual for Semicondutor Engineer.* Wiley, New York, 1985.

[25] F.M. Smits. Measurement of sheet resistivities with the four-point probe. *Jounal of Bell System Technology*, 37:711, 1958.

[26] L. J. van der Pauw. A method of measuring specific resistivity and hall effect on disc or arbitary shape. *Philips Research Reports*, 13:1, 1958.

[27] J. H. Werner and H. H. Guttler. Barrier inhomogeneities at Schottky contacts. *Journal of Applied Physics*, 69(3):1522–1533, 1991.

[28] R. T. Tung. Electron transport at metal-semiconductor interfaces: General theory. *Physical Review B*, 45(23):13509–13523, 1992.

[29] A. N. Saxena. Forward current-voltage characteristics of Schottky barriers on n-type silicon. *Journal of Surface Science*, 13:151–171, 1969.

[30] M. E. Kiziroglou, A. A. Zhukov, X. Li, D. C. Gonzalez, P. N. de Groot, P. A. J.and Bartlett, and C. H. de Groot. Analysis of thermionic emission from electrodeposited NiSi Schottky barriers. *Solid State Communications*, 140:508–513, 2006.

[31] M. E. Kiziroglou, X. Li, A. A. Zhukov, P. A. J. de Groot, and C. H. de Groot. Thermionic field emission at electrodeposited Ni-Si Schottky barriers. *Solid-State Electronics*, 52(7):1032–1038, 2008.

[32] J. H. Werner and H. H. Guttler. Barrier inhomogeneities at schottky contacts. *JAP*, 69(3):1522–1533, 1991.

[33] F.A. Padovani and R. Stratton. Field and thermionic-field emission in Schottky barriers. *Solid-State Electron*, 9:69, 1966.

[34] S. H. Songa J. G. Kima, K. H. Han and A. Reillyb. Magnetic properties of sputtered soft magnetic FeNi films with an uniaxial anisotropy. *Thin Solid Films*, 440:54–59, 2003.

[35] Z. Popovic and B. D. Popovic. *Introductory electromagnetics*. Prentice Hall, 1999.

[36] B. H. Hwang. Calculation and measurement of all (002) multiple diffraction peaks from a (001) silicon wafer. *Journal of Physics D: Applied Physics*, 34:2469–2474, 2001.

[37] B. D. Cullity. *Elements of X-Ray Diffraction*. Addison-Wesley Publishing Company, INC., 1967.

[38] M. E. Kiziroglou, A. A. Zhukov, M. Abdelsalam, X. Li, P. A. J. de Groot, P. N. Bartlett, and C. H. de Groot. Electrodeposition of Ni-Si Schottky barriers. *IEEE Transactions on Magnetics*, 41:2639–2641, 2005.

[39] G. Schmidt. Concepts for spin injection into semiconductors - A review. *Journal of Physics D: Applied Physics*, 38:R107–R122, 2005.

[40] G. Schmidt and L. W. Molenkamp. Spin injection into semiconductors, physics and experiments. *Semiconductor Science and Technology*, 17:310–321, 2002.

[41] T. McGuire and R. Potter. Anisotropic magnetoresistance in ferromagnetic 3D alloys. *IEEE Transactions on Magnetics*, 11:1018–1038, 1975.

[42] M. N. Baibich, J. M. Broto, and Fert A. Giant magnetoresistance of (001)Fe/(001)Cr magnetic superlattices. *Physical Review Letters*, 61:2472–2475, 1988.

[43] G. Binasch, P. Grünberg, F. Saurenbach, and W. Zinn. Enhanced magnetoresistance in layered magnetic structures with antiferromagnetic interlayer exchange. *Physical Review B*, 39(7):4828–4830, Mar 1989.

[44] J. S. Moodera and L. R. Kinder. Large magnetoresistance at room temperature in ferromagnetic thin film tunnel junctions. *Physical Review Letters*, 74:3272–3276, 1995.

[45] P. Bruno. Geometrically constrained magnetic wall. *Physical Review Letters*, 83(12):2425–2428, 1999.

[46] K. Mizushima, T. Kinno, T. Yamauchi, and K. Tanaka. Energy-dependent hot electron transport across a spin-valve. *IEEE Transactions on Magnetics*, 33(5):3500, 1997.

[47] S. Datta and B. Das. Electronic analog of the electro-optic modulator. *Applied Physics Letters*, 56(7):665–667, 1990.

[48] P. A. E. Jonkers. *Quantum transport in disordered magnetoresistive systems*. PhD thesis, University of Groningen, Netherlands, 2000.

[49] J. F. Gregg, I. Petej, E. Jouguelet, and C. Dennis. Spin electronics: A review. *Journal of Physics D: Applied Physics*, 35(18):R121–R155, 2002.

[50] S. S. P. Parkin, C. Kaiser, A. Panchula, P. M. Rice, B. Hughes, M. Samant, and S. H. Yang. Giant tunnelling magnetoresistance at room temperature with MgO (100) tunnel barriers. *Nature Materials*, 3:862–867, 2004.

[51] P. M. Levy and S. Zhang. Resistivity due to domain wall scattering. *Physical Review Letters*, 79:5110–5113, 1997.

[52] J. F. Gregg, W. Allen, K. Ounadjela, M. Viret, M. Hehn, S. M. Thompson, and J. M. D. Coey. Giant magnetoresistive effects in a single element magnetic thin film. *Physical Review Letters*, 77(8):1580–1583, 1996.

[53] J. F. Gregg, R. P. Borges, E. Jouguelet, C. L. Dennis, I. Petej, S. M. Thompson, and K. Ounadjela. Spin injection efficiency in spin electronic devices. *Journal of Magnetism and Magnetic Materials*, 265(3):274, 2003.

[54] G. Schmidt, D. Ferrand, L. W. Molenkamp, A. T. Filip, and B. J. van Wees. Fundamental obstacle for electrical spin injection from a ferromagnetic metal into a diffusive semiconductor. *Physical Review B*, 62(8):R4790–R4793, Aug 2000.

[55] A. M. Bratkovsky and V. V. Osipov. Efficient spin injection and extraction in modified reverse and forward biased ferromagnetic-semiconductor junctions and low-power ultrafast spin injection devices. *Applied Physics A: Materials Science & Processing*, 80(6):1237–1246, 2005.

[56] Mark Johnson. Bilayer embodiment of the bipolar spin switch. *Applied Physics Letters*, 63(10):1435–1437, 1993.

[57] M. Johnson. Bipolar spin switch. *Science*, 260(5106):320–323, April 1993.

[58] M. Johnson. Spin injection in metal films: The bipolar spin transistor. *Materials Science and Engineering B*, 31(1-2):199, 1995.

[59] C. L. Dennis, C. Sirisathitkul, G. J. Ensell, J. F. Gregg, and S. M. Thompson. High current gain silicon-based spin transistor. *Journal of Physics D: Applied Physics*, 36(2):81–87, 2003.

[60] R. Jansen, O. M. J. van't Erve, S. D. Kim, R. Vlutters, P. S. Anil Kumar, and J. C. Lodder. The spin-valve transistor: Fabrication, characterization, and physics. *Journal of Physics D: Applied Physics*, 89(11):7431–7436, 2001.

[61] P. S. Anil Kumar, R. Jansen, O. M. J. van 't Erve, R. Vlutters, P. de Haan, and J. C. Lodder. Low-field magnetocurrent above 200room temperature. *Journal of Magnetism and Magnetic Materials*, 214(1-2):1, 2000.

[62] R. Jansen, P. S. Anil Kumar, and J. C. Lodder. Thermal spin-wave scattering in hot-electron magnetotransport across a spin valve. *Physical Review Letters*, 85:3277–3280, 2000.

[63] R. Jansen. The spin-valve transistor: A review and outlook. *Journal of Physics D: Applied Physics*, 36(19):R289–R308, 2003.

[64] T. Shimatsu, R. H. Mollema, D. Monsma, E. G. Keim, and J. C. Lodder. Metal bonding during sputter film deposition. *Journal of Vacuum Science & Technology A: Vacuum, Surfaces, and Films*, 16(4):2125–2131, 1998.

[65] J. C. Lodder, D. J. Monsma, R. Vlutters, and T. Shimatsu. The spin-valve transistor: technologies and progress. *Journal of Magnetism and Magnetic Materials*, 198-199:119, 1999.

[66] K. Mizushima, T. Kinno, K. Tanaka, and T. Yamauchi. Strong increase of the effective polarization of the tunnel current in $Fe/AlO_x/Al$ junctions with decreasing Fe layer thickness. *Physical Review B*, 58:4660–4665, 1998.

[67] X. Lou, C. Adelmann, S. A. Crooker, E. S. Garlid, J. Zhang, K. S. Madhukar Reddy, S. D. Flexner, C. J. Palmstr, and P. A. Crowell. Electrical detection of spin transport in lateral ferromagnetsemiconductor devices. *Nature Physics*, 3:197–202, 2007.

[68] B. T. Jonker, G. Kioseoglou, A. T. Hanbicki, C. H. Li, and P. E. Thompson. Electrical spin-injection into silicon from a ferromagnetic metal/tunnel barrier contact. *Nature Physics*, 3:542–546, 2007.

[69] O. M. J. van't Erve, A. T. Hanbicki, M. Holub, C. H. Li, C. Awo-Affouda, P. E. Thompson, and B. T. Jonker. Electrical injection and detection of spin-polarized carriers in silicon in a lateral transport geometry. *Applied Physics Letters*, 91(21):212109, 2007.

[70] M. Hu, J. Chen, Z. Li, L. Au, G. V. Hartland, X. Li, M. Marquez, and Y. Xia. Gold nanostructures: engineering their plasmonic properties for biomedical applications. *Chemical Society Reviews*, 35:1084–1094, 2006.

[71] B. Min, K. Motohashi, C. Lodder, and R. Jansen. Tunable spin-tunnel contacts to silicon using low-work-function ferromagnets. *Nature Materials*, 5(10):817–822, 2006.

[72] R. Levin C. Koeneke, S. Sze and E. Kinsbron. Schottky MOSFET for VLSI. *International Electron Devices Meeting (IEDM)Tech. Dig.*, 27:367–370, 1981.

[73] R. Li, S. Lee, H. Yao, D. Chi, M. Yu, and D.-L. Kwongvol. Pt-germanide Schottky source/drain germanium p-MOSFET with HfO_2 gate dielectric and TaN gate electrode. *IEEE Electron Device Letters*, 27:476–478, 2006.

[74] J. M. Larson and J. P. Snyder. Overview and status of metal S/D Schottky-barrier MOSFET technology. *IEEE Transactions on Electron Devices*, 53:1048, 2006.

[75] S. Zhu, R. Li, S. Lee, M. Li, A. Du, J. Singh, C. Zhu, A. Chin, and D. Kwong. Germanium p-MOSFETs with Schottky-barrier germanide S/D, high-k gate dielectric and metal gate. *IEEE Electron Device Letter*, 26:81–83, 2005.

[76] V. W. L. Chin, J. W. V. Storey, and M. A. Green. P-type PtSi Schottky diode barrier height determined from I-V measurement. *Solid State Electronics*, 32(6):475–478, 1989.

[77] E. Chan and H. Card. Optoelectronic properties of metal-Ge Schottky barrier quantum detectors. *International Electron Devices Meeting (IEDM)Tech. Dig.*, 24:653–656, 1978.

[78] J. Seger, S.-L. Zhang, D. Mangelinck, and H. H. Radamson. Increased nucleation temperature of $NiSi_2$ in the reaction of Ni thin films with $Si_{1-x}Ge_x$. *Applied Physics Letters*, 81(11):1978–1980, 2002.

[79] J. Y. Spann, R. A. Anderson, T. J. Thornton, G. Harris, S. G. Thomas, and C. Tracy. Characterization of nickel germanide thin films for use as contacts to p-channel germanium MOSFETs. *Electron Device Letters, IEEE*, 26(3):151–153, March 2005.

[80] M. K. Husain, X. Li, and C. H. De Groot. High quality schottky contacts for limiting leakage currents in Ge based Schottky barrier MOSFETs. *IEEE Transactions on Electron Devices*, 56(3):499–504, 2009.

[81] G. M. Whitesides and B. Grzybowski. Self-assembly at all scales. *Science*, 295:2418–2421, 2002.

[82] P. N. Bartlett, P. N. Birkin, M. A. Ghanem, P. de Groot, and M. Sawicki. The electrochemical deposition of nanostructured cobalt films from lyotropic liquid crystalline media. *Jounal of Bell System Technology*, 148:C119–C123, 2001.

[83] J. C. Hulteen and C. R. Martin. A general template-based method for the preparation of nanomaterials. *Journal of Materials Chemistry*, 7(7):1075–1087, 1997.

[84] T. Thurn-Albrecht, J. Schotter, G. A. Kastle, N. Emley, T. Shibauchi, L. Krusin-Elbaum, K. Guarini, C. T. Black, M. T. Tuominen, and T. P. Russell. Ultrahigh-density nanowire arrays grown in self-assembled diblock copolymer templates. *Science*, 290:2126–2129, 2000.

[85] P. N. Bartlett, P. R. Birkin, and M. A. Ghanem. Electrochemical deposition of macroporous platinum, palladium and cobalt films using polystyrene latex sphere templates. *Chemical Communications*, 21(17):1671–1672, 2000.

[86] L. Xu, W. L. Zhou, C. Frommen, R. H. Baughman, A. A. Zakhidov, L. Malkinski, J. Q. Wang, and J. B. Wiley. Electrodeposited nickel and gold nanoscale metal meshes with potentially interesting photonic properties. *Chem. Commun.*, pages 997–998, 2000.

[87] J. Cheng, C. A. Ross, and A. Mayes. Nanostructure engineering by templated self-assembly. *Nature Materials*, 3(11):823–828, 2004.

[88] S. M. Yang and G. A. Ozin. Opal chips: vectorial growth of colloidal crystal patterns inside silicon wafers. *Chemical Communications*, pages 2507–2508, 2000.

[89] D. Wang and H. Mohwald. Template-directed colloidal self-assembly the route to top-down nanochemical engineering. *Jounal of Materials Chemistry*, 14:459–468, 2004.

[90] P. Ferrand, M. Egen, B. Griesebock, J. Ahopelto, M. Muller, R. Zentel, S. G. Romanov, and C. M. Sotomayor. Self-assembly of three-dimensional photonic

crystals on structured silicon wafers. *Applied Physics Letters*, 81(15):2689–2691, 2002.

[91] J. P. Hoogenboom, C. Retif, E. de Bres, M. van de Boer, A. K. van Langen-Suurling, J. Romijn, and A. van Blaaderen. Template-induced growth of close-packed and non-close-packed colloidal crystals during solvent evaporation. *Nano Letters*, 4(2):205–208, 2004.

[92] Y. H. Ye, S. Badilescu, V. V. Truong, P. Rochon, and A. Natansohn. Self-assembly of colloidal spheres on patterned substrates. *Appl. Phys. Lett.*, 79(6):872–874, 2001.

[93] J. Zhang, A. Alsayed, K. H. Lin, S. Sanyal, F. Zhang, W.J. Pao, V. S. K. Balagurusamy, P. A. Heiney, and A. G. Yodha. Template-directed convective assembly of three-dimensional face-centered cubic colloidal crystals. *Applied Physics Letters*, 81(17):3176–3178, 2001.

[94] J. I. Martin, J. Nogues, Kai Liu, J. L. Vicent, and Ivan K. Schuller. Ordered magnetic nanostructures: fabrication and properties. *Journal of Magnetism and Magnetic Materials*, 256:449–501, 2003.

[95] M. Brust and C. J. Kiely. Some recent advances in nanostructure preparation from gold and silver particles: a short topical review. *Colloids and Surfaces A: Physicochemical and Engineering Aspects*, 202(2-3):175, 2002.

[96] A. M. Mayes J. Y. Cheng and C. A. Ross. Nanostructure engineering by templated self-assembly of block copolymers. *Nature Materials*, 3:823–828, 2001.

[97] D. Philp and J. F. Stoddart. Self-assembly in natural and unnatural systems. *Angewandte Chemie-International Edition in English*, 35(11):1155–1196, 1996.

[98] P. Ball. The self-made tapestry: Pattern formation in nature. *Oxford Univ. Press*, 1999.

[99] G. M. Whitesides and B. Grzybowski. Self-assembly at all scales. *Science*, 295(5564):2418–2421, 2002.

[100] J. C. Huie. Guided molecular self-assembly: a review of recent efforts. *Smart Materials and Structures*, 12(2):264–271, 2003.

[101] J. H. Fendler. Chemical self-assembly for electronic applications. *Chemistry of Materials*, 13(10):3196–3210, 2001.

[102] K. B. Blodgett and I. Langmuir. Built-up films of Barium Stearate and their optical properties. *Physical Review*, 51:964–982, 1937.

[103] J. Cha, Y.-K. See, J. Lee, and T. Chang. Structure and thermal stability of cadmium arachidate/poly(tert-butyl methacrylate) alternating Langmuir-Blodgett film. *Synthetic Metals*, 117(1-3):149, 2001.

[104] R. I. Carey, J. P. Folkers, and G. M. Whitesides. Self-assembled monolayers containing w-Mercaptoalkyl boronic acids adsorbed onto gold form a highly cross-linked, thermally stable borate glass surface. *Langmuir*, 10(7):2228–2234, 1994.

[105] A. Ulman. Formation and structure of self-assembled monolayers. *Chemical Reviews*, 96(4):1533 – 1554, 1996.

[106] P. A. Kralchevsky and N. D. Denkov. Capillary forces and structuring in layers of colloid particles. *Current Opinion in Colloid & Interface Science*, 6:383–401, 2001.

[107] N. D. Denkov, O. D. Velev, P. A. Kralchevsky, I. B. Ivanov, J. H. Yoshimura, and K. Nagayama. Mechanism of formation of two-dimensional crystals from latex particles on substrates. *Langmuir*, 8:3183–3190, 1992.

[108] N. D. Denkov, P. A. Velev, O. D.and Kralchevsky, I. B. Ivanov, H. Yoshimura, and K. Nagayama. Two-dimensional crystallization. *Nature*, 361:26, 1993.

[109] K. Nagayama. Two-dimensional self-assembly of colloids in thin liquid films. *Colloids Surfaces A*, 109:363–374, 1996.

[110] A. S. Dimitrov and K. Nagayama. Continuous convective assembling of fine particles into two-dimensional arrays on solid surfaces. *Langmuir*, 12:1303–1311, 1996.

[111] J. C. Hulteen and R. P. van Duyne. Nanosphere lithography: a materials general fabrication process for periodic particle array surfaces. *The Journal of Vacuum Science and Technology A*, 13:1553–1558, 1995.

[112] M. Sasaki and K. Hane. Ultrasonically facilitated two-dimensional crystallization of colloid particles. *Jounal of Applied Physics*, 80:5427–5431, 1996.

[113] R. Micheletto, H. Fukuda, and M. Ohtsu. A simple method for the production of two-dimensional, ordered array of small latex particles. *Langmuir*, 11:3333–3336, 1995.

[114] G. S. Lazarov, N. D. Denkov, O. D. Velev, P. A. Kralchevsky, and K. Nagayama. Formation of two-dimensional structures from colloidal particles on fluorinated oil substrate. *Journal of the Chemical Society, Faraday Transactions*, 90:2077–2083, 1994.

[115] J. McLellan Y. Yin, Y. Lu and Y. Xia. Template-assisted self-assembly of spherical colloids into complex and controllable structures. *Advanced Functional Materials*, 13:907–918, 2003.

[116] Y. Yin, Y. Lu, B. Gates, and Y. Xia. Template-assisted self-assembly: A practical route to complex aggregates of monodispersed colloids with well-defined sizes, shapes, and structures. *Journal of the American Chemical Society*, 123:8718 – 8729, 2001.

[117] G. T. Pickett, M. Gross, and H. Okuyama. Spontaneous chirality in simple systems. *Physical Review Letters*, 85(17):3652–3655, Oct 2000.

[118] Y. Yin and Y. Xia. Self-assembly of spherical colloids into helical chains with well-controlled handedness. *Journal of the American Chemical Society*, 125:248–2049, 2003.

[119] J. H. Conway and N. J. A. Sloane. *Sphere packings, lattices and groups.* Springer-Verlag, 1988.

[120] F. J. Castano, K. Nielsch, C. A. Ross, J. W. A. Robinson, and R. Krishnan. Anisotropy and magnetotransport in ordered magnetic antidot arrays. *Applied Physics Letters*, 85(14):2872–2874, 2004.

[121] A. A. Zhukov, A. V. Goncharov, P. A. J. de Groot, M. A. Ghanem, P. N. Bartlett, R. Boardman, H. Fangohr, V. Novosad, and G. Karapetrov. Oscillatory thickness dependence of the coercive field in magnetic three-dimensional antidot arrays. *Applied Physics Letters*, 88:062511, 2006.

[122] M. Tanaka, E. Saitoh, H. Miyajima, and T. Yamaoka. Magnetization process and magnetic structure in a NiFe honeycomb nano-network. *Journal of Magnetism and Magnetic Materials*, 282:22–24, 2004.

[123] C. Bae, H. Shin, and J. Moon. Facile route to aligned one-dimensional arrays of colloidal nanoparticles. *Chemistry of Materials*, 19(7):1531–1533, 2007.

[124] J. Ye, R. Zentel, S. Arpiainen, J. Ahopelto, F. Jonsson, S. G. Romanov, and C. M. Sotomayor Torres. Integration of self-assembled three-dimensional photonic crystals onto structured silicon wafers. *Langmuir*, 22(17):7378–7383, 2006.

[125] L. N. Donselaar, A. P. Philipse, and J. Suurmond. Concentration-dependent sedimentation of dilute magnetic fluids and magnetic silica dispersions. *Langmuir*, 13(23):6018–6025, 1997.

[126] A. M. Kalsin, M. Fialkowski, M. Paszewski, S. K. Smoukov, K. J. M. Bishop, and B. A. Grzybowski. Electrostatic self-assembly of binary nanoparticle crystals with a diamond-like lattice. *Science*, 312(5772):420–424, 2006.

[127] A. van Blaaderen, R. Ruel, and P. Wiltzius. Template-directed colloidal crystallization. *Nature*, 385:321 – 324, 1997.

[128] G. A. Ozin and S. M. Yang. The race for the photonic chip: Colloidal crystal assembly in silicon wafers. *Advanced Functional Materials*, 11:95–104, 2001.

[129] Y. Yin, Z. Li, and Y. Xia. Template-directed growth of (100)-oriented colloidal crystals. *Langmuir*, 19:622 – 631, 2003.

[130] T. A. Kelf, Y. Sugawara, R. M. Cole, J. J. Baumberg, M. E. Abdelsalam, S. Cintra, S. Mahajan, A. E. Russell, and P. N. Bartlett. Localized and delocalized plasmons in metallic nanovoids. *Physical Review B (Condensed Matter and Materials Physics)*, 74(24):245415, 2006.

[131] R. M. Cole, J. J. Baumberg, F. J. GarciadeAbajo, S. Mahajan, M. Abdelsalam, and P. N. Bartlett. Understanding plasmons in nanoscale voids. *Nano Letters*, 7(7):2094–2100, 2007.

[132] R. W. Wood. On a remarkable case of uneven distribution of light in a diffraction grating spectrum. *Philosophical Magazine*, 4:396, 1902.

[133] R. H. Ritchie. Plasma losses by fast electrons in thin films. *Physical Review*, 106:874–881, 1957.

[134] H. Raether. *Surface Plasmons on Smooth and Rough Surfaces and on Gratings*. Springer, Berlin, 1988.

[135] J. M. Pitarke, V. M. Silkin, E. V. Chulkov, and P. M. Echenique. Theory of surface plasmons and surface-plasmon polaritons. *Reports on Progress in Physics*, 70(1):1–87, 2007.

[136] Y. Xia and N. J. Halas. Shaped-controlled synthesis and surface plasmonic properties of metallic nanostructures. *MRS bulletin*, 30:338–343, 2005.

[137] W. L. Barnes, A. Dereux, and T. W. Ebbesen. Surface plasmon subwavelength optics. *Nature*, 424:824–830, 2003.

[138] Ekmel Ozbay. Plasmonics: Merging photonics and electronics at nanoscale dimensions. *Science*, 311(5758):189–193, 2006.

[139] J. R. Sambles, G. W. Bradbery, and F. Z. Yang. Optical-excitation of surface plasmons: an introduction. *Contemporary Physics*, 32:173–183, 1991.

[140] KOVACS. *Micromachined Transducers Sourcebook*. McGraw-Hill Education, Europe, 2000.

[141] M. J. Madou. *Fundamentals of Microfabrication: The Science of Miniaturization*. CRC Press, 2002.

[142] A. A. Zhukov, A. V. Goncharov, P. A. J. de Groot, P. N. Bartlett, and M. A. Ghanem. Magnetic antidot arrays from self-assembly template methods. *Journal of Applied Physics*, 93(10):7322–7324, 2003.

[143] R. M. Cole, Y. Sugawara, J. J. Baumberg, S. Mahajan, M. Abdelsalam, and P. N. Bartlett. Easily coupled whispering gallery plasmons in dielectric nanospheres embedded in gold films. *Physical Review Letters*, 97(13):137401, 2006.